Modelling of magnetic null points using BOUT++

Brendan William Shanahan

Doctor of Philosophy

University of York

Physics

June 2016

Abstract

One of the major challenges to viable fusion energy is the exhaust of hot plasma, as future magnetic fusion devices will have unacceptably high heat fluxes on the plasma facing components. Recent research into advanced divertor designs and alternative magnetic configurations attempts to alleviate this issue, however the effectiveness of these configurations relies on cross field transport in the poloidal magnetic null region, which is currently poorly understood. Simulations of instabilities and turbulence in X-point configurations are challenging due to the limitations of field-aligned coordinate systems: X-point dynamics are often interpolated based on nearby flux surfaces, which could exclude relevant physics. Here we present the results of turbulence and transport simulations relevant to tokamak X-points in various magnetic geometries using coordinate systems which are not aligned to the magnetic field.

First, we present results as part of a feasibility study of a university-scale linear plasma device capable of producing azimuthal X-points. The turbulent characteristics of this system are explored and measurements using synthetic diagnostics are proposed. These studies are then extended to toroidal geometries by simulating filament propagation in TORPEX poloidal magnetic null point scenarios and comparison to experiment. It is determined that the null region can cause an acceleration of filaments due to increasing connection length, but this acceleration is small relative to other effects, which we quantify. Experimental measurements are reproduced, and the dominant acceleration mechanism is identified as that of a developing dipole in a moving background. Finally, the implementation of the Flux Coordinate Independent method for parallel derivatives into `BOUT++` is investigated by simulating transport and diffusion in nonaxisymmetric geometries. The potential for `BOUT++` to be used as a stellarator turbulence and transport code is also discussed.

Contents

List of Figures

Acknowledgments

I owe the success of this PhD to the phenomenal support structure that I have in my life. Firstly I must extend my sincerest gratitude to my supervisor, Dr. Ben Dudson, for his expertise, patience, and guidance. I would also like to thank the members of the York Plasma Institute, who have made this experience both academically and personally rewarding. Specifically, I'd like to acknowledge Professor Howard Wilson, Professor Bruce Lipschultz, and Professor Kieran Gibson for their valuable advice, and Dr. Jarrod Leddy for his fruitful discussions regarding both physics and more material matters. I must also thank Dr. Nick Walkden, who is somehow still willing to discuss filament physics at any opportunity. Additionally, I am grateful for the help of Dr. Peter Hill, who has led the development of the Flux Coordinate Independent method in `BOUT++`, helping me to achieve my master plan of surreptitiously bringing stellarator physics to the YPI.

I rarely embrace a challenge tentatively, which is the fault of my family. Without their unwavering support and encouragement, I would never have been able to reach my goals. I am very thankful to have loving parents who have always provided for me and given excellent guidance. I must also thank my brother, who has always been the ideal older sibling; always giving the best advice to help me succeed.

Finally, I am eternally grateful to my wife Sophia for her help, patience, and laughter. Many PhD candidates apologize to their spouses for always discussing physics, but I am fortunate enough to have married an incredibly talented physicist. I must therefore thank her for the countless conversations concerning work, and equally for the discussions which have distracted us.

Declaration

I declare that the work presented in this thesis, except where it is otherwise stated, is based on my own research and has not been submitted previously for a degree in this or any other university. Parts of the work presented in this thesis have been published in:

- [1] B W Shanahan and B D Dudson, "X-point modelling in linear geometries using `BOUT++`" *Journal of Physics: Conference Series*, 561(1):012015, 2014.
- [2] B W Shanahan and B D Dudson, "Blob dynamics in TORPEX poloidal magnetic null configurations" *Plasma Physics and Controlled Fusion* **58**(12):125003, 2016.
- [3] B W Shanahan, P Hill, and B D Dudson, "Towards nonaxisymmetry; initial results using the Flux Coordinate Independent method in `BOUT++`" *Accepted to Journal of Physics: Conference Series* 2016.
- [4] J Leddy, B Dudson, M Romanelli, B Shanahan and N R Walkden, "A novel flexible field-aligned coordinate system for tokamak edge plasma simulation" *Accepted to Computational Physics Communications* 2016.
- [5] P Hill, B Shanahan, and B Dudson, "Dirichlet boundary conditions for arbitrary-shaped boundaries in stellarator-like magnetic fields for the Flux-Coordinate Independent method", *Submitted to Computational Physics Communications* 2016.

Chapter 1

Introduction

1.1 Global Energy Picture

It is becoming increasingly apparent that that the global energy production and consumption is not sustainable[6, 7, 8]. Two main factors which should drive humanity's migration toward cleaner, renewable energy are the imminent climate change due to atmospheric greenhouse gas emissions and the reduction of fossil fuel supplies.

1.1.1 Carbon emissions and peak oil

The ongoing climate change due to emission of greenhouse gasses is one of the most pressing issues facing humanity; it is now clear that the carbon emissions due to human civilization [9, 10] has already begun affecting living systems [11]. Greenhouse gas emissions must be reduced in order to avoid global temperature increases which will lead to rising sea levels, severe droughts and other catastrophic events [12, 13].

As of 2013, 79% of global energy consumption relies on fossil fuel energy sources [14]. This over-reliance on fossil fuels is concerning as these resources are finite. M. King Hubbert originally postulated the idea of peak oil, where the global supply of oil will one day peak, leading to rapid decline in availability [15]. Many of the subsequent studies have proposed that we have already passed the

time for peak oil supply, as shown for example in Figure 1.1 [16].

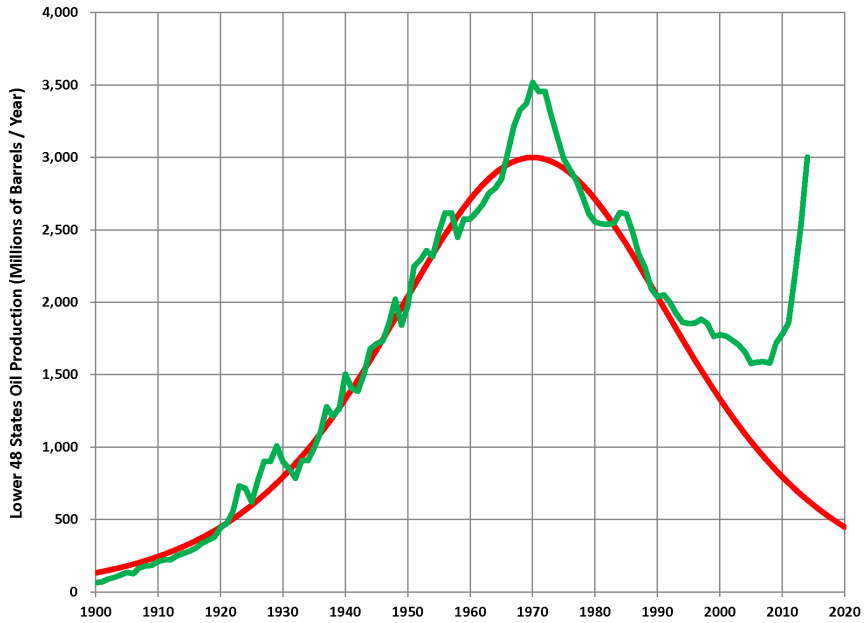

Figure 1.1: Comparison of Hubbert's upper bound peak oil model for the contiguous United States and the corresponding actual oil production, taken from [16].

Prior to the mid 2000s, it appeared that global oil production had peaked. As seen in Figure 1.1, however, oil production in the United States (and numerous other areas) has recently seen a large increase due to the realization of methods allowing for extraction of oil in areas which was previously thought impossible. The most common method for this is called "hydraulic fracturing" or "fracking" of shale oil which was originally patented in the 1960s [17]. The major disadvantage of this method of oil extraction is its environmental impact on ground- and surface water [18]. Nevertheless, the increase in oil production from hydraulic fracturing has sparked several counterarguments to peak oil that suggest global energy production from fossil fuels is far from peaking, but that there is enough world reserves for the next century. Nevertheless, a viable alternative should be found within that (relatively short) century.

There are several candidates for clean, renewable energy sources – solar, wind, geothermal, etc. In reality, many renewable energy sources should be used together, as each has its own advantages and disadvantages. Nuclear fission will

probably provide the majority of the "clean" energy for the near future. However, nuclear nonproliferation limits the research of fission, and the safe and responsible storage of long-lived radioactive waste is a still major challenge. Other means of energy production have limited availability due to their dependence on factors such as the cost, large land areas required, and the dependence on local weather.

An ideal energy source would have a very large natural fuel supply, emit no greenhouse gasses, and have no long lived radioactive waste. Additionally, the energy should come from a consistently available, compact and safe system free from risks of large scale catastrophe. Fusion power has the potential to fulfil these criteria, but there are a number of challenges which have yet to be overcome.

1.2 Fusion as an energy source

Fusion energy is beginning to establish itself as a viable alternative to conventional energy sources[19, 20]. Fusion is the principle by which the Sun produces energy. By forcing light nuclei together it is possible to overcome the Coulomb repulsion and allow the strong force to combine the nuclei into one heavier nucleus. The resulting nucleus is lighter than the combined constituent nuclei, and the "missing" mass is converted to energy via the now-famous relation $E = mc^2$ [21].

The most promising reaction for commercial fusion prospects is thought to be the fusion of Deuterium and Tritium:

$$ {}^{2}_{1}\mathrm{D} + {}^{3}_{1}\mathrm{T} \rightarrow {}^{4}_{2}\mathrm{He} + \mathrm{n} + 17.6\mathrm{MeV} \tag{1.1} $$

While there are other approaches being investigated, the D-T reaction is generally favored as it has a relatively high cross section at temperatures achievable in laboratory plasmas (around 10keV), as shown in Figure 1.2 [22].

If there are enough nuclei fusing and producing this energy, the reaction can be self sustaining. The parameters necessary for this to occur were first calculated by J D Lawson [23]. This calculation provides a minimum threshold which is necessary for ignition, or the self sustaining fusion reaction, and is often

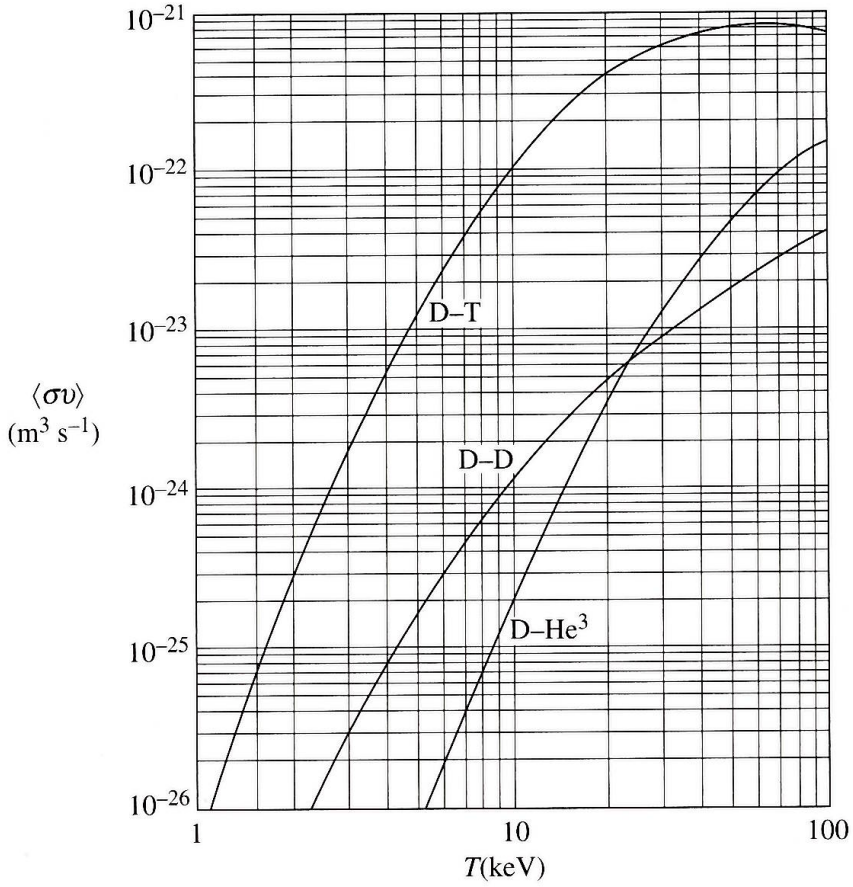

Figure 1.2: Average cross section times reactant velocity ($\langle\sigma\nu\rangle$) for the three most common fusion reactions as a function of temperature [22].

expressed as a triple product:

$$nT\tau_E \geq \frac{12}{E_{fusion}} \frac{T^2}{\langle\sigma\nu\rangle} \tag{1.2}$$

where n is the density, T is temperature, and τ_E is the energy confinement time. To determine these values, one must know the reaction cross section σ, the speed of a reactant nucleus ν, and the energy from the fusion reactions E_{fusion}. For the D-T reaction, this triple product must be greater than 10^{21}keV s/m^3 for temperatures relevant for laboratory fusion (10-20keV). It should be noted here that temperatures in plasma physics are often referred to in units of electron volts (eV). For reference, a plasma with a temperature of 1keV is over 11 million degrees

Celsius. This is where the challenges to fusion begin; how to create sufficient densities and temperatures while maintaining good enough confinement. There are several routes to fusion, all of which focus on creating a plasma where the parameters fulfil this Lawson criterion, Equation 1.2.

1.2.1 Plasma

Plasma is the fourth and most common state of matter in the universe. A plasma is formed when the electrons are stripped from atoms, allowing the nuclei (ions) and electrons to move individually. This dissociation of electrons can be accomplished either by increasing the temperature or subjecting matter to very strong electromagnetic fields. Plasmas may seem unfamiliar but are apparent in everyday life. Lightning, flames, and fluorescent light bulbs are all examples of plasma – although these plasmas vary greatly from those used in fusion applications. Plasmas differ to the descriptions of gasses in that they can be described by their collective behavior.

The physics of plasma is fundamental to the study of nuclear fusion. As stated in the previous section, fusion plasmas must have a high triple product – the combination of density, temperature, and confinement time. The two principle routes to fusion, inertial confinement fusion (ICF) and magnetic confinement fusion (MCF) attempt to achieve this by maximizing different factors.

1.2.2 Common routes to fusion

The fundamental challenge of fusion – to confine a dense, hot plasma for long enough to produce fusion reactions – is apparent when considering the scale of the parameters involved. Typical fusion reactions are most convenient at 10keV (which corresponds to over 100 million degrees Celsius). It is clear that one must be clever in confining something with these temperatures, as most materials cannot withstand such heat. There are two main routes which have had early success in containing these reactions. The first of which is inertial confinement fusion which attempts to produce fusion reactions in plasmas at high densities for

short confinement times, and localize these reactions far away from any confining material walls.

1.2.3 Inertial confinement fusion

Inertial confinement fusion typically uses lasers to either directly or indirectly heat a spherical capsule of DT fuel, and cause it to implode. The ablation of the outer surface causes an inward compression of the capsule, allowing for a hot, dense sphere to fuse nuclei [24, 25]. This process is shown in Figure 1.3.

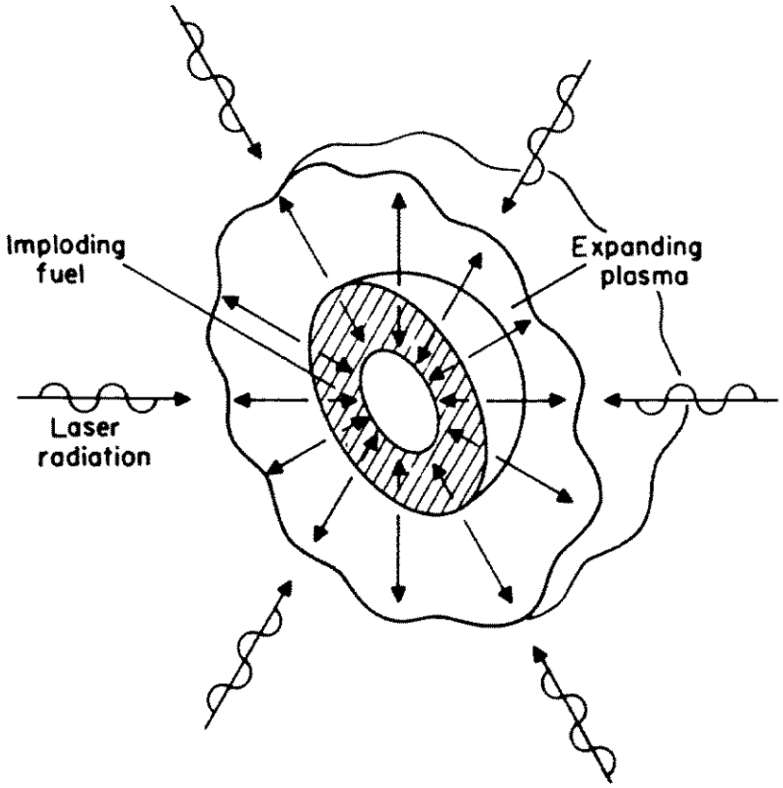

Figure 1.3: The fundamental physics behind direct-drive inertial confinement fusion [25].

Inertial confinement fusion relies on the idea of having very high densities (around $10^{29} \rightarrow 10^{30}\text{m}^{-3}$), with a relatively low confinement time (order 1ns), as the plasma is only confined by its inertia inwards. The challenges of inertial confinement fusion are apparent when examining these scales, but there have been recent advancements at the National Ignition Facility (NIF) which is

located at Lawrence Livermore National Laboratory. Recent experiments have achieved about 40% of the expected Lawson criterion fusion yield [26]. It should be noted however, that early design of NIF and simulations of capsule implosions predicted higher performance [27]. Turbulent mixing of hot and cold fuel as well as nonuniform implosion are challenges which have yet to be overcome [28].

1.3 Magnetic confinement fusion

The other primary route to fusion utilizes a lower density plasma ($10^{20}\mathrm{m}^{-3}$) which is confined for longer times (order 1 second) and relies on the physics of charged particle motion in magnetic fields.

1.3.1 Fundamentals of magnetically confined fusion

To understand the motivation behind using magnetic fields to confine plasmas for fusion applications, it is useful to consider single particle classical motion. Charged particles are free to move along magnetic field lines but are subject to the Lorentz force:

$$\mathbf{F} = Ze\left(\mathbf{E} + \mathbf{v} \times \mathbf{B}\right) \tag{1.3}$$

This constraint means that particles follow helical paths along field lines in the absence of electric fields as shown in Figure 1.4, where the radius of their orbit is described as the Larmor radius:

$$r_L = \frac{mv_\perp}{qB} \tag{1.4}$$

In strong magnetic fields, the particle experiences a relatively constant field, and therefore it's angle relative to the field line does not matter. Therefore, the particle will feel the same torque from the magnetic field. This torque on a particle

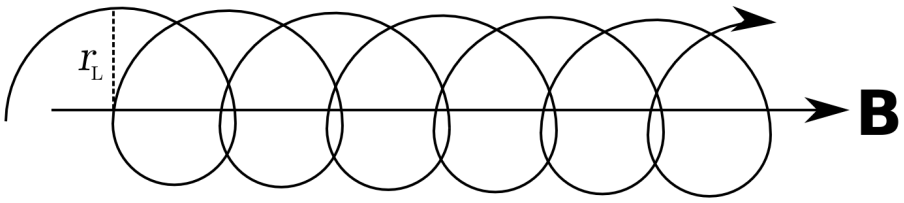

Figure 1.4: A single particle travelling helically along a field line when there is no electric field present.

by a magnetic field is called the magnetic moment, and is given by Equation 1.5:

$$\mu = \frac{mv_\perp^2}{2B} \tag{1.5}$$

In the absence of an electric field, the charged particle can do no work. Therefore the energy (and magnetic moment) are invariant. By splitting the velocity of a particle into its parallel and perpendicular components one can write:

$$v_\parallel^2 = v^2 - v_\perp^2 = v^2 - \frac{2\mu B}{m} \tag{1.6}$$

where we have used the expression for magnetic moment (1.5) to replace $v_\perp$. When $v_\parallel = 0$, the particle is purely gyrating around the field line, and not moving parallel to the magnetic field. At the limit of the very large magnetic field, Equation 1.6 is negative. As speeds are not imaginary, this means that the particle reflects and returns to the area of weaker magnetic field. This is the basis for a magnetic mirror [29], a schematic of which is shown in Figure 1.5.

In these magnetic mirrors, particles would be reflected back from the regions of high magnetic field strength. From the conservation of magnetic moment, it

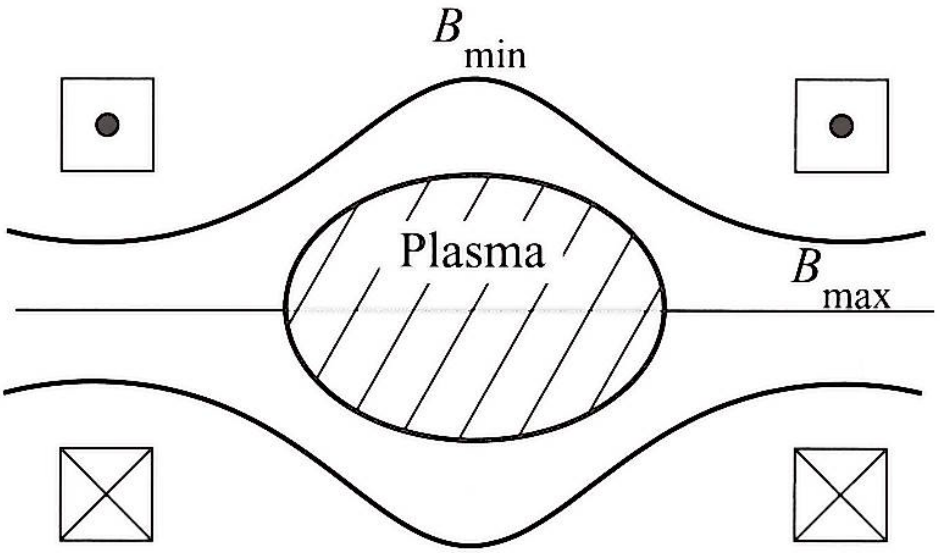

Figure 1.5: The magnetic mirror concept for confining a fusion plasma [30]

can be shown that particles will only be lost if the following relation is fulfilled:

$$\frac{v_{\perp \min}^2}{v^2} < \frac{B_{\min}}{B_{\max}} \tag{1.7}$$

Where $v_{\perp \min}$ is the perpendicular velocity in the region of the minimum magnetic field strength, $B_{\min}$, and $B_{\max}$ is the maximum magnetic field strength. Unfortunately, plasmas are composed of many ions, and collisions between particles ensure that a large fraction of particles will eventually enter the "loss cone" of Equation 1.7. These end losses made it difficult to obtain fusion-relevant conditions in these mirror devices. The natural way to prevent end losses is to remove the ends of your device by wrapping it into a torus. This is the basis for toroidal confinement devices.

1.3.2 Toroidal confinement

By creating a toroidal magnetic field to overcome end losses, the magnetic field can no longer be considered uniform across a poloidal cross section. The magnetic field is now higher on the inside of the torus than it is on the outside. This

gradient in the magnetic field creates particle drifts – as a particle is orbiting around the magnetic field line, it feels different strengths of the magnetic field. Therefore, when referring to Equation 1.4, one can see that the radius of the charged particle orbit will be smaller in the high field side, and larger in the region of weaker magnetic field. This leads to a net drift (which will be discussed more in Section 2.2.1), which degrades confinement.

To overcome this, the field lines in toroidal configurations must not be strictly toroidal. Consider an ion which drifts upward when on the top of the torus. If the field line wraps around the torus helically, the ion will be able to also drift upwards when it is at the bottom of the torus – thereby negating any previous drift outward. By introducing an additional (poloidal) magnetic field, the confinement of particles is recovered. The degree by which a field wraps helically around a torus is called the *rotational transform*. It is the manner by which this rotational transform is implemented which distinguishes various toroidal confinement devices.

1.3.3 Tokamaks

In the 1950s, physicists Igor Yevgenyevich Tamm and Andrei Sakharov suggested that the rotational transform could be generated by a toroidal current within the plasma, which would create a poloidal magnetic field [31]. This was termed the TOroidal'naya KAmera v MAgnitnyuk Katushkakh, or the tokamak. An illustration of a simple tokamak is given in Figure 1.6.

In a tokamak, magnetic field coils create a toroidal field, and a central transformer coil is supplied with a time-varying current, which creates a varying magnetic flux and induces a toroidal current. This toroidal current creates a poloidal magnetic field, which creates the rotational transform necessary for confinement [22]. By the late 1960s, tokamaks began to outperform other contemporary configurations, and the tokamak configuration has since continually set the benchmark for fusion performance. The Joint European Torus (JET), located in Culham, England currently holds the record for the highest fusion gain, when it produced 16.1MW of fusion power in the late 1990s [33, 34].

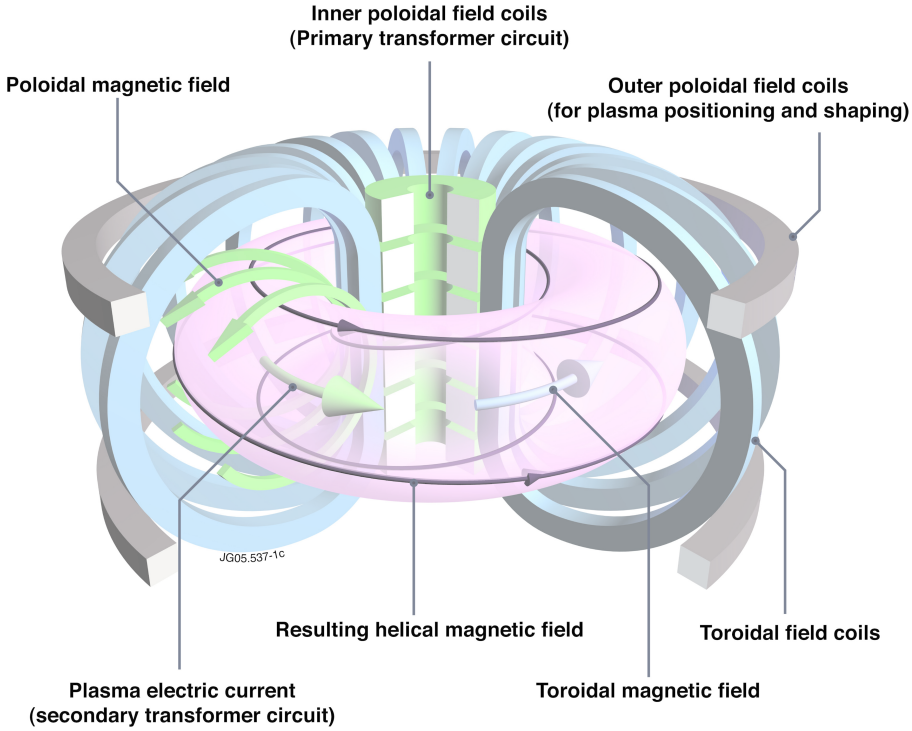

Figure 1.6: A schematic of a simple tokamak [32]

The performance of the tokamak configuration has led to the construction of the ITER device [35] in Cadarache, France, which will become operational in the late 2020s. This experiment is designed to have an energy gain of 10, such that the fusion power produced is 10 times higher than the power used to heat and contain the plasma. The ITER project is an international collaboration and marks an important era in fusion research.

There are, of course, disadvantages to tokamaks. Some of the more relevant challenges will be discussed in Section 2.1. However, additional challenges are manifested in the form of current-driven instabilities and disruptions – where the plasma violently extinguishes. These instabilities can be mitigated by creating a rotational transform without inducing a plasma current.

1.3.4 Stellarators

Also in the late 1950s, Lyman Spitzer began to study the three dimensional confinement of particles and suggested that external magnetic coils could produce a rotational transform. This can be done by either rotating the poloidal cross

section of the plasma or with a torsion of the magnetic axis. The advantage of this configuration is that there are very small plasma currents, limiting the effect of current-driven instabilities and disruptions. He termed this concept the stellarator, and the first designs were in the form of a figure-eight [36]. Unfortunately these early devices had very poor confinement, especially in comparison to the tokamak.

Despite their early struggles, the stellarator concept of producing a rotational transform with external coils persisted. By the late 1980s, stellarator research on what are now considered 'classical stellarators' culminated in the Wendelstein 7-AS device, which is shown in Figure 1.7 [37].

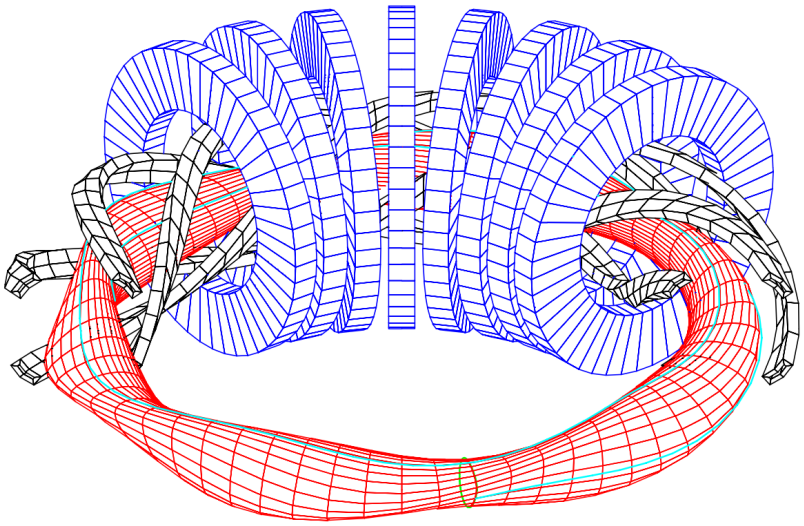

Figure 1.7: A schematic of the Wendelstein 7-AS stellarator, which is known as a "classical stellarator" due to the in-vessel helical coils. Image from [37].

The blue, toroidal field coils in Figure 1.7 produce a toroidal field. The black, helically winding coils produce the rotational transform and poloidal flux surfaces, since the current direction alternates between coils. These helical coils posed a major challenge in classical stellarator construction. However, the relatively recent advent of modular coils allows for easier construction and better diagnostic access [38].

Stellarator design is challenging due to their inherently three dimensional nature. While tokamaks were considered axisymmetric since the poloidal cross

section does not change toroidally, modern stellarators exploit other symmetries, such as helical symmetry. As such, there are many more degrees of freedom when designing a stellarator [39, 40]. For many years, this was a disadvantage as theoretical and computational tools for stellarator optimization were not available until the late 1990s [30]. Recently, however, developments in the stellarator concept has led to in the construction of the Wendelstein 7-X experiment in Greifswald, Germany [41].

The inherent nonaxisymmetry of stellarators causes difficulty in designing, constructing, and analyzing stellarators. The final research chapter of this thesis discusses the challenges of simulating nonaxisymmetric configurations, and reports the recent progress towards stellarator edge turbulence modelling in `BOUT++`.

1.4 Outline

The research presented within this thesis focuses on simulating edge transport and turbulence in various magnetic geometries relevant to fusion. Transport at the edge of magnetic fusion devices dominates the performance of fusion plasmas. It is therefore necessary to determine the nature of this transport, and be able to simulate it effectively.

This thesis is arranged as follows. Chapter 2 provides a brief review of the fundamental physics of transport in magnetically confined plasmas, and highlights the methods used in describing tokamak plasmas. The simulation of plasma turbulence in toroidal geometries will also be discussed. The chapter also introduces `BOUT++`, a plasma turbulence framework used here to simulate turbulence in three different geometries, before concluding by introducing numerical methods and deriving an isothermal plasma turbulence model which has been implemented in `BOUT++`.

Chapter 3 discusses simulations of turbulence in linear geometries where an azimuthal magnetic null point is present. This work serves as a feasibility study for a university-scale linear plasma device to study plasma scenarios relevant to tokamak heat and particle exhaust.

Chapter 4 reports results in simulating plasma filaments in poloidal magnetic null point scenarios in the TORPEX device. Filaments (or blobs) are coherent structures which transport heat and particles in magnetically confined plasmas. Understanding their behavior in scenarios applicable to a tokamak scrape off layer is important in minimizing turbulent losses.

Chapter 5 reports the progress in modelling nonaxisymmetric configurations in `BOUT++`. At the moment, there is no code capable of simulating plasma fluid turbulence in the entire edge of nonaxisymmetric devices. Recent numerical implementations into `BOUT++` have allowed for nonaxisymmetric geometries. Here a proof of principle is provided indicating the ability of `BOUT++` to perform global edge fluid transport and turbulence simulations in nonaxisymmetric geometries, which will, among other things, allow for analysis of divertor interactions in stellarators.

Finally, Chapter 6 will provide conclusions and prospective future work based on the research presented herein.

Chapter 2

Background

Before discussing the research presented within this thesis, it is important to understand the motivation behind the work. This chapter attempts to provide a context for this research, while introducing concepts which will be important in understanding the following chapters. Section 2.1 discusses the general tokamak configuration which is used in modern experiments, and why this configuration has been chosen. The following section, Section 2.2 provides a brief introduction to the transport mechanisms inherent to the tokamak configuration, and how these effects limit the confinement. The most dominant transport phenomenon, turbulence, is introduced in Section 2.3, which also includes a review of the physics of a turbulent mechanism which is extensively studied in Chapter 4. The simulation framework `BOUT++` is introduced in Section 2.4 before concluding with a derivation of the plasma fluid model (Section 2.5.1) and numerical methods essential to the research presented within this thesis.

2.1 The modern tokamak

Early tokamaks were very similar to that described in Section 1.3.3; toroidal magnetic configurations with poloidal magnetic field manifested by a toroidal current within the plasma. By considering only the classical transport as described in Section 1.3.2, early estimates predicted fusion could be accomplished in a machine on the order of centimeters [42]. However, there are other transport mechanisms

(such as turbulence which will be discussed in Section 2.3) which have dictated that machines must be much larger than originally thought. With the increase in machine size comes an increase in performance; some of the most important challenges in fusion are associated with the control of heat and particle flux onto plasma facing components.

2.1.1 The diverted tokamak

The original interface between tokamak plasmas and the wall of the device was a segment of metal onto which particles and heat were deposited at the outer edge of the plasma. This device was called a limiter, and effectively isolated the rest of the wall of the device from the hot plasma. The part of the plasma which interacted with the limiter was called the scrape off layer (SOL), as it was the final layer of plasma which was "scraped off". The main disadvantage of the limiter, however, was that this method introduced a large amount of impurities into the plasma[30]. High-Z impurities from the wall material are problematic in tokamak plasmas as they tend to radiate energy and cool the hot, dense, core region[43]. In order to mitigate the amount of impurities entering the plasma from surface interactions, the divertor concept was implemented. A divertor configuration uses an extra set of magnetic coils to create a poloidal magnetic null point at the edge of the confined plasma. The plasma diffuses across this area and deposits particles and energy along field lines onto target plates. As these target plates are farther separated from the core plasma, there is less contamination from impurities[30, 44]. Figure 2.1 illustrates the difference between plasma cross sections in the Joint European Torus (JET) in both limiter and divertor configurations [45].

The implementation of the divertor concept brought a drastic improvement in the performance of tokamaks. Most notably, diverted tokamaks began to be able to access operating regimes of improved confinement. This high confinement mode or "H-mode" was first discovered on the ASDEX machine in Garching, Germany [46]. While the mechanism is still a subject of research nearly 35 years later, H-mode exhibits increased flows at the plasma edge, which lead to the suppression of turbulence [47, 48].

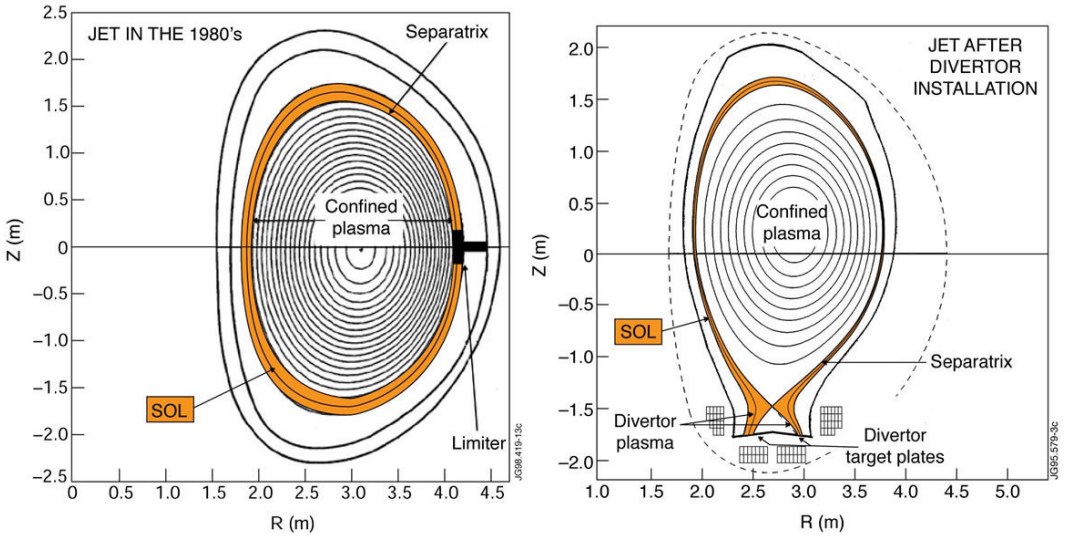

Figure 2.1: Plasma cross sections in JET in both limiter and divertor configurations [45]

While the divertor concept increased the performance of tokamaks, it also increased the heat and particle flux density onto plasma facing components. There is growing concern that traditional divertor configurations in future devices could still have unacceptably high heat fluxes, especially during transient events [49, 50]. As a result, there have been increasing studies into alternative concepts which could lessen the stress on divertor targets [51, 52]. At the moment, the proposed operating scenario for ITER is one with partial divertor detachment [53], where a gas is injected into the divertor area which allows for cooling of the plasma via collisions and radiation prior to striking the divertor targets. This scenario could be insufficient for future tokamak reactors, however, as the heat fluxes will be much higher and access to detached scenarios will be limited [54]. Alternatively, there have been studies to alter the magnetic configuration such that the heat load on the divertor targets is minimized. One particular design to be studied is the snowflake divertor [55]. This design utilizes an additional set of coils to create extra branches to dissipate plasma flows toward target plates, thereby reducing heat flux. An illustration of this configuration is shown in Figure 2.2.

The effectiveness of the snowflake divertor relies on cross field transport in the poloidal magnetic null region. However, transport in this area is poorly

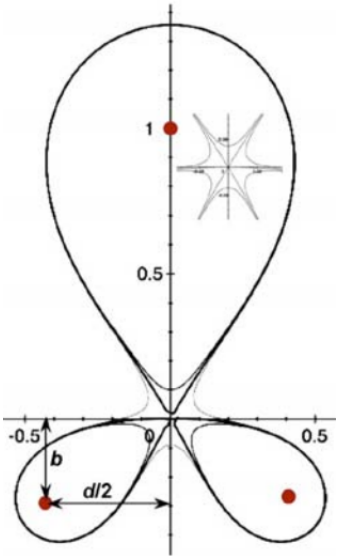

Figure 2.2: A schematic of a perfect snowflake divertor[56]

understood, as the majority of plasma turbulence simulations do not directly model X-points, since they usually employ a field-aligned coordinate system. The X-point is where flux surfaces cross, and in a tokamak this region has effectively no poloidal magnetic field component. For reasons which will be discussed later, X-points create numerical instability in plasma turbulence simulations and are therefore difficult to model efficiently. The most common method currently is to interpolate parameters from either side of the X-point region. This system, however, could potentially exclude important physics associated with this region. As a region of complicated plasma dynamics which can greatly affect the edge and SOL flows, the X-point region is an area that merits direct modelling, and this is a major aim of this research.

2.2 Transport in tokamaks

If the plasma physics associated with toroidal confinement were as simple as described in Section 1.3.2, it would be possible to have a tokamak producing a net energy gain via fusion reactions in a relatively small room. Unfortunately, the analysis presented previously neglected important transport mechanisms which are inherent in toroidal magnetic confinement: *drifts* and *turbulent* transport.

2.2.1 Plasma Drifts

A toroidal magnetic configuration destroys the magnetic field uniformity of linear configurations. Any lack of uniformity will lead to either parallel acceleration (partially discussed in Section 1.3.1), or a drift of particles perpendicular to the magnetic field, which will be briefly discussed here.

Drifts of particles can be broadly characterized by the general drift mechanism:

- A partial expansion/contraction of the Larmor orbit, causing a nonuniform Larmor radius as a particle completes an orbit: $\mathbf{E} \times \mathbf{B}$, $\nabla \mathbf{B}$, and curvature drifts
- A shift of the Larmor orbit: the polarization drift
- Fluid flows due to Larmor motion: the diamagnetic drift

Referring to the Lorentz force (Equation 1.3), we can see that the perpendicular motion of a charged particle can be influenced by either the electric field or the magnetic field. Let us first consider the effect of an electric field perpendicular to the magnetic field, which is shown in Figure 2.3 [30].

A charged particle is always accelerated either parallel or anti-parallel to the electric field, depending on the sign of the charge. Referring to situation (a) in Figure 2.3, we see that at point 1 of a particle's orbit, it is travelling parallel to the electric field. This causes an acceleration such that at point 2, the particle has a higher perpendicular speed, $v_\perp$, before it is decelerated at point 3 such that it has a low perpendicular speed at point 4. By referring to Equation 1.4, we see that this creates a larger Larmor radius at the top of the orbit, and a smaller orbit at the bottom. This causes a net drift outwards, which is referred to as the $\mathbf{E} \times \mathbf{B}$ drift as it is caused by an electric field which is perpendicular to the magnetic field. The radial drift velocity v_E caused by this effect is described as in Equation 2.1

$$v_E = \frac{\mathbf{E} \times \mathbf{B}}{B^2} \tag{2.1}$$

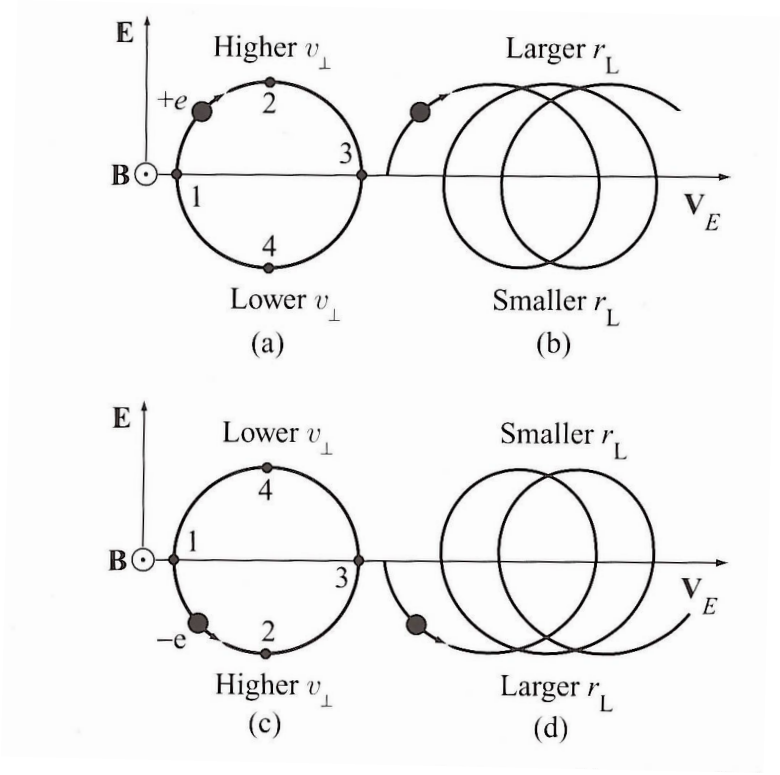

Figure 2.3: An illustration of the $\mathbf{E} \times \mathbf{B}$ drift [30]

This effect – that a perpendicular (specifically, vertical) electric field causes a radial advection – is an important mechanism in filament dynamics, which will be discussed in greater detail in Section 2.3.1. Understanding the consequences of this effect will help to understand confinement degradation in tokamaks and other magnetic confinement devices.

Another mechanism for particle drifts is a variation in the magnetic field. It has already been discussed how a parallel variation in the magnetic field strength can lead to trapped particles in magnetic mirrors. A radial nonuniformity can also lead to a particle drift, as described in Figure 2.4.

When referring again to the expression for a particle's Larmor radius, Equation 1.4 it is apparent that in areas of higher magnetic field, the particle will have a smaller Larmor radius. This in turn means that the variation in the magnetic field strength causes a nonuniform orbit, leading to a drift (which is shown here to be vertical). Unlike the $\mathbf{E} \times \mathbf{B}$ drift, the ∇B drift causes the electrons and positively charged ions to drift in opposite directions. The ∇B drift can be described

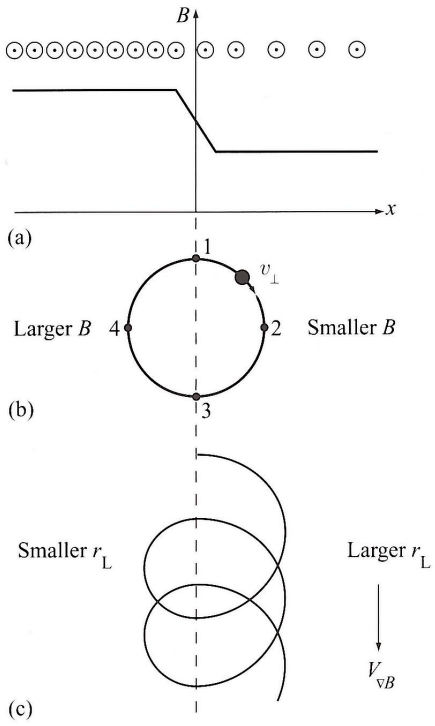

Figure 2.4: An illustration of the ∇B drift [30]

in a similar form to the $\mathbf{E} \times \mathbf{B}$ drift:

$$v_{\nabla B} = \frac{v_\perp^2}{2\Omega_c} \frac{\mathbf{B} \times \nabla \mathbf{B}}{B^2} \tag{2.2}$$

where $\Omega_c = \frac{e_s B}{m_s}$ is the Larmor, cyclotron, or gyro-frequency – or the frequency with which a particle orbits a field line – where e_s and m_s are the charge and mass of the species, respectively. It should be noted here that the gyrofrequency carries the sign of the charge, which indicates the direction of oscillation around the field line. From Equation 2.2, we see that a radial gradient in the toroidal magnetic field strength causes a vertical drift.

The final drift which is caused by the modification of the Larmor radius across a gyro-orbit is the curvature drift. As a particle is traversing along a curved field line, it will experience a centripetal force. At the top of the gyro-orbit (for instance) this force accelerates the particle, causing a larger Larmor radius, and decelerates the particle at the bottom of the orbit. This, like the ∇B

drift, causes a vertical net drift, given by:

$$v_{curv} = \frac{v_{\parallel}^2}{\Omega_c} \frac{\mathbf{R_c} \times \mathbf{B}}{R_c^2 B} \tag{2.3}$$

where $\mathbf{R}_c = R_c\mathbf{r}$ is the radius of curvature. Similar to the ∇B drift, the curvature drift causes electrons and ions to be shifted in opposite directions. In a fluid model like that which will be described in Section 2.5.1, the curvature and ∇B drifts are combined since the parallel and perpendicular velocities are not evolved separately.

These three drifts have been derived considering time-independent electromagnetic fields. However, when a time-varying electromagnetic field is imposed, further drifts can arise. Let us first consider a time-varying radial electric field. If a particle initially at rest in a homogeneous magnetic field suddenly experiences a radial electric field $\mathbf{E}$, it will be accelerated radially – for ions, in the direction of the electric field. Once it is in motion, it experiences the effects of the magnetic field, and begins to gyrate in a Larmor orbit. Once the electric field is no longer applied, the particle no longer experiences a radial force, and is left to gyrate. Now, however, it's guiding center has been shifted radially. This is described as the polarization drift, and is described by:

$$v_{pol} = \frac{1}{\Omega_c B} \frac{d\mathbf{E}}{dt} \tag{2.4}$$

As this drift relies on a time varying electric field, it can only be present for a finite amount of time. Therefore this drift can be relatively small, but the current associated with this drift is an important mechanism in plasma dynamics, as will be discussed in Chapter 4.

It should be noted that the drifts described by Equations 2.2, 2.3, and 2.4 are all dependent on the mass of the species. For this reason, the drifts will be smaller for electrons than for ions, as $m_e/m_i \ll 1$. Furthermore, the discussion here is meant solely to be illustrative, since currents derived from considerations

of single particle orbits can be misleading, as a full currents should be averaged over entire distributions of particles – currents will most likely not be completely uniform.

The final drift which will be discussed is the diamagnetic drift which is caused by a gradient in pressure. One of the most distinguishing features of the diamagnetic drift is that the individual gyro-orbits do not drift; rather, there is a net fluid motion of particles which can be described as a drift. Consider a situation with a pressure gradient perpendicular to the magnetic field, as shown in Figure 2.5.

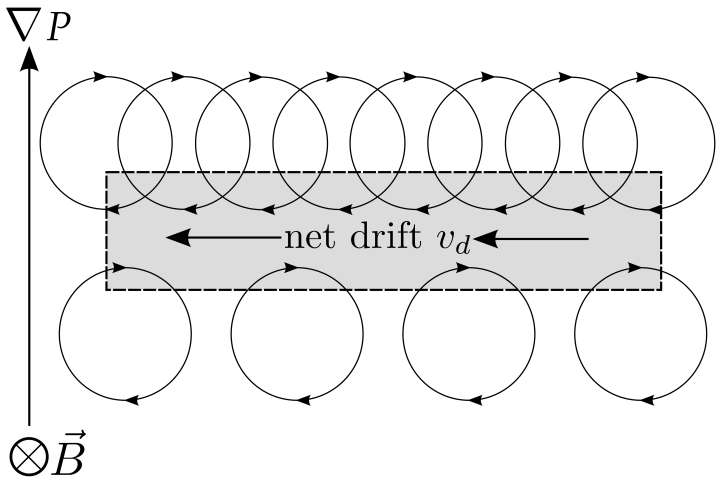

Figure 2.5: A description of the diamagnetic drift.

Consider the shaded region in Figure 2.5. Due to the pressure gradient ∇P, there are more particles at the top of the diagram than at the bottom. Therefore, in this shaded region, there are more particles appearing to move to the left than those to the right. This creates a net drift motion of a fluid, and is called the diamagnetic drift. An expression for the fluid velocity of the diamagnetic drift is shown as Equation 2.5.

$$v_d = \frac{1}{Zen}\frac{\mathbf{B}\times\nabla P}{B^2} \tag{2.5}$$

Again, this drift is dependent on the charge of the particle, and is in opposite

directions for electrons and ions. This drift is important in filament dynamics, which will be discussed in Section 2.3.1, as it can lead to currents within the filaments and ultimately a charge separation. In a constant magnetic field, the MHD equilibrium force balance equation ($\mathbf{J} \times \mathbf{B} = \nabla P$) dictates that the there must be a uniform pressure. Therefore this current arises to maintain equilibrium and cancel the opposing field. However, no isolated finite pressure plasma can develop a self-confining magnetic field to satisfy a force-balance equilibrium [57]. Furthermore, a density gradient in a finite plasma will cause drift waves, which flow perpendicular to the magnetic field at the diamagnetic drift velocity [22]. To illustrate how the diamagnetic current arises, consider a Gaussian perturbation in density in the plane perpendicular to the magnetic field, Figure 2.6.

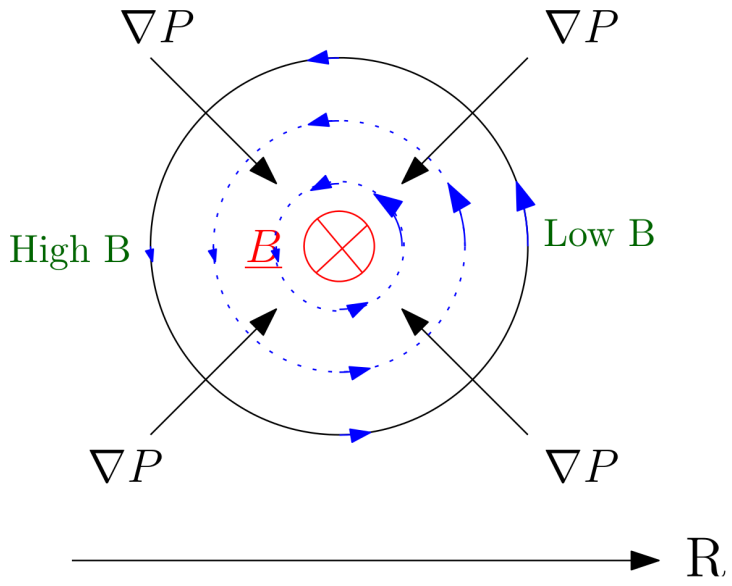

Figure 2.6: An illustration of the diamagnetic current. Pressure gradients create a flow perpendicular to both **B** and ∇P (counterclockwise here). However, since the magnetic field is not constant, the effect is stronger in areas of weaker magnetic field, and therefore causes a net vertical drift. Diagram courtesy of Ben Dudson

Consider particles on particular flux surfaces (labelled in blue in Figure 2.6). While the diamagnetic drift doesn't lead to a direct shift of individual particles, there is a net fluid drift counter clockwise. However, since there is a gradient in magnetic field, the drift is stronger (referring to Equation 2.5) for those particles in the region of weaker magnetic field. This results in a net current which can be

described by the following relation:

$$J_{dia} = \frac{\mathbf{B} \times \nabla P}{B^2} \tag{2.6}$$

This current is fundamental to the physics of blob propagation, which will be discussed in Section 2.3.1. Note that the divergence of this current has the same net effect as the divergence of the ∇B and curvature drift currents. This is best noticed by expanding the MHD equilibrium force balance equation ($\nabla P = \mathbf{J} \times \mathbf{B}$), and noting $\nabla \times \mathbf{B} = \mathbf{J}$, providing a curvature term and a pressure gradient driven term.

We have been able to describe the main drifts in tokamaks. While these effects do limit the performance of tokamaks, there is an additional transport phenomenon which further degrades the confinement. The following section discusses turbulence and its effect on the confinement of plasma in magnetic configurations.

2.3 Turbulence

Tokamaks were originally predicted to provide a net energy output from a relatively small device. Unfortunately these predictions failed to consider the effects of plasma turbulence. Turbulence is a ubiquitous phenomenon in all fluids; it is apparent when milk is poured into tea, and in the evolution of galactic clouds. The varied forms of turbulence have prevented a unified theory to describe it. It is not a new phenomenon either – Leonardo Da Vinci sought to understand the nature of turbulence, as is evident in his drawings dated 1510, shown as Figure 2.7 [58].

Turbulence, perhaps due to its ubiquitous (and equally varied) nature, has been defined in many different ways. Let us choose a definition similar to that of Tsytovich [59], which describes turbulence as nonlinear dynamical behavior with:

- (apparent) randomness and irreversibility. Turbulence is deterministic and dependent on initial conditions.

Figure 2.7: Drawings from Leonardo Da Vinci describing the turbulent motion of fluids, indicating a cascade of eddies at various scales.

- the excitation of fluctuations across a range of scales.
- exchanges of energy between fluctuations excited over this range of scales.

This definition of turbulence is broad, but thereby encapsulates almost all aspects of the various forms of turbulence. In studying turbulence, we select properties to be studied. The typical properties of turbulence which are analyzed are (not limited to):

- Correlations: how closely two quantities are related
- Correlation lifetimes: the amount of time it takes for the relation between quantities to be lost. The random nature of turbulence gives correlations a finite lifetime.
- Spectral energy transfer: the transfer of energy between scales. This is apparent in Figure 2.7, where Da Vinci has drawn water whirls in many different sizes, having been created by a large perturbation – the flow from the top right. This phenomenon is often described in cascades of turbulent eddies.
- Invariance, symmetry, and symmetry breaking: homogeneous, unbounded turbulence has an apparent symmetry in the cascade through scales and the

excited modes. By imposing boundaries (i.e. in a tokamak), the symmetry is broken.

- Transport or movement: the spatial transport of quantities via turbulence is a fundamental obstacle in plasma physics

It is now understood that turbulent transport is the dominant radial diffusive process in tokamak devices [60, 61], and therefore limits performance and determines machine size. Furthermore, turbulence in fusion plasmas can affect the heat and particle flux onto plasma facing components. While turbulence has been studied extensively for centuries, a complete unified description remains a mystery.

Fortunately, there have been significant advances in understanding plasma turbulence in recent years [62]. By modelling plasma turbulence in tokamaks, one can ascertain the performance of certain configurations. For instance, the fluid turbulence simulations presented within this thesis allow for direct experimental comparison to present devices. By benchmarking simulations against experiments, it is possible to apply the same numerical methods to future devices and predict their behavior. Additionally, it is possible to surmise configurations which limit turbulent transport and therefore increase performance.

2.3.1 Filament Physics

Part of the research presented in this thesis, specifically Chapter 4, explores the behavior of filaments (or blobs) in a complicated magnetic geometry including a poloidal magnetic null region. Filaments are typically field aligned plasma structures found in the edge and scrape off layer (SOL) of tokamaks, and are a form of turbulent transport. There is a good review of filament physics found in [63], and this section will serve only as a brief overview.

D'Ippolito *et al.* [63] define blobs as:

- A monopole density distribution with a peak value much higher than the surrounding RMS fluctuations of the background plasma (typically ≥ 2 times)

- Having an alignment to the magnetic field such that variation along the field line is weaker than in the transverse direction
- Exhibiting a dominantly dipole potential in the perpendicular plane which causes a strong component of $E \times B$ motion radially.

There are many different names for plasma filaments [64]. For the sake of simplicity, the terms 'filament' and 'blob' will be used interchangeably when referring to this phenomenon throughout this thesis.

There has been substantial research into the physics of blobs, as they are considered to be an important mechanism for heat and particle transport out of the plasma during L-mode and inter-ELM H-mode plasmas [65]. However, while blobs have been measured in many tokamaks [66, 67, 68, 69], they are also evident in other magnetic configurations such as stellarators [70] and linear devices [71]. Additionally, and of particular pertinence to these studies, there is significant study of filament propagation within simple magnetic tori such as the TORPEX device [72, 73].

As blobs are seen across a broad range of magnetic configurations, significant effort has gone into determining the physics behind their behavior. Generally, the research can be divided between that of filament origins and propagation. The research presented within this thesis focuses only on the motion of filaments, and therefore this background will cover only the physics associated with blob propagation. The fundamental physics of blob propagation is described in Figure 2.8.

Diamagnetic drifts (equivalently the ∇B and curvature drifts) cause a charge separation (shown as the grey dipole in Figure 2.8), which causes an electric field to develop. This electric field then gives rise to $\mathbf{E} \times \mathbf{B}$ convection ($\mathbf{v_E}$) in the form of counter-rotating vortices, since a flow develops perpendicular to the dipole electric field. These vortices then drive the filament radially outwards (anti-parallel to $\nabla \mathbf{B}$ and κ). The propagation of filaments once in motion is dependent on the mechanism for the charge separation, which will be discussed shortly.

The primary model for filament propagation was published by Krasheninnikov in 2001 [74] for filaments in tokamaks, and will be reproduced here. For this derivation, the electron temperature T_e is considered constant, and the parallel

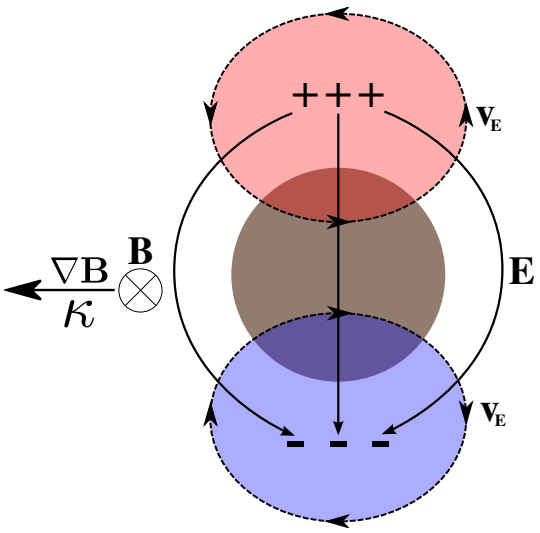

Figure 2.8: Schematic of blob propagation mechanism showing the formation of counter-rotating vortices from diamagnetic drifts

dynamics are neglected – only providing boundary conditions. It is proposed that a quasineutral ($n_i \approx n_e$) filament will have no internal divergence of the current:

$$\nabla \cdot \mathbf{J} = \nabla \cdot \mathbf{J}_\perp + \nabla \cdot \mathbf{J}_\parallel = 0 \tag{2.7}$$

where $\mathbf{J}$ is the current density and $\mathbf{J}_\perp$ and $\mathbf{J}_\parallel$ are the perpendicular and parallel components of the current density. As the motion of blobs is considered to be caused by $\mathbf{E} \times \mathbf{B}$ advection, we write:

$$\frac{\partial n}{\partial t} = -\mathbf{v_E} \cdot \nabla n \tag{2.8}$$

Which is the lowest order of the density continuity equation where n is the density of the blob and $\mathbf{v_E}$ is the $\mathbf{E} \times \mathbf{B}$ velocity. The potential difference (which creates the electric field via $\mathbf{E} = -\nabla\phi$) which forms across the dipole is derived via current balance in Equation 2.7. In Krashenninikov's model, the only perpendicular current is that caused by the curvature and ∇B drifts, allowing us

to write:

$$\nabla \cdot \mathbf{J}_\perp = \nabla \cdot \mathbf{J}_{dia} = \nabla \cdot \left(\frac{\mathbf{B} \times \nabla P}{B^2} \right) \approx \left(\nabla \times \frac{\mathbf{b}}{B} \right) \cdot \nabla P \tag{2.9}$$

where $P = nT$ is the pressure and with:

$$\nabla \times \frac{\mathbf{b}}{B} = \frac{2}{B} \mathbf{b} \times \kappa + \frac{2}{B^2} \mathbf{b} \times \nabla B \tag{2.10}$$

where κ is the curvature vector. This expression (2.10) is just the sum of the curvature and ∇B contributions to the perpendicular current, as discussed in Section 2.2.1. As this is a single-fluid approximation, the species dependence of the drifts is neglected, assuming a single drift direction. Assuming the $\nabla \times \frac{\mathbf{b}}{B}$ contributions are perpendicular to both the radial and parallel directions (and defining this direction to be $\mathbf{z}$), we can write:

$$\nabla \cdot \mathbf{J}_\perp = \left(\nabla \times \frac{\mathbf{b}}{B} \right) \cdot \nabla P \approx \frac{1}{BR} \frac{\partial P}{\partial z} = \nabla_\parallel J_\parallel \tag{2.11}$$

Here, we have defined $\mathbf{b} \cdot \nabla = \nabla_\parallel$, which will be used throughout this thesis for parallel gradients. As stated previously, Krashenninikov assumes minimal variation along the magnetic field, allowing us to integrate along the field line such that:

$$\int_0^{L_\parallel} dl \frac{1}{BR} \frac{\partial P}{\partial z} \approx \frac{L_\parallel}{BR} \frac{\partial P}{\partial z} = \Delta J_\parallel \tag{2.12}$$

where $L_\parallel$ is the parallel connection length between the ends of the filament (which are assumed to be the divertors), and $\Delta J_\parallel$ is the difference between the parallel current density at the two ends (sheaths) of the filament. It is then possible to substitute a relation for the current density at the sheaths, obtained

from [75], and neglecting parallel flow, allowing us to write:

$$\Delta J_{\parallel} \approx -en_t c_s \left(\frac{e\phi}{T_e}\right) \tag{2.13}$$

where e is the electron charge, n_t is the density at the target (divertor), $c_s = \sqrt{T_e/m_i}$ is the sound speed, and ϕ is the potential. Substituting this expression into Equation 2.12 gives:

$$\frac{e\phi}{T_e} = \frac{L_{\parallel} T_e}{BRen_t c_s} \frac{\partial n_b}{\partial z} \tag{2.14}$$

where n_b is the density of the blob. Equation 2.14 provides a relation between the potential difference across the filament and the filament density. We can now determine the $\mathbf{E} \times \mathbf{B}$ velocity and substitute into Equation 2.8. If we assume that the density at the target is some fraction of the blob density, $n_t = \chi n_b$, and we write the resulting equation as a separable ballistic equation: $n_b(x, z, t) = n_b^x(x, t) n_b^z(z)$, where $n_b^z \propto \exp(-z^2/\delta^2)$ with δ being the perpendicular width of the filament and x as the radial coordinate. We then arrive at the following expression describing a filament moving radially:

$$v = c_s \left(\frac{\rho_s}{\delta}\right)^2 \frac{L_{\parallel}}{R} \frac{n_b}{n_t} \tag{2.15}$$

where $\rho_s = c_s/\Omega_i$ is the gyroradius with $\Omega_i = eB/m_i$ describing the gyrofrequency. Equation 2.15 is considered a major result in filament dynamics and is often referred to as the sheath-limited scaling of filament propagation as it assumes the charge separation within the filament is dissipated via the sheath currents. In deriving this expression, however, many parallel dynamics were neglected. In reality, the charge separation can be mitigated by other currents, as described in Figure 2.9.

In a filament, a potential difference is created due to the separation of

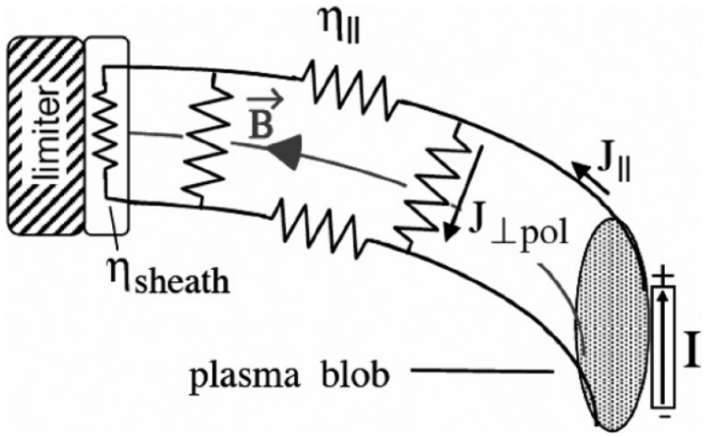

Figure 2.9: Schematic of current dissipation mechanisms in filaments, taken from [76]

charge. Since plasmas are often considered to follow the Boltzmann relation, the potential perturbation is often on the scale of the density perturbation. The way this potential is mitigated determines how the filament is advected. If the parallel resistivity $\eta_{\parallel}$ is high enough, or likewise the connection length $L_{\parallel}$ to the sheath is too long, the blob circuit shown in Figure 2.9 can be short circuited by the polarization current $J_{\perp pol}$. When this occurs, the filament propagation velocity follows a $\delta^{1/2}$ scaling [77], and is considered to be *inertially* limited. By analyzing the filament propagation and the currents within the system, it is possible to determine the blob propagation regime. Section 4.4.1 contains an analysis of the blobs in a poloidal magnetic null point geometry by following these principles. Additionally, the mechanism for charge dissipation is a central question within the research presented in this section, as it helps determine the validity of an analytical model.

2.3.2 Simulating turbulence

As it has become apparent that turbulence is the dominant mechanism for heat and particle transport in plasmas, there has been great effort into researching plasma turbulence. The research presented within this thesis focuses on turbulence modelling in various magnetic geometries. There are several approaches to model plasma turbulence, and they can be distinguished by considering the

different assumptions in deriving the models and consequently the scales involved.

In constructing a description of plasma turbulence, we must begin with finding a fundamental description of plasmas [22]. Due to the number of particles involved, any description must be statistical, therefore we begin by considering a distribution function $f(\mathbf{x}, \mathbf{v}, t)$ which describes the probability density for a particle to exist at time t, with a position $\mathbf{x}$ and a velocity $\mathbf{v}$. We can then write that the distribution function is a function of the particle's position $\mathbf{q} = \mathbf{x}$ and canonical momentum $\mathbf{p} = m\mathbf{v}$ such that $f = f(\mathbf{q}, \mathbf{p})$. In the absence of external sources, the distribution function is assumed to follow a continuity equation:

$$\frac{df}{dt} = -f\left(\frac{\partial}{\partial \mathbf{q}} \cdot \dot{\mathbf{q}} + \frac{\partial}{\partial \mathbf{p}} \cdot \dot{\mathbf{p}}\right) \tag{2.16}$$

where the time derivative on the left hand side is defined as:

$$\frac{d}{dt} = \frac{\partial}{\partial t} + \dot{\mathbf{q}} \cdot \frac{\partial}{\partial \mathbf{q}} + \dot{\mathbf{p}} \cdot \frac{\partial}{\partial \mathbf{p}} \tag{2.17}$$

The right hand side of Equation 2.16 can be shown to be zero by substituting Hamilton's equations:

$$\dot{\mathbf{q}} = \frac{\partial H}{\partial \mathbf{p}}, \qquad \dot{\mathbf{p}} = -\frac{\partial H}{\partial \mathbf{q}} \tag{2.18}$$

Therefore Equation 2.16 becomes:

$$\frac{\partial f}{\partial t} + \dot{\mathbf{q}} \cdot \frac{\partial f}{\partial \mathbf{q}} + \dot{\mathbf{p}} \cdot \frac{\partial f}{\partial \mathbf{p}} = 0 \tag{2.19}$$

Which is a form of the Boltzmann equation. Reminding ourselves that a particle in a plasma is subject to the Lorentz force, Equation 1.3 and that the force exerted on a particle is the time derivative of the momentum (Newton's

Second Law), we write:

$$\dot{\mathbf{p}}_\mathbf{j} = Ze_j \left(\mathbf{E} + \mathbf{v} \times \mathbf{B}\right) \tag{2.20}$$

By substituting this into Equation 2.19, we arrive at the Vlasov equation:

$$\frac{\partial f}{\partial t} + \mathbf{v} \cdot \frac{\partial f}{\partial \mathbf{x}} + \frac{Ze_j}{m_j} \left(\mathbf{E} + \mathbf{v} \times \mathbf{B}\right) \cdot \frac{\partial f}{\partial \mathbf{v}} = 0 \tag{2.21}$$

The Vlasov equation describes the behavior of a collection of particles in a plasma in the absence of collisions. To include collisions, a collision operator C is added which varies based on the type of collisions present. This addition gives the Vlasov-Fokker-Planck equation:

$$\frac{\partial f}{\partial t} + \mathbf{v} \cdot \frac{\partial f}{\partial \mathbf{x}} + \frac{Ze_j}{m_j} \left(\mathbf{E} + \mathbf{v} \times \mathbf{B}\right) \cdot \frac{\partial f}{\partial \mathbf{v}} = C[f_j, f_i] \tag{2.22}$$

We now have an equation which describes the distribution function for a particle species j under the influence of an electric field $\mathbf{E}$, magnetic field B and colliding with species i. This expression is difficult to solve completely, as it is 7-dimensional. As such, it serves as the starting point for many descriptions of plasma. The various descriptions of plasma differ by which assumptions and simplifications of the Vlasov-Fokker-Planck equation are made.

By assuming that electromagnetic field varies significantly across a Larmor orbit and averaging this effect over that orbit (or, *gyro-averaging*), the gyrokinetic equation is obtained. This description focuses on smaller scale effects both in time and space, as numerical simulation of the gyrokinetic equation is computationally expensive. At the moment, this is the only method by which stellarator turbulence is modelled due to the complexity of the nonaxisymmetric magnetic field. The difficulties of simulating nonaxisymmetric fields in fluid simulations will be discussed in depth in Chapter 5. Gyrokinetics are also often used to sim-

ulate core plasmas in tokamaks, as the high temperatures (and low collisionality) prompt a kinetic treatment.

Alternatively, by taking moments of the Vlasov-Fokker-Planck equation, one arrives at a set of fluid equations for both species (electrons and ions). Further simplifications such as quasineutrality ($n_e = n_i$) lead to single fluid equations. This fluid description of plasma assumes that fluctuations occur on scales much larger than a gyroradius, and slower than a gyrofrequency. Fluid turbulence simulations often assume a flute-reduction such that perturbations perpendicular to the magnetic field occur on smaller spatial and temporal scales to those in the parallel direction. This assumption often leads to computation on field-aligned grids, which is impractical in complicated magnetic geometries and will be discussed in more detail in Section 2.4. Fluid descriptions are often used for global plasma edge simulations in tokamaks, as the collisionality is high enough to assume a fluid description.

It is this fluid approach to plasma turbulence simulation that is mainly employed in `BOUT++`. The main advantages are that large scales can be efficiently simulated, while still recovering relevant physics. A brief derivation of the fluid model used in this thesis will be provided in Section 2.5.1.

2.4 BOUT++

To perform the modelling in this research, a framework developed primarily in York called `BOUT++` is used. `BOUT++` is a highly adaptable, modular tool which simulates an arbitrary number of equations in 3D curvilinear coordinates, with the original intention of simulating flute-reduced plasma fluid turbulence models. It is written primarily in C++, although the pre- and post-processing routines are written in Python, IDL, Mathematica and Matlab. Unlike most fluid turbulence codes [78, 79], `BOUT++` does not solve a particular plasma model. Rather, the model (and numerical methods) can be changed. This allows for greater flexibility and adaptability to the physics which is to be investigated. The model implemented for the majority of the simulations presented within this thesis is

described in Section 2.5.1. Some of the advantages of BOUT++ are:

- An object-oriented and modular structure. Users can alter numerical methods, schemes and solvers without altering the core structure of the code. This allows for a greater flexibility and alterations which are specific to the issues to be investigated.

- Generalized differential operators. These operators can be solved in any curvilinear system where the metric tensor varies in two dimensions (this limitation will be addressed in Chapter 5). This allows various geometries to be implemented with minimal alteration to the code.

- A straightforward syntax for model implementation, allowing for simple and natural code implementation.

BOUT++ was originally developed with the intention of solving plasma fluid turbulence models in field aligned coordinate systems. In the context of typical BOUT++ meshes, a field aligned system refers to a coordinate system in which one coordinate is aligned to the magnetic field (typically $\mathbf{y}$ in BOUT++), and another coordinate is radial ($\mathbf{x}$) and one is toroidal ($\mathbf{z}$). This coordinate system allows for stability and efficiency of numerical methods, as the parallel derivatives always lie in only one coordinate direction, and therefore the parallel operators must only be one dimensional. Figure 2.10 illustrates half of a poloidal cross section for a field-aligned mesh of the Mega-Ampere Spherical Tokamak (MAST), which is generated using a common grid generator for BOUT++ called Hypnotoad.

Figure 2.10 quite nicely demonstrates the limits of a field aligned coordinate system. Firstly, this method cannot correctly capture the plasma-surface interaction at divertor strike points. Consider the mesh which covers the outboard divertor leg (magenta). As the coordinate must be strictly radial (technically, perpendicular to flux surfaces), it cannot be aligned to the divertor (shown as a horizontal red line) as the divertor is not aligned perpendicularly to flux surfaces. For this reason, any divertor interactions must be extrapolated.

The treatment of X-points in field-aligned systems is the main motivation for this work. As the field is completely toroidal at the X-point, the field aligned

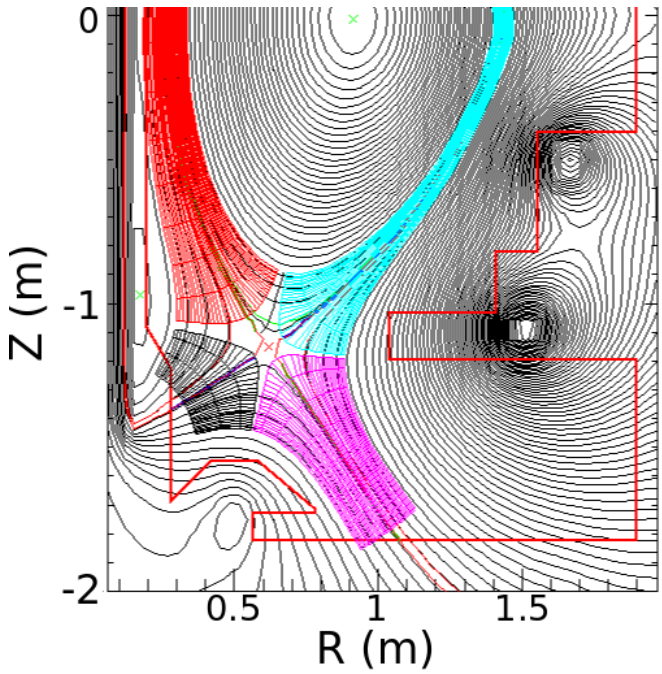

Figure 2.10: The field-aligned coordinate system (black, red, cyan, magenta) within BOUT++, as illustrated in half of a poloidal cross section if the MAST tokamak. The black contour lines illustrate magnetic surfaces, and the red lines at the edges of the figure represent the location of the vacuum vessel.

coordinate system is insufficient since two coordinates (toroidal, field-aligned) are then parallel. This mathematical singularity causes numerical instability in the form of zero volume elements. Instead, the mesh is generated as closely as possible to the X-point without violating the Courant-Friedrichs-Lewy (CFL) condition [80]. While an implicit method is used, small grid cells lead to small timesteps.

The CFL condition imposes a limit on the spacing of grid points when solving partial differential equations using finite difference methods. Heuristically, the limit arises based on the amount of time that a wave propagates across a grid cell. If this time is less than the timestep used in solving the differential equation, the solution cannot be correct.

As a result, there is a significant portion of the computational domain in the magnetic null region where there are no explicit calculations. This could potentially exclude important physics. For instance, there has been a recent proposition of a "churning mode" [81] near poloidal magnetic nulls in tokamaks.

This mode could become important when describing the distribution of heat and particle flux in divertor configurations such as the snowflake [82].

There are several options for coordinate systems which are able to generate a computational mesh which accurately describes the physics near null points. One method which has recently been implemented into BOUT++ through the modification of Hypnotoad, though is not used in this thesis, is the non-orthogonal coordinate system which is shown in Figure 2.11.

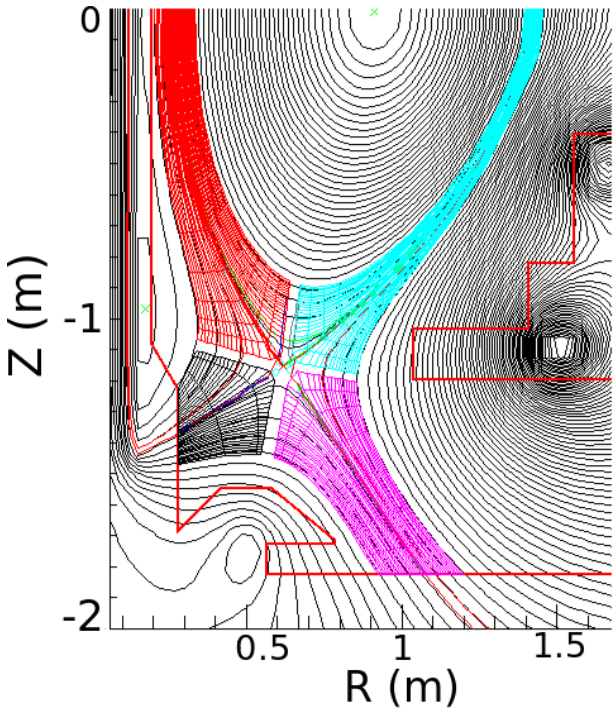

Figure 2.11: The nonorthogonal field-aligned coordinate system (black, red, cyan, magenta) within BOUT++, which is able to more closely model the X-point and include realistic strikepoint coverage.

With the implementation of the nonorthogonal coordinate system illustrated in Figure 2.11, the X-point is more closely (but still not completely) modelled while still maintaining the advantages of field aligned coordinate systems allowing for more efficient computation. This method will not be used within this thesis, but it should be mentioned due to its potential application to X-point and divertor studies.

For the work presented herein, the method of prescribing a Cartesian coordinate system is used. This creates a singularity-free orthogonal coordinate system,

allowing for more flexible magnetic geometries. For this research, the Cartesian coordinate system is imposed such that the **x** direction is now considered horizontal, **z** is vertical, and **y** is toroidal. With this stability comes a few disadvantages. One must be clever in implementing the magnetic geometry. For the work within this thesis, the magnetic field is implemented in two ways. Firstly, an analytical form for the magnetic vector potential is found and the parallel derivatives are modified to include the perpendicular perturbation, as described in Section 2.5.2. Secondly, a new method for parallel derivatives called the Flux Coordinate Independent [83] method has been implemented into `BOUT++`. This method allows for much more complicated magnetic geometries and will be discussed in Section 5.2.

The stability of imposing a Cartesian coordinate system comes a the cost of numerical efficiency. Since the field line no longer lies in a coordinate direction, parallel derivatives are less efficient, as each operation must be a three dimensional operation. The efficiency is also degraded in the case of FCI derivatives, as an interpolation scheme must also be used for each derivative. The advantages and disadvantages of such a system will be explored in Chapter 5.

The original metric tensor in `BOUT++` was implemented to be two dimensional, assuming that there is always a symmetric direction **z**. As such, spectral methods are often used in computing derivatives or operators in the **z** direction such as Laplacian inversion. This is sufficient for axisymmetric tokamak cases, as the toroidal **z** direction is is the direction of symmetry. However, the author of this thesis insists on doing things the difficult way, and the new **z** direction, the vertical direction, has broken the periodic and symmetric nature. As such, a new method for Laplacian inversion must be implemented, as will be discussed in the following section.

2.5 Isothermal model and Numerical methods

The strength of `BOUT++` lies in its flexibility. As we are free to choose a (sensible) plasma model, this section describes the isothermal model which will be utilized in this thesis. Additionally, the modular nature of `BOUT++` allows for the imple-

mentation of new numerical methods. The common numerical methods used in the majority of this thesis are also presented here.

2.5.1 Isothermal model

The research described in Chapters 3 and 4 utilize an isothermal reduced magnetohydrodynamic model which was initially developed for blob studies [84], but has been extended to evolve parallel velocity. For a full description of the derivation, see Nick Walkden's thesis [64], where the original model was derived by following that found in Reference [85, 86]. A brief outline of the derivation will be provided here.

The derivation of this model begins, like many plasma fluid turbulence models, by taking moments of the Vlasov-Fokker-Planck equation (Equation 2.22). We start with the zeroth moment which describes the density continuity for a species j:

$$\frac{\partial n_j}{\partial t} + \nabla \cdot (n_j \mathbf{u_j}) = S_{n,j} \tag{2.23}$$

where n_j is the density, $\mathbf{u_j}$ is the velocity, and $S_{n,j}$ is a source term. The first moment of the Vlasov-Fokker-Planck equation provides the momentum conservation equation:

$$m_j \frac{\partial n_j \mathbf{u_j}}{\partial t} + \nabla p_j + \nabla \cdot \left(\overleftrightarrow{\pi}_j + m_j n_j \mathbf{u_j} \mathbf{u_j} \right) = Z_j e n_j \left(\mathbf{E} + \mathbf{u_j} \times \mathbf{B} \right) + \mathbf{R} + S_{m,j} \tag{2.24}$$

where m_j is the mass, p_j is the pressure, $\overleftrightarrow{\pi}_j$ is the viscous stress tensor, Z_j is the atomic number, and $\mathbf{R_j}$ is the friction force. The displacement term in Ampere's law is neglected here, as in many MHD models. This approximation is valid only for highly conducting fluids at low frequency (less than the plasma frequency). For this derivation there are assumed to be no sources ($S_{n,j} = S_{m,j} = 0$) and a drift ordering scheme is used which assumes:

- The plasma equilibrium exhibits two separable length scales; one with slowly varying quantities L_s and one with fast varying quantities L_f. On both scales, quantities are varying on a timescale such that at each time the plasma is in MHD equilibrium ($\mathbf{J} \times \mathbf{B} = \nabla P$), but this variation is on slow timescales compared to the Alfvén time. Quantities on the slowly varying time scale are assumed to have a large spatial extent, whereas quantities which are quickly varying are assumed to exhibit a small spatial extent. Effectively, this is the separation between the parallel and perpendicular length scales within the scrape off layer, as L_s is assumed to be associated with effects such as the curvature of the equilibrium magnetic field, and L_f is associated with local radial gradients. A small parameter ϵ is defined:

$$\epsilon \equiv \frac{L_f}{L_s} \ll 1 \tag{2.25}$$

- Other assumed small parameters include the plasma β, which is the ratio of the thermal to magnetic pressure:

$$\beta \equiv \frac{2\mu_0 nT}{B_0^2} \ll 1 \tag{2.26}$$

and a collision-dominated, magnetized plasma is assumed such that:

$$\Delta \equiv \frac{\lambda}{L_s} \ll \frac{\lambda}{L_f} \ll 1 \tag{2.27}$$

$$\delta \equiv \frac{\rho}{L_s} \ll 1 \tag{2.28}$$

where λ is the ion-electron mean free path and ρ is the Larmor radius.

- The time scales are assumed to follow the ordering that:

$$\omega \ll \nu \ll \Omega, \omega_{pe} \tag{2.29}$$

where $\omega_{pe} = \sqrt{n_e e^2/m_e\epsilon_0}$ is the plasma frequency, ω is the frequency of the relevant physics, ν is the collision frequency, and Ω is the gyrofrequency. Physically, this means that the plasma is magnetized but still collisional; particles can travel around orbits, but will still experience collisions.

To derive an expression describing the density evolution, we first obtain expressions for the perpendicular flow velocity. By taking the perpendicular component of our momentum conservation equation, Equation 2.24, we begin to see some familiar terms. By noting the following relation:

$$\mathbf{B} \times (\mathbf{u_j} \times \mathbf{B}) = B^2\mathbf{u_j} - (\mathbf{u} \cdot \mathbf{B})\,\mathbf{B} \equiv B^2\mathbf{u}_\perp \tag{2.30}$$

we can arrive at an expression for our total velocity:

$$\mathbf{u} = \mathbf{u}_\parallel + \mathbf{u}_\perp = \mathbf{u}_\parallel + \mathbf{u_d} + \mathbf{u_E} + \mathbf{u_p} \tag{2.31}$$

where we have recovered the diamagnetic velocity:

$$\mathbf{u_d} = \frac{1}{Z_j e n_j}\frac{\mathbf{B} \times \nabla p}{B^2} \tag{2.32}$$

the $\mathbf{E} \times \mathbf{B}$ velocity:

$$\mathbf{u_E} = \frac{\mathbf{B} \times \nabla \phi}{B^2} \tag{2.33}$$

and the polarization velocity:

$$\mathbf{u_p} = \frac{1}{\Omega_j B^2}\mathbf{B} \times \left(\frac{\partial \mathbf{u}}{\partial t} + \mathbf{u} \cdot \nabla \mathbf{u} + \frac{\nabla \cdot \overleftrightarrow{\pi}_j - \mathbf{R_j}}{m_j n_j}\right) \tag{2.34}$$

The drift ordering makes the polarization velocity a small correction to the $\mathbf{E} \times \mathbf{B}$ velocity ($\sim \delta_i^2$), and will be simplified when deriving an expression for vorticity.

This seems as good a time as any to discuss the viscous stress tensor, $\overleftrightarrow{\pi}$. First, we can split this tensor into its parallel, perpendicular, and gyroviscous

components:

$$\overleftrightarrow{\pi} = \overleftrightarrow{\pi}_{\parallel} + \overleftrightarrow{\pi}_{\perp} + \overleftrightarrow{\pi}_{g} \tag{2.35}$$

The perpendicular component describes the resistance of particles to move perpendicularly caused by collisions. The gyroviscous component describes the viscous stress on a rotating fluid element due to its gyro-motion. We will be neglecting the collisional (parallel and perpendicular) components as they are smaller than the gyroviscous part by a factor of $\frac{1}{\Omega_i}$ [87]. For a detailed description of the gyroviscous tensor, see References [88, 89]. When considering many gyro-orbits, the gyroviscous stress creates a net vertical stress. Therefore, to the leading order, the gyroviscous stress tensor is given by [85]:

$$\overleftrightarrow{\pi}_{g} \approx -\mathbf{u}_{d,i} \cdot \nabla \mathbf{u} \tag{2.36}$$

This approximation is often referred to as the gyroviscous cancellation, and is justified in that it removes the divergence free advection due to particle orbits. Quantities are considered not to be advected due to gyromotion, but instead by the guiding center motion described previously. This cancellation removes any effects due to the gyromotion, much like gyroaveraging removes these effects in gyrokinetic and gyrofluid treatments.

Derivation of density continuity

To derive the density equation, we begin by substituting Equation 2.31 into our density continuity expression, Equation 2.23. We neglect the contribution of the polarization velocity as the drift ordering assumes its $1/\Omega_i$ dependence determines that it is m_e/m_i smaller than than $\mathbf{u}_E$ and $\mathbf{u}_d$. Utilizing this assumption, we get:

$$\frac{dn}{dt} + \mathbf{u}_E \cdot \nabla n = -n\nabla \cdot \mathbf{u}_E - \nabla \cdot (n\mathbf{u}_d) - \nabla \cdot \left(n\mathbf{u}_{\parallel}\right) \tag{2.37}$$

It is easiest to evaluate this expression term by term. We will begin now to write our magnetic field vector as $\mathbf{b} = \frac{\mathbf{B}}{B}$. Let's start by simplifying the first term on the right hand side by recalling that the curl of a gradient is exactly zero:

$$\begin{aligned} n\nabla \cdot \mathbf{u}_E &= n\nabla \cdot \left(\frac{\mathbf{b}}{B} \times \nabla\phi \right) = \left(\nabla \times \frac{\mathbf{b}}{B} \right) \cdot n\nabla\phi + n\frac{\mathbf{b}}{B} \left(\nabla \times \nabla\phi \right) \\ &= \left(\nabla \times \frac{\mathbf{b}}{B} \right) \cdot n\nabla\phi \end{aligned} \tag{2.38}$$

We can perform a similar treatment on the second term on the right hand side of Equation 2.37:

$$\begin{aligned} \nabla \cdot (n\mathbf{u}_d) &= \nabla \cdot \left(\frac{\mathbf{b}}{B} \times \frac{\nabla p}{Ze} \right) = \left(\nabla \times \frac{\mathbf{b}}{B} \right) \cdot \frac{\nabla p}{Ze} + \frac{\mathbf{b}}{B} \left(\frac{1}{Ze} \nabla \times \nabla p \right) \\ &= \left(\nabla \times \frac{\mathbf{b}}{B} \right) \cdot \frac{1}{Ze} \nabla p \end{aligned} \tag{2.39}$$

The third and final term on the right hand side of Equation 2.37 can be treated by first considering the electron expression and recalling the definition of a parallel current:

$$\begin{aligned} \nabla \cdot \left(n u_{\parallel,e} \mathbf{b} \right) &= \nabla \cdot \left(n u_{\parallel,i} - \frac{J_\parallel}{e} \right) \mathbf{b} \\ &= \nabla_\parallel \left(n u_{\parallel,i} - \frac{J_\parallel}{e} \right) + \left(n u_{\parallel,i} - \frac{J_\parallel}{e} \right) \nabla \cdot \mathbf{b} \end{aligned} \tag{2.40}$$

where $\nabla_\parallel = \mathbf{b} \cdot \nabla$. We can split the velocity term $\nabla_\parallel n u_{\parallel,i}$ and recall for the second half of the expression that:

$$\nabla \cdot \mathbf{b} = \frac{1}{B} \nabla \cdot \mathbf{B} + \mathbf{B} \cdot \nabla \frac{1}{B} = -\frac{\mathbf{B}}{B^2} \nabla B = -\frac{1}{B} \nabla_\parallel B \tag{2.41}$$

Therefore we can write the parallel component of Equation 2.37 as:

$$\nabla_\parallel \frac{J_\parallel}{e} - n\nabla_\parallel u_{\parallel,i} - u_{\parallel,i} \nabla_\parallel n - \frac{1}{B} \left(n\nabla_\parallel u_{\parallel,i} - \frac{J_\parallel}{e} \right) \nabla_\parallel B \tag{2.42}$$

This gives us the following expression for the density of electrons:

$$\begin{aligned}\frac{dn}{dt} + \mathbf{u}_E \cdot \nabla n = \left(\nabla \times \frac{\mathbf{b}}{B}\right) \cdot \left(\frac{1}{e}\nabla p - n\nabla\phi\right) + \nabla_\parallel \frac{J_\parallel}{e} - n\nabla_\parallel u_{\parallel,i} \\ - u_{\parallel,i}\nabla_\parallel n - \frac{1}{B}\left(n\nabla_\parallel u_{\parallel,i} - \frac{J_\parallel}{e}\right)\nabla_\parallel B\end{aligned} \tag{2.43}$$

We now begin to apply our reductions to this model. Firstly we assume a large aspect ratio, such that $\nabla_\parallel B \to 0$. We also assume an isothermal plasma with cold ions: $T_i \ll T_e \approx constant \Rightarrow p \approx nT_e \Rightarrow \nabla p \approx T_e \nabla n$. Finally, we define our polarization vector $\xi \equiv \nabla \times \frac{\mathbf{b}}{B}$ which defines the direction of charge polarization due to the drifts described earlier in section 2.2.1. Applying these reductions, we arrive at the final form of our density continuity equation:

$$\frac{\partial n}{\partial t} + \mathbf{u}_E \cdot \nabla n = 2c_s\rho_s\xi \cdot (\nabla n - n\nabla\phi) + \nabla_\parallel \frac{J_\parallel}{e} - n\nabla_\parallel u_\parallel - u_\parallel \nabla_\parallel n \tag{2.44}$$

where $c_S = \sqrt{\frac{T_e}{m_i}}$ is the sound speed, $\rho_s = \frac{c_s}{\Omega_i}$ is the gyro radius, and $\Omega_i = \frac{eB}{m_i}$ is the cyclotron frequency.

Derivation of the vorticity equation

Next, we can derive an expression for vorticity by considering the ambipolarity condition $\nabla \cdot \mathbf{J} = 0$ where $\mathbf{J} = Zne\,(\mathbf{u_i} - \mathbf{u_e})$. For this derivation, we will assume a hydrogen plasma such that $Z = 1$. We can then expand the electron and ion velocities into the components as described in Equation 2.31 in order to write:

$$-\nabla_\parallel J_\parallel = \nabla \cdot (ne[\mathbf{u}_{d,i} - \mathbf{u}_{d,e}]) + \nabla \cdot [en\,(\mathbf{u}_{p,i} - \mathbf{u}_{p,e})] \tag{2.45}$$

We note that the first term on the right hand side of Equation 2.45 has a similar form to Equation 2.39, which allows us to write:

$$\nabla \cdot (ne\mathbf{u}_{d,i} - \mathbf{u}_{d,e}) = \left(\nabla \times \frac{\mathbf{b}}{B}\right) \cdot \nabla\,(p_i + p_e) \tag{2.46}$$

To simplify the second term in the right hand side of Equation 2.45, we

recall our expression for the polarization velocity, Equation 2.34. As the inertial part of this velocity is dependent on $1/\Omega_j$, it is clear that the electron polarization is smaller than the ion polarization by a factor of m_e/m_i and therefore can be neglected. The electron-ion friction term, $\mathbf{R}_j$ is written as:

$$\mathbf{R}_e = -\mathbf{R}_i = en\left(\frac{\mathbf{J}_\parallel}{\sigma_\parallel} + \frac{\mathbf{J}_\perp}{\sigma_\perp}\right) \tag{2.47}$$

where nonisothermal terms have been neglected. Therefore, the friction terms in the polarization current cancel. Finally, we use the gyroviscous approximation to leave only the leading order for the viscous stress tensor, allowing us to write:

$$\nabla \cdot (ne\mathbf{u}_{p,i} - \mathbf{u}_{p,e}) = \nabla \cdot \left[\mathbf{b} \times \left(\frac{1}{\Omega_i} n \frac{\partial}{\partial t}\mathbf{u}_i - \mathbf{u}_{d,i} \cdot \nabla \mathbf{u}\right)\right] \tag{2.48}$$

To write our perpendicular components of the velocity, we first remind ourselves that the polarization current is small by a factor of $\frac{1}{\Omega_i}$, and therefore is neglected. Therefore our perpendicular velocities are simply the $\mathbf{E} \times \mathbf{B}$ and diamagnetic components, which allows us to write:

$$\mathbf{b} \times \mathbf{u}_i = -\frac{1}{B}\nabla_\perp \phi - \frac{1}{neB}\nabla_\perp p_i \tag{2.49}$$

Next, we substitute this expression into Equation 2.48 and exploit the Boussinesq approximation [90] such that $\nabla \cdot (n\partial_t \nabla_\perp \phi) \sim n\partial_t \nabla_\perp^2 \phi$. This approximation is commonly used in fluid turbulence simulations and limits the size of the density perturbation above the background. This approximation has been shown to be valid in scrape-off-layer turbulence simulations, as its inclusion introduces only a small discrepancy [91]. We also utilize the isothermal approximation and normalize our potential to the electron temperature $T_e(eV)$ to write the po-

larization current as:

$$\nabla \cdot (ne\mathbf{u}_{p,i} - \mathbf{u}_{p,e}) = -\frac{T_e}{B\Omega_i} n \frac{d\omega}{dt} \tag{2.50}$$

where $\omega = \nabla_\perp^2 \phi$ is the vorticity, and the advective derivative $\frac{d}{dt}$ is written:

$$\frac{d}{dt} = \frac{\partial}{\partial t} + \mathbf{u}_E \cdot \nabla + \mathbf{u}_\parallel \cdot \nabla \tag{2.51}$$

We again use the definition of our polarization vector $\xi \equiv \nabla \times \frac{\mathbf{b}}{B}$ and substitute Equations 2.50 and 2.46 into Equation 2.45 to give an expression for vorticity:

$$\frac{T_e}{B\Omega_i} n \frac{d\omega}{dt} = T_e \xi \cdot \nabla n + \nabla_\parallel J_\parallel \tag{2.52}$$

Dividing through by e and utilizing our expressions for ρ_s, c_s and Ω_i, we arrive at the final form for our vorticity:

$$\rho_s^2 n \frac{d\omega}{dt} = 2c_s \rho_s \xi \cdot \nabla n + \nabla_\parallel \frac{J_\parallel}{e} \tag{2.53}$$

Derivation of the parallel Ohm's law and the parallel velocity equation

As the research presented within this thesis is focused on turbulence in poloidal magnetic null regions, the parallel dynamics must be considered. As such, we will derive expressions for the parallel version of Ohm's law and the parallel velocity. We begin by deriving an expression for Ohm's law by considering the parallel projection of our electron momentum expression, neglecting inertial and viscous

terms:

$$T_e \nabla_\parallel n + en\nabla_\parallel \phi = \mathbf{b} \cdot \mathbf{R}_e \tag{2.54}$$

By substituting Equation 2.47 and normalizing the plasma potential to the electron temperature (in eV), we arrive at:

$$J_\parallel = \frac{\sigma_\parallel T_e}{en}(\nabla_\parallel n - n\nabla_\parallel \phi) \tag{2.55}$$

which is the electrostatic version of Ohm's law parallel to the magnetic field.

To derive an expression for the parallel velocity, we begin similarly by considering the parallel projection of the ion momentum expression:

$$\frac{\partial m_i n u_\parallel}{\partial t} + \mathbf{b} \cdot \nabla \cdot \left(\overleftrightarrow{\pi}_i + m_i n \mathbf{u}_i \mathbf{u}_i \right) + en\nabla_\parallel \phi - \mathbf{b} \cdot \mathbf{R}_i = 0 \tag{2.56}$$

This can be simplified by considering $\mathbf{R}_e = -\mathbf{R}_i$ and substituting Equation 2.54 to get:

$$\frac{\partial m_i n u_\parallel}{\partial t} + T_e \nabla_\parallel n + \mathbf{b} \cdot \nabla \cdot \left(\overleftrightarrow{\pi}_i + m_i n \mathbf{u}_i \mathbf{u}_i \right) + en\nabla_\parallel \phi - \mathbf{b} \cdot \mathbf{R}_i = 0 \tag{2.57}$$

Expanding the time derivative and substituting in the density continuity equation (Equation 2.23) gives:

$$\frac{\partial m_i n u_\parallel}{\partial t} = n m_i \frac{\partial u_\parallel}{\partial t} - m_i \mathbf{b} \cdot \mathbf{u}_i \nabla \cdot (n \mathbf{u}_i) \tag{2.58}$$

We can now combine the second hand on the right hand side of Equa-

tion 2.58 with the fourth term in Equation 2.57, which gives:

$$\mathbf{b} \cdot [\nabla \cdot (m_i n \mathbf{u}_i \mathbf{u}_i) - m_i \mathbf{u}_i \nabla \cdot (n \mathbf{u}_i)] = \mathbf{b} \cdot [n m_i \mathbf{u}_i \cdot \nabla \mathbf{u}_i] = n m_i \mathbf{u}_i \cdot \nabla u_\parallel \quad (2.59)$$

Finally, we again use only the lowest order of the gyroviscous stress tensor so that:

$$\mathbf{b} \cdot \nabla \cdot \overleftrightarrow{\pi} \approx -\mathbf{u}_{d,i} \cdot \nabla u_\parallel \quad (2.60)$$

Combining Equations 2.58, 2.59 and 2.60 into Equation 2.57, we arrive at the final expression for our parallel velocity evolution:

$$\frac{du_\parallel}{dt} = -\frac{c_s^2}{n} \nabla_\parallel n \quad (2.61)$$

Where we have again used the form for the total advective derivative, Equation 2.51.

Model summary

In the interest of energy conservation, the density should be considered constant in terms where it is not differentiated. This is essentially an outcome of the Boussinesq approximation ($\nabla \cdot (n d_t \nabla_\perp \phi) \sim n_0 d_t \nabla_\perp^2 \phi$). Section 3.3.3 includes a more complete consideration of the energy dynamics within this model. The complete model which has been derived is summarized below, which evolves:

Density continuity:

$$\frac{dn}{dt} = 2 c_s \rho_s \xi \cdot (\nabla n - n_0 \nabla \phi) + \nabla_\parallel \frac{J_\parallel}{e} - n_0 \nabla_\parallel u_\parallel \quad (2.62)$$

Vorticity:

$$\rho_s^2 n_0 \frac{d\omega}{dt} = 2 c_s \rho_s \xi \cdot \nabla n + \nabla_\parallel \frac{J_\parallel}{e} \quad (2.63)$$

Parallel velocity:

$$\frac{du_\parallel}{dt} = -\frac{c_s^2}{n_0}\nabla_\parallel n \tag{2.64}$$

Ohm's law:

$$J_\parallel = \frac{\sigma_\parallel T_e}{e n_0}(\nabla_\parallel n - n_0 \nabla_\parallel \phi) \tag{2.65}$$

Here the advective derivative is given as $\frac{d}{dt} = \frac{\partial}{\partial t} + \mathbf{u}_E \cdot \nabla + \mathbf{u}_\parallel \cdot \nabla$. We have also defined the vorticity as $\omega = \nabla_\perp^2 \phi$, and our polarization vector $\xi \equiv \nabla \times \frac{\mathbf{b}}{B}$. This model is isothermal, electrostatic, inviscid, and employs the Boussinesq approximation.

The treatment of each species in this model should be clarified. As the assumption of quasineutrality ($n_i \approx n_e$) has been made, the density evolution (Equation 4.1) holds for both electron and ion densities. The electron velocity was used in describing parallel advection, as electrons are considered to be much more mobile than ions. Equation 4.3, however, describes only the evolution of parallel ion velocity, and the parallel current is used as a representation of the electron velocity. As the parallel current is not evolved, the expression is used simply for closure. Ultimately, perpendicular velocity including the effects of species dependent phenomena such as the diamagnetic current is not evolved, but parallel velocity is. This model describes effects for both ions an electrons, but not separately.

Having derived the model used in the following two chapters, it is now useful to discuss numerical methods which will allow us to properly simulate the physics of plasma turbulence in the regions of magnetic null points.

2.5.2 Common numerical methods

For the first two chapters of this thesis, parallel derivatives are implemented by modifying the form of the parallel gradient operator, $\nabla_\parallel$, such that it includes the contributions from the relatively small perpendicular (azimuthal in Chapter 3 and poloidal in Chapter 4) magnetic field. These perpendicular magnetic fields are

implemented by prescribing an analytic form for the magnetic vector potential and modifying the parallel gradient operator. To determine the form of the magnetic vector potential, we start with the general form of magnetic vector potential in an unbounded space [92]:

$$\mathbf{A}(\mathbf{r}) = \frac{\mu_0}{4\pi} \int \frac{\mathbf{J}(\mathbf{r}')}{|\mathbf{r} - \mathbf{r}'|} d^3 r' \tag{2.66}$$

As we can exploit symmetry in both chapters (longitudinal in Chapter 3 and toroidal in Chapter 4), we find that $\mathbf{A}$ must be the same at a given distance $\mathbf{r}$ from a current carrying wire. Thus, assuming a constant current in the wire we arrive at the Biot-Savart law:

$$\mathbf{A}(\mathbf{r}) = \frac{-\mu_0 I}{2\pi} \ln(r) \hat{\mathbf{y}} \tag{2.67}$$

where $\hat{\mathbf{y}}$ is the longitudinal or toroidal direction (parallel to wire). It is therefore possible to construct an arbitrary magnetic field given the number of turns, current, and location of magnetic coils. The only difficulty is the infinite magnetic field on axis, which is avoided using a penalization scheme, as described later in section 4.3.2. Our form of the vector potential can therefore be implemented into our simulations as the $\mathbf{b} \cdot \nabla$ operator such that:

$$\mathbf{b} \cdot \nabla f = \nabla_{\parallel} f - \left[\frac{A_{ext}}{B}, f \right] \tag{2.68}$$

where A_{ext} is the perturbed externally applied vector potential due to the magnetic coils and the square brackets are Poisson brackets which are solved using the Arakawa method [93].

Due to the highly modular nature of `BOUT++`, the majority of solvers and operators within `BOUT++` can be altered as user input. There are a few options which are common to all of the research presented within this thesis. Time

integration was implemented using the implicit time integration solver CVODE, within the SUite of Nonlinear and DIfferential/ALgebraic equation Solvers (SUNDIALS) [94]. For the first two chapters, the Laplacian solver, which calculates potential (ϕ) from vorticity (ω), in BOUT++ was altered to invert using discrete sine transforms in the z (vertical) direction, which eliminates the periodicity inherent in typical Laplacian inversion utilizing full Fourier transforms. The Laplacian solver has also been altered to invert using discrete cosine transforms, allowing for arbitrary-value boundary conditions, but this method was not used for the results presented here.

We have now discussed the motivation and methods for simulating plasma turbulence in magnetic null point regions in tokamaks. A brief description of the transport mechanisms in tokamaks has been presented, and we have seen that the turbulent dynamics near X-points in modern tokamaks could have a significant influence on the heat and particle deposition onto plasma facing components. The BOUT++ framework has been introduced, and its limitations in magnetic null point configurations have been addressed. With typical BOUT++ field-aligned simulations, X-point dynamics must be interpolated based on nearby flux surfaces. The implementation of a Cartesian coordinate system allows for simulation of plasma turbulence in the presence of magnetic null points. We have derived an isothermal reduced magnetohydrodynamic model and discussed the numerical methods which allow us to implement this model in BOUT++. The following two chapters will describe the research which has contributed toward the understanding of turbulence and transport in the regions of magnetic X-points, by first considering a linear geometry in order to test the aforementioned numerical methods before including curvature in toroidal X-point configurations.

Chapter 3

X-points in linear geometries

3.1 Introduction

This chapter describes simulations performed as part of a feasibility study for a university scale linear plasma device which is capable of producing an azimuthal magnetic null region, and most of which is published with coauthors in [1]. The motivation for this research was to find a suitably accessible device to study fusion-relevant divertor scenarios. Future fusion devices will have unacceptably high heat fluxes [49, 50]. At the moment, the solution for ITER is to operate in a partially detached regime. Additionally, there are investigations into altering the magnetic geometry in tokamaks to mitigate the high heat loads [51, 52]. This linear device would provide a directly accessible, easily diagnosed machine for alternate divertor and detachment relevant plasma scenarios.

As discussed previously, typical `BOUT++` three dimensional turbulence simulations use field-aligned coordinate systems, which have singularities at X-points. Here, the linear geometry provides the simplest geometry in which to test the implemented Cartesian coordinate system and the associated method for calculating parallel derivatives. This is the first chapter which implements the method of modifying the parallel gradient operator such that:

$$\nabla_{\parallel}(f) \rightarrow \nabla_{\parallel}(f) - \left[\frac{A_{\parallel}}{B}, f\right] \tag{3.1}$$

where $A_{\parallel}$ is the imposed magnetic vector potential by which X-point fields are incorporated. By implementing this method in linear geometries, it is possible to test the efficacy and stability of the method while providing meaningful results for future experimental investigations.

This chapter is arranged as follows. The geometry and fluid model used in the following turbulence simulations are given in Section 3.2. Section 3.3 compares the turbulence characteristics and energy dynamics of a simple linear device to those of a device with X-point azimuthal fields. Previous work in linear configurations is confirmed and proposed measurements and dynamics in future devices are given. Finally, section 3.4 asserts our conclusions and discusses future work.

3.2 Simulation geometry and model

3.2.1 Geometry and coordinate system

As an initial study into X-point simulation in `BOUT++`, we have considered a hypothetical linear plasma device capable of producing azimuthal magnetic null points, as shown in Figure 3.1. The machine parameters are chosen as part of a feasibility study into a hypothetical university-scale experiment capable of producing X-points for tokamak-relevant scenarios. The study of tokamak divertor-relevant scenarios is becoming increasingly important and has led to the proposal of multiple test facilities [95, 96, 97]. This machine would allow for direct investigation of fundamental plasma physics associated with tokamak divertor regions and allow simple diagnostic access to an azimuthal magnetic null region, an area which is currently poorly understood. The machine parameters were chosen based on those achieved in previous machines such as those in References [98, 99]. This device is proposed to produce low temperature, high density plasmas relevant to detachment and divertor-relevant scenarios. The electron temperature will be simulated as $T_{e0} \sim 2\text{eV}$, which is relevant for tokamak divertors in detached configurations and typical for linear devices as parallel streaming limits the maximum electron temperatures which can be achieved. The machine will achieve densi-

ties of up to $10^{19}\mathrm{m}^{-3}$, as in previous machines [98, 100], for detachment-relevant scenarios. The initial plasma minor radius was considered to be 5cm. The axial magnetic field is $B_0 \sim 0.2 - 0.3\mathrm{T}$. An additional azimuthal field is created by longitudinal wires which can create X-point fields of approximately $B_{ext} \sim 0.02\mathrm{T}$ at the edge of the simulation domain, which corresponds to a current of about 300A in the internal X-point wires, which are considered to be 18-turn coils. More exotic configurations such as the snowflake [82] can easily be reproduced by the inclusion of more longitudinal wires. It should be noted that the interchange drive will not be present in this configuration, as there is no curvature, except for small local curvature in the perturbed (X-point) field. While this means that this machine will have different turbulent characteristics to a tokamak, it is still capable of producing tokamak-relevant studies applicable to divertor areas, as other turbulent modes such as driftwaves are still present. Therefore, the study of the interaction of turbulence with neutral gas and the influence of turbulence on detachment would be possible.

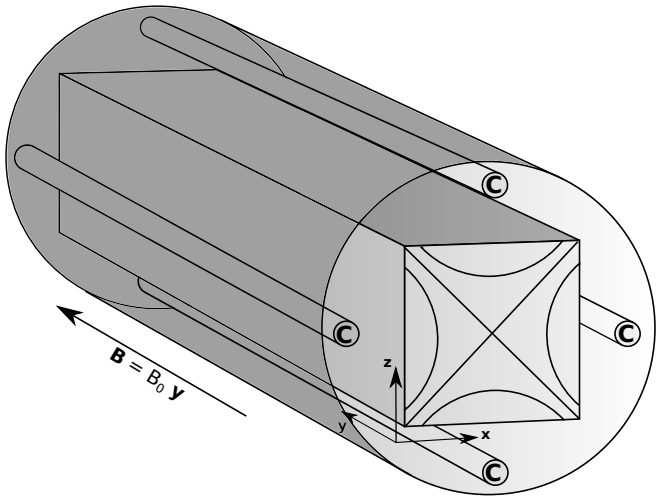

Figure 3.1: Schematic of proposed device showing vessel and X-point coils. Cartesian coordinate system measuring 30cm x 30cm x 3m shown inlaid within the vessel. The four X-point coils are labelled with a 'c'.

In most 3 dimensional turbulence simulations in `BOUT++`, a field-aligned coordinate system is used in the interest of numerical efficiency [101]. In these systems, one coordinate is radial, one is toroidal, and one lies in the direction of the magnetic field. This method cannot be used to explicitly model X-points,

where the field is completely toroidal, as this introduces zero-volume elements where two coordinates are parallel. To ameliorate these issues, we have imposed a Cartesian coordinate system, as shown in the center of the machine pictured in Figure 3.1. The implementation of this coordinate system ensures that there are no zero volume elements, as each dimension is perpendicular to the other two, and therefore X-points (and any other singularities) can be effectively incorporated. The main disadvantages of this method are the potential lower accuracy at a given resolution and the pollution of parallel and perpendicular derivatives. These disadvantages were mitigated by performing simulations at high resolution with a relatively small perpendicular field.

Figure 3.1 also illustrates the shape of the external field used to simulate X-point scenarios. This field was considered to be of the form shown in equation 3.2 [82], where $\theta = tan^{-1}\left(\frac{z}{x}\right)$ is the azimuthal angle. The magnitude and specific geometry of this field can be arbitrarily chosen by altering A_0, the exponent of r and corresponding coefficient of θ. For instance, changing the exponent of r and coefficient of θ to 3 would give a perfect snowflake configuration (likewise 4 will give a cloverleaf).

$$A_{ext} = A_0 r^2 cos(2\theta) \tag{3.2}$$

The expression in Equation 3.2 then creates a perturbed field, as $\mathbf{B}_\theta = \nabla \times \mathbf{A}_{ext}$. The implementation of this perturbed magnetic field into parallel gradient operators is described in section 3.2.3.

3.2.2 Model modifications and numerical methods

The simulations in this Chapter are performed using the isothermal model described in section 2.5.1 in a linear geometry, and therefore any terms involving curvature are neglected in the following analysis ($\xi \equiv \nabla \times \frac{\mathbf{b}}{B} \rightarrow 0$). While this model includes several simplifications, it still captures relevant physics such as Kelvin-Helmholtz and driftwave turbulence, an important class of instabilities in

tokamak edge plasmas [102], as driftwaves are a ubiquitous instability. It should be noted that for this chapter, the density is written with a capital N, as the lower case is reserved for the longitudinal mode number, n, which will be discussed later. The complete set of equations which are solved are as follows in SI units:

Density continuity equation:

$$\frac{dN}{dt} = \nabla_\parallel \frac{J_\parallel}{e} - N_0 \nabla_\parallel u_\parallel \tag{3.3}$$

Vorticity:

$$\rho_s^2 N_0 \frac{d\omega}{dt} = \nabla_\parallel \frac{J_\parallel}{e} \tag{3.4}$$

Parallel velocity:

$$\frac{du_\parallel}{dt} = -\frac{c_s^2}{N_0} \nabla_\parallel N \tag{3.5}$$

Ohm's law:

$$J_\parallel = \frac{\sigma_\parallel T_{e0}}{e N_0} (\nabla_\parallel N - N_0 \nabla_\parallel \phi) \tag{3.6}$$

Where $\omega \equiv \nabla_\perp^2 \phi$ is vorticity, total derivatives are split via $\frac{d}{dt} = \frac{\partial}{\partial t} + \mathbf{u_E} \cdot \nabla + \mathbf{u}_\parallel \cdot \nabla$, and parallel derivatives are defined as $\nabla_\parallel = \mathbf{b} \cdot \nabla$ – however the exact form of this operator must incorporate the X-point field, as discussed in the following section. In the above equations, $\rho_s = \frac{c_s}{\Omega_i}$ is the Bohm gyroradius. These equations are normalized such that density (N) is normalized to $N_0 = 5 \times 10^{18} m^{-3}$, speeds are normalized to the sound speed, and $\phi = \frac{e\Phi}{T_{e0}}$ is the normalized electrostatic plasma potential. The isothermal electron plasma temperature T_{e0} is chosen to be 2eV. The boundary conditions for the simulations presented here will be discussed in section 3.3.

This model differs from that used in reference [84] in that it incorporates parallel ion free streaming, $u_\parallel$, as parallel flows are vital when determining the effects of X-points. Additionally, energy conservation required the restriction

that density N is considered constant (N_0) in terms where it is not differentiated. This is essentially an outcome of the Boussinesq approximation, as discussed in Section 2.5.1. See Section 3.3.3 for a full discussion on the energy dynamics within the system.

3.2.3 Numerical Methods

This model was solved for the system described in section 3.2.1 using a resolution of 1.15mm ($1.25\rho_s$) in the plane perpendicular to $\mathbf{B}$ (x, z), and 8cm ($90.4\rho_s$) in direction parallel to $\mathbf{B}$ (y). The longitudinal direction was chosen to have a relatively low resolution, as fine structure dynamics were expected to be more dominant in the perpendicular planes. Previous studies of linear devices [103] have also indicated that low axial wave-numbers are dominant in linear configurations. Additionally, Alfvén length scales ($\frac{V_A}{\Omega_{ci}}$) are about 20cm, and therefore these dynamics are adequately resolved, as Alfvén wave transit times are shorter than perpendicular drift dynamics.

The parallel dynamics introduced by the imposed X-point field were implemented by altering the $\mathbf{b}\cdot\nabla$ operator such that $\nabla_\parallel(f) \rightarrow \nabla_\parallel(f) - \left[\frac{A_\parallel}{B}, f\right]$, where the brackets indicate Poisson brackets, which were calculated using the Arakawa method [93]. Here it was assumed that the perturbed magnetic field is given by: $\widetilde{\mathbf{b}} = \nabla \times \left(A_\parallel b_o\right) \approx b_0 \nabla A_\parallel$.

The simulation domain was chosen to exclude the in-vessel coils as the magnetic field is infinite on the axis of an infinitesimally thin wire, and therefore causes a numerical instability. Furthermore, the solid-density coils create difficulty when simulating them next to plasma-density regions. These issues can be overcome by introducing a penalization scheme [104], which has been successfully achieved in `BOUT++` and will be described in Chapter 4.

3.3 Simulation analysis

3.3.1 Implementation and behavior

The model represented by Equations 3.3 - 3.6 was implemented into `BOUT++` and simulations were performed with and without an externally applied X-point field. The plasma source was modelled as a constant flow at the sound speed into the domain from one of the longitudinal boundaries ($y = 0$), as this mimics the plasma source used the current York Linear Plasma Device [105]. The opposing longitudinal boundary was considered to have zero-gradient boundary conditions in cases both with and without an imposed X-point. In cases with an X-point, sheath boundary conditions pertinent to presheath entrance as found in reference [106] were implemented. These boundary conditions are modified Bohm boundary conditions which account for the oblique magnetic fields at the Chodura sheath. As these boundary conditions rely on an oblique magnetic field, they could not be imposed in a basic linear case without an externally applied field, as the field lines are parallel to the wall. As such, these cases were constrained to zero-gradient boundary conditions on all fields in the directions perpendicular to the magnetic field ($\mathbf{x}, \mathbf{z}$).

Figure 3.2 shows the time evolution of the total energy of the fluctuations, which will be discussed later in Section 3.3.3. The simulations begin with an initial perturbation, and fluctuations grow until reaching a saturated stage. This state is considered turbulent as the profile has reached an average equilibrium, but fluctuations around that mean profile persist. Furthermore, there is an excitation of energy at various scales, and an exchange of energy between these scales, which will be discussed later in section 3.3.3. This stage is shown as the flat section in Figure 3.2. All analysis presented in this work has been conducted within this regime.

Figure 3.3 illustrates the mean radial density profiles both with (solid) and without (dotted) an X-point at various locations along the length of the device. The radial profiles in each case is taken along a diagonal ($x = z$) line across the azimuthal plane which lies on the X-point. Figure 3.3 indicates that the

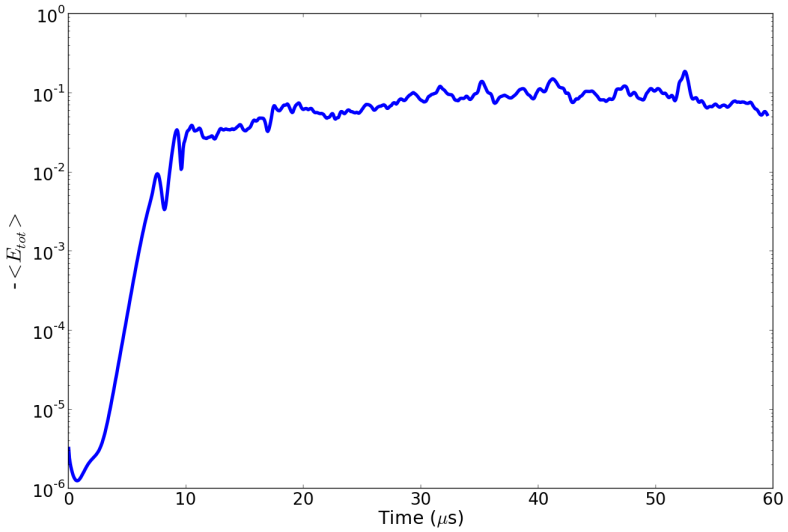

Figure 3.2: Time evolution of the volume averaged total dissipation $(-\langle E_{tot} \rangle)$ in a case without an X-point. For reference, the ion gyroperiod is 59ns.

introduction of a magnetic X-point introduces an asymmetric off-axis peak of density and a narrowing of the total profile.

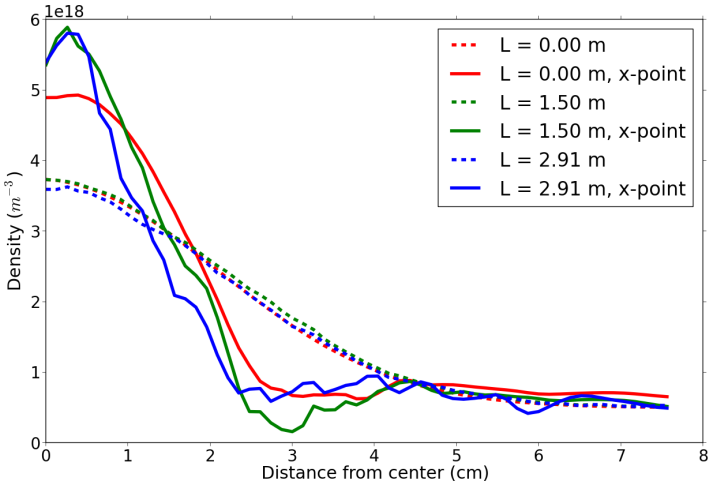

Figure 3.3: Time averaged radial density profiles along a diagonal in the azimuthal plane with (solid) and without (dotted) an X-point applied.

The narrowing of the profiles induced by the X-point as shown in Figure 3.3 can be attributed to the externally applied azimuthal magnetic field, which is

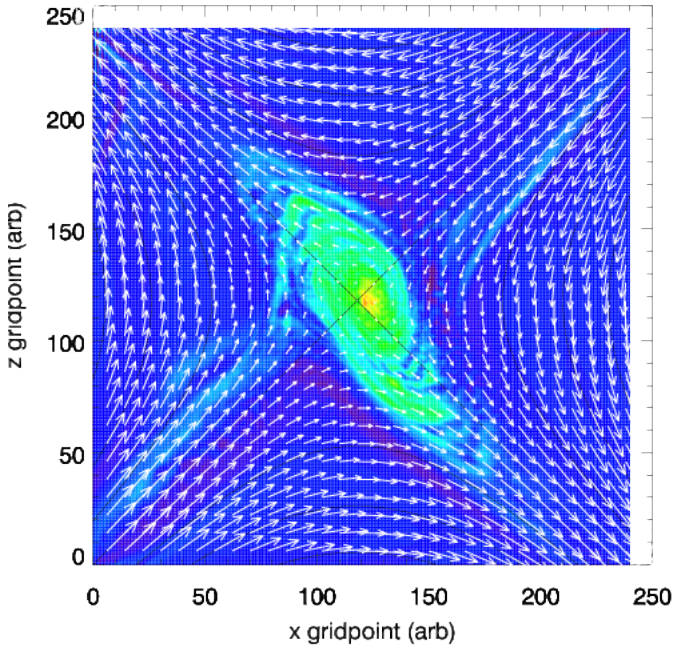

Figure 3.4: Density contour at y=1.5m with overlaid magnetic field, indicating an asymmetric profile in the azimuthal plane.

shown in Figure 3.4. The profile is distorted due to the external magnetic field which maps a circular input profile to an elongated profile at the opposite (sheath) end. This can be described by simply following field lines. Consider a test particle which moves along the axis of the machine. Along the magnetic axis of the machine, the perturbed field shifts the total magnetic field such that it is closer to the null point in two directions (top right and bottom left in Figure 3.4). This therefore creates a narrowing of the profiles in that direction. Likewise the opposite occurs in the other two directions, creating a broadened radial density distribution. Finally, Figure 3.3 also indicates that the radial density profiles are smoother without an X-point field applied. This could perhaps be explained by considering the cross field transport introduced by the X-point which inhibits the azimuthal flow of plasma, breaking up coherent structures.

3.3.2 Transport and cross correlation

As this device is intended to be relevant to configurations such as the snowflake divertor, the flow dynamics near the azimuthal magnetic null region are important to determine. To study the parallel dynamics of the system, a cross correlation analysis was employed. The inbuilt cross correlation function in IDL was used to compute the cross correlation (P_{fg}) of two quantities f and g using the method shown in Equation 3.7. Here k is the index for each population and M is the number of elements in said population.

$$P_{fg} = \sum_{k=0}^{M-1} (f_k - \overline{f})(g_k - \overline{g}) \left\{ \left[\sum_{k=0}^{M-1} (f_k - \overline{f})^2 \right] \left[\sum_{k=0}^{M-1} (g_k - \overline{g})^2 \right] \right\}^{-\frac{1}{2}} \tag{3.7}$$

Using this method, one can determine the correlation between two quantities at different points within the domain. This serves as a convenient method to visualize flow dynamics, as shown in Figure 3.5, which shows the two dimensional cross correlation of density perturbations in an azimuthal plane at the center of the machine ($y = 1.5$m) when an X-point field is applied. The reference point for the cross correlation in Figure 3.5 is shown in black near the null region. This analysis is dependent on the choice of the reference point, however the general trend remains that perturbations are correlated along field lines, and not very well correlated across field lines. This then indicates the nature of transport in the system. This figure illustrates the effects of an induced X-point on parallel dynamics, as transport along field lines is apparent. A correlation in density perturbations indicates that the fluctuations in one region are related to those in another. Furthermore, perturbations on neighboring field lines are not very well correlated, indicating a lack of transport in that direction.

Figure 3.6 plots the cross field flux (Γ) when an X-point is applied, given by $\Gamma = \langle N v_\perp \rangle$ where $v_\perp = \frac{|\mathbf{b} \times \nabla \widetilde{\phi}|}{B}$ and $\widetilde{\phi} = \phi - \langle \phi \rangle$. The cross field flux indicates the regions of high cross field transport, which is an important factor in the effectiveness of novel divertor configurations such as the snowflake or cloverleaf [82], since it determines how effectively heat and particle flux will be distributed across

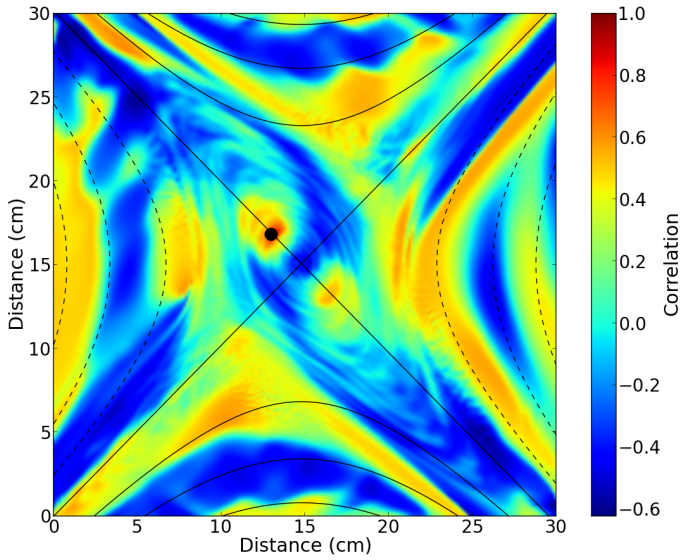

Figure 3.5: Two dimensional cross correlation of density fluctuations at y=1.5m, reference point shown as black dot.

additional divertor legs.

Figures 3.5 and 3.6 indicate two characteristics of note. Firstly, Figure 3.5 indicates that away from the null point, perturbations are highly correlated along field lines, but adjacent areas perpendicular to field lines are less correlated, as indicated by the change from highly correlated (orange) to weakly correlated (blue). Secondly, Figure 3.6 indicates that the null point is the main area of cross-field transport allowing plasma to flow from one region to another. This figure also indicates a two-fold symmetry, since the structure of the magnetic field (as seen in Figure 3.4) introduces a preferred direction which is also apparent in the density profile.

To visualize the full dynamics of the machine, a three dimensional cross correlation was performed for both cases using the same method as before (Equation 3.7). By analyzing correlations in three dimensions, it is possible to determine the dynamics along the length of the machine and visualize the plasma profile, as shown in Figures 3.7 and 3.8. The perturbed plasma profiles induced by the external X-point field is most apparent when visualizing using the three dimensional cross correlation.

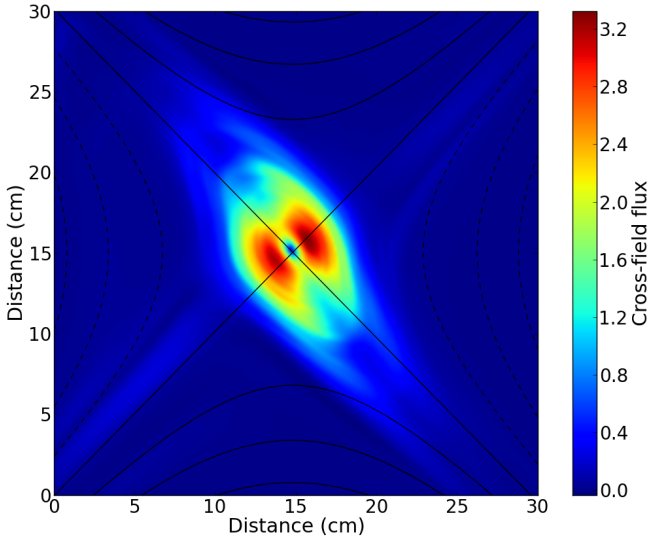

Figure 3.6: Cross field flux at y=1.5m, indicating that the center of the machine is the dominant area for cross-field transport.

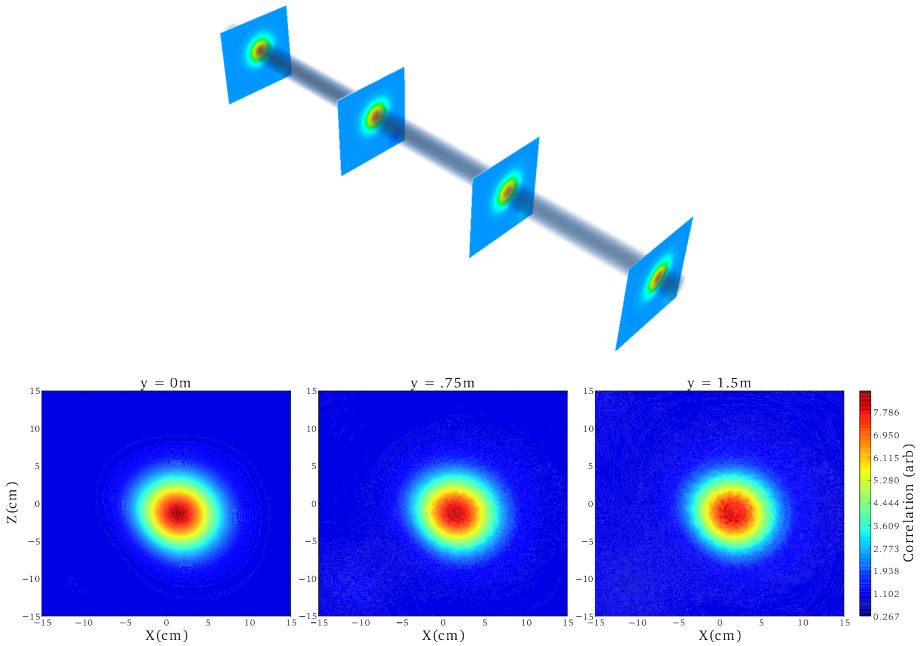

Figure 3.7: Three dimensional cross correlation of a basic linear plasma, and slices at various longitudinal positions. The plasma is relatively uniform along the length of the device.

In these cross correlations, a point was chosen in the middle of the computational domain, and Equation 3.7 was employed to calculate the correlation

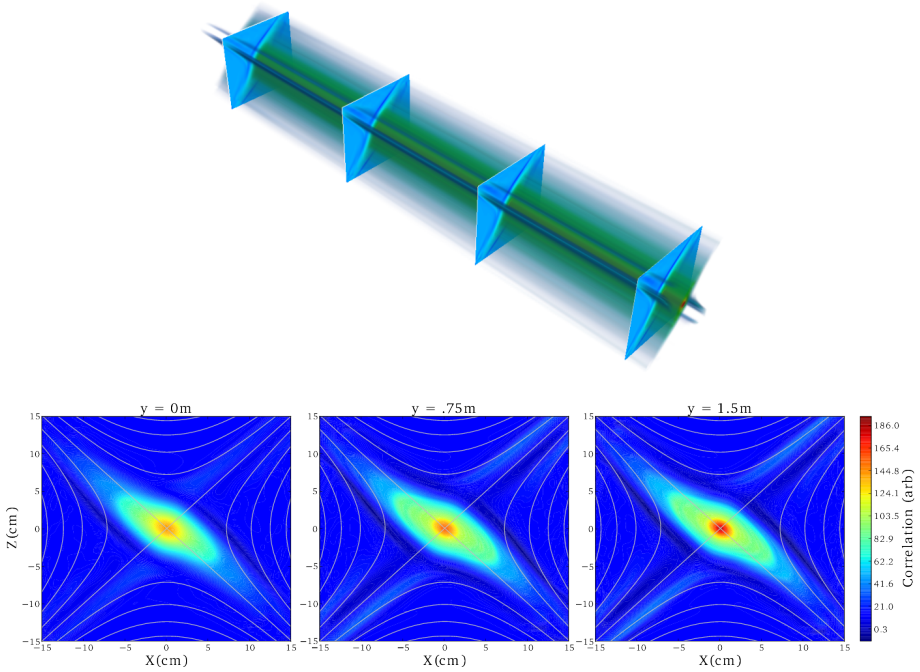

Figure 3.8: Three dimensional cross correlation of an imposed X-point plasma and slices at different longitudinal positions, indicating transport along the field lines and a perturbed profile.

of densities at every point within the domain with that central reference position. From Figures 3.7 and 3.8 it is apparent that the imposed X-point field alters the dynamics of the device. Nevertheless, there exists a correlation among perturbations along the length of the device in both configurations.

As a further analysis, the effect of the imposed X-point on the system's turbulence can be examined using basic synthetic diagnostics. Specifically, one can look at the turbulence on a circle at a constant radius from the center of the plasma column, in this case considered to be $r = 5$cm, and measure the phase shift between potential and density fluctuations. Figures 3.9 and 3.10 indicate this relationship measured on turbulence with longitudinal fluctuations (driftwave-like), which was chosen due to its ubiquitous nature [102, 107]. Here, m is the azimuthal mode number, since this analysis only considers fluctuations in the azimuthal plane.

The phase shift measurements shown in Figure 3.9 indicate structures which are highly correlated and therefore their phase shifts are centered around 0. Figure 3.10 however indicates that the introduction of an X-point causes structures

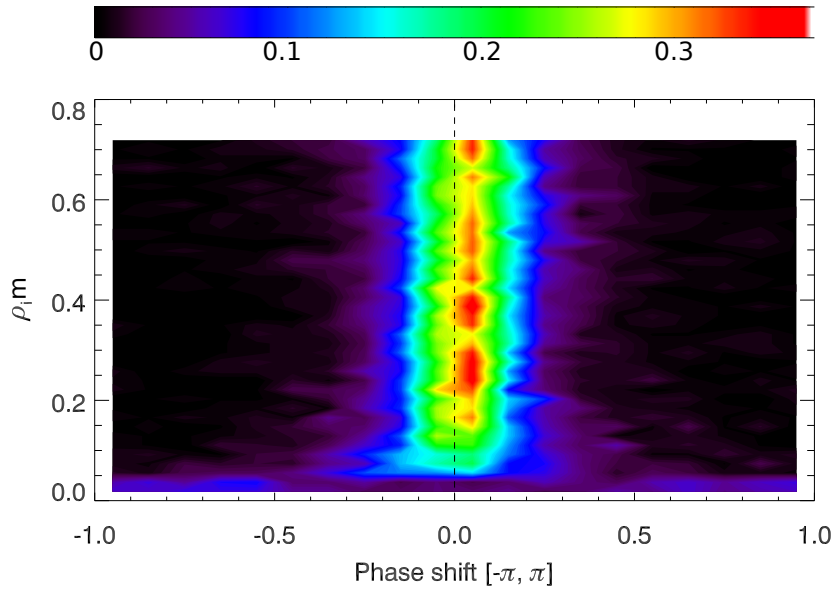

Figure 3.9: Phase shift comparison of density and potential perturbations in driftwave-like modes in a basic linear geometry.

to be dissipated, meaning that their phase shifts, while centered around zero, have a broader, less coherent spectrum. This is to be expected, as the perpendicular, perturbed X-point field lines inhibit the transport of turbulent structures, and therefore dissipates adjacent fluctuations.

Additionally, a similar synthetic diagnostic can be used to examine the cross correlation between perturbations in density and potential within the system, which is a common method in determining the turbulent characteristics of a system [108]. The results of this analysis are shown in Figures 3.12 and 3.13.

Figure 3.12 demonstrates the strong driftwave-like behavior in the simple linear configuration, as the perturbations are highly correlated (as indicated by the contour lying on the 1:1 diagonal). It can be seen from Figure 3.13 that this strongly coherent driftwave like nature is removed when an X-point is introduced, as the coherent modes previously present have been dissociated due to inhibited transport across field lines. These figures and the phase shift measurements shown above provide predictive measurements which could be reproduced in experiment using simple diagnostics.

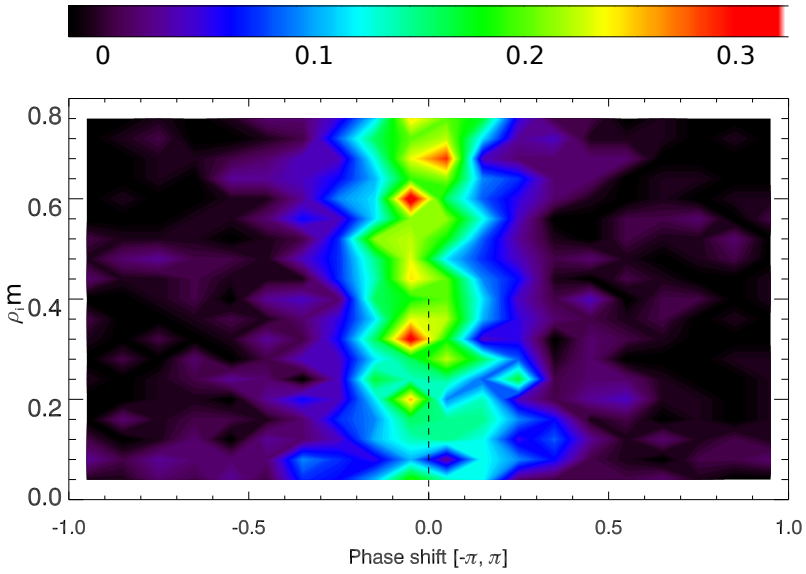

Figure 3.10: Phase shift comparison of density and potential perturbations in driftwave-like modes with an applied X-point.

3.3.3 Energy dynamics

An important aspect of plasma models is conservation of physical quantities. For this reason, an analysis of the energy dynamics within the system was performed similar to that found in reference [109]. In this work, the system is spectrally-decomposed in the azimuthal and axial directions, and the energy of each mode is analyzed to determine the energy transfer channels and dissipation. The energy of each Fourier mode where $\vec{k} = (m, n)$, with m being the poloidal mode number and n the axial mode number, is:

$$E_{tot}(\vec{k}) = \frac{1}{2}\left\langle \underbrace{\left|N_{\vec{k}}\right|^2}_{\text{(a)}} + \underbrace{\frac{1}{2}\left|u_{\parallel,\vec{k}}\right|^2}_{\text{(b)}} + \underbrace{\rho_s^2 \frac{1}{2}\left[\left|\frac{\partial \phi_{\vec{k}}}{\partial r}\right|^2 + \frac{m^2}{r^2}\left|\phi_{\vec{k}}\right|^2\right]}_{\text{(c)}} \right\rangle \tag{3.8}$$

Where N_k, $u_{\parallel,\vec{k}}$ and $\phi_{\vec{k}}$ are the Fourier-transformed density, parallel velocity, and potential, respectively. The analysis presented here occurs in the turbulent, steady state phase described in Figure 3.2. The individual terms in Equation 3.8

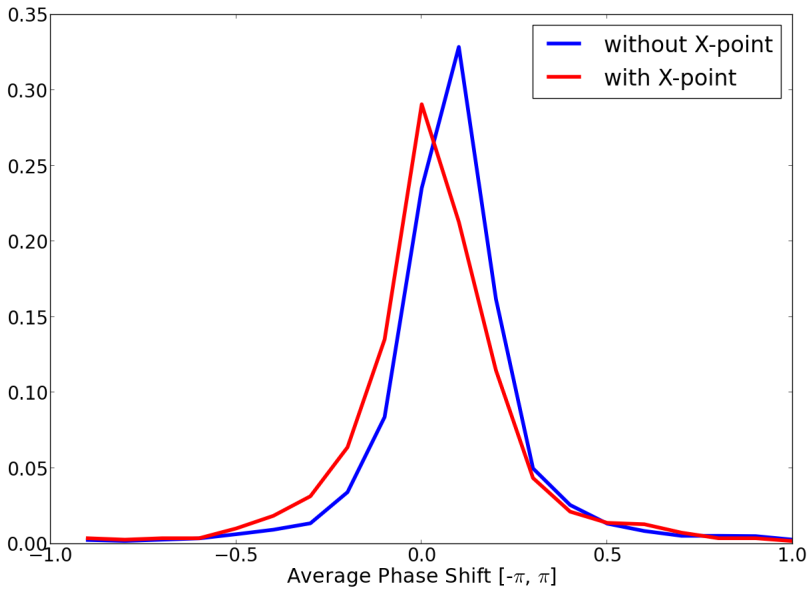

Figure 3.11: Phase shift profiles of azimuthal perturbations averaged over $\rho_i m$.

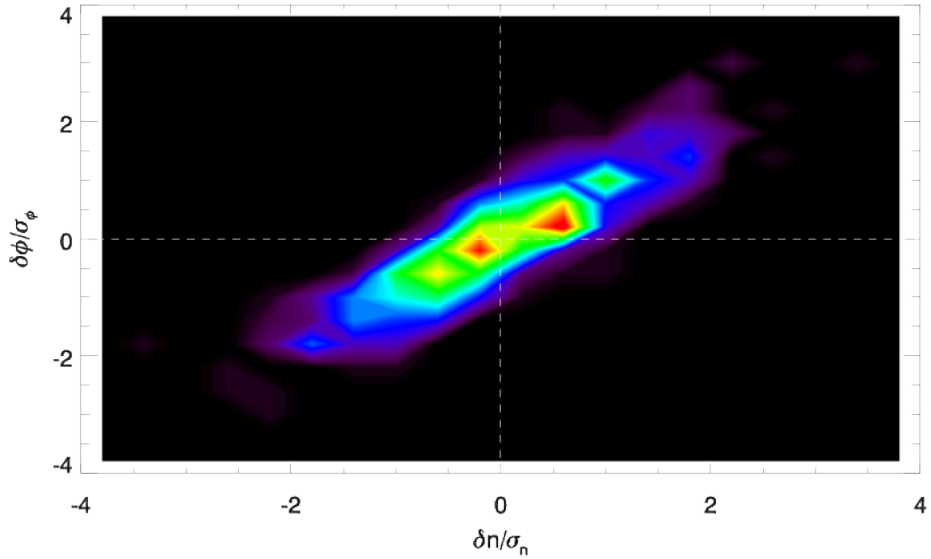

Figure 3.12: Turbulent correlations of density and potential perturbations in driftwave-like modes in a basic linear geometry.

indicate the (a) internal energy, (b) parallel kinetic energy, and (c) perpendicular kinetic energy of the system in Fourier space. The evolution of each Fourier mode

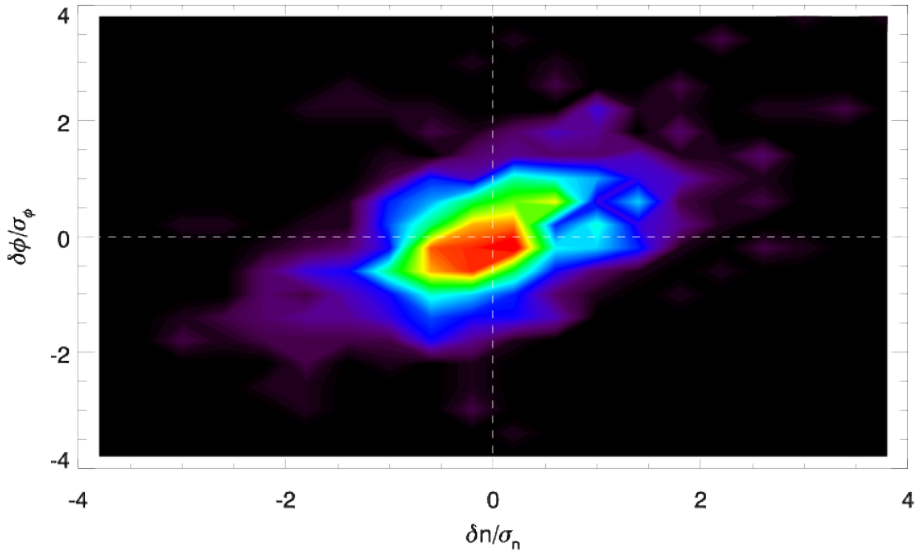

Figure 3.13: Turbulent correlations of density and potential perturbations in driftwave-like modes with an applied X-point.

can be described as [109]:

$$\frac{\partial E_f(\vec{k})}{\partial t} = Q_f(\vec{k}) + C_f(\vec{k}) + D_f(\vec{k}) \tag{3.9}$$

Here, f indicates each field $(N, u_\parallel, \phi, j_\parallel)$, and $Q_f(\vec{k})$, $C_f(\vec{k})$, and $D_f(\vec{k})$ stand for the nonconservative energy forces (i.e. external sources and sinks), linear energy transfer channels, and dissipation terms respectively. There are only conservative energy forces in our system, so $Q_f(\vec{k}) = 0$. The exact expressions for $C_f(\vec{k})$ and $D_f(\vec{k})$ in our model are:

$$C_N(\vec{k}) = \frac{1}{eN_0^2} Re \left\langle ik_\parallel j_{\parallel,\vec{k}} N^*_{\vec{k}} - \frac{1}{N_0} ik_\parallel u_{\parallel,\vec{k}} N^*_{\vec{k}} \right\rangle \tag{3.10}$$

$$C_\phi(\vec{k}) = \frac{1}{eN_0^2} Re \left\langle ik_\parallel j_{\parallel,\vec{k}} \phi^*_{\vec{k}} \right\rangle \tag{3.11}$$

$$C_{u_\parallel}(\vec{k}) = \frac{1}{N_0} Re \left\langle ik_\parallel N_{\vec{k}} u^*_{\parallel,\vec{k}} \right\rangle \tag{3.12}$$

$$C_{j_\parallel}(\vec{k}) = \frac{1}{eN_0^2} Re \left\langle ik_\parallel N_{\vec{k}} j^*_{\parallel,\vec{k}} - iN_0 k_\parallel \phi_{\vec{k}} j^*_{\parallel,\vec{k}} \right\rangle \tag{3.13}$$

$$D_{j_\parallel}(\vec{k}) = Re \left\langle \frac{-j_\parallel^2}{\sigma_\parallel T_{e0}} \right\rangle \tag{3.14}$$

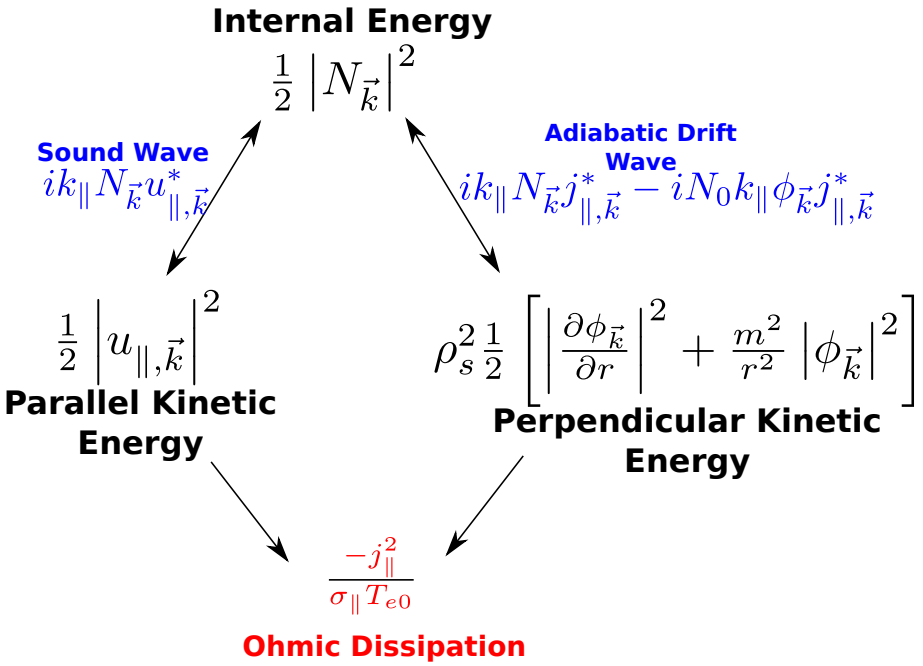

Figure 3.14: Energy dynamics diagram indicating the transfer of energy via sound waves and adiabatic drift waves.

Furthermore, our system conserves energy except for Ohmic dissipation, $\sum_f C_f(\vec{k}) = 0$, as shown in Figure 3.14. As a result, Equation 3.9 elucidates the wave numbers at which energy is dissipated from the system, as the only terms remaining are those found in $D_f(\vec{k})$. Figures 3.15 and 3.16 plot the nonconservative rate of change of the total energy, $\frac{\partial E_f(\vec{k})}{\partial t}$, as a function of wave number in

cases with and without an X-point.

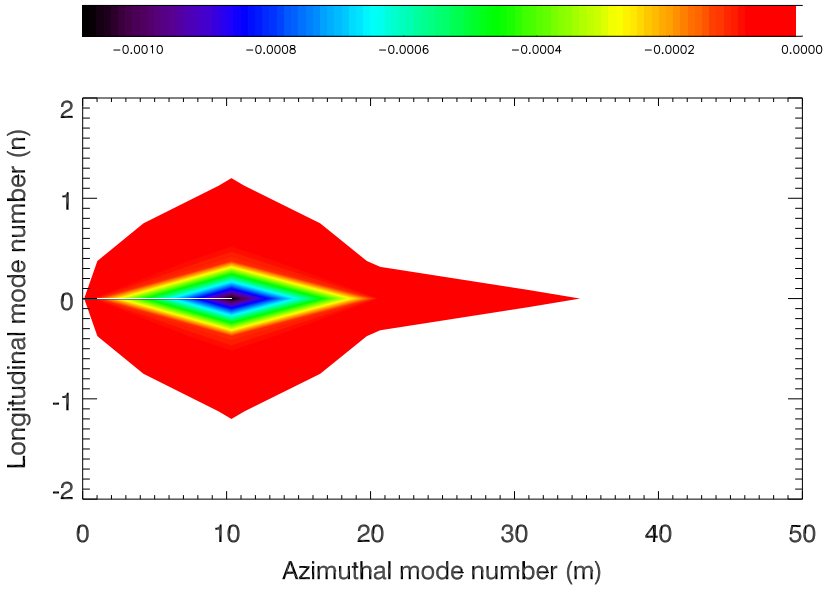

Figure 3.15: Total spectral nonconservative energy loss without an X-point

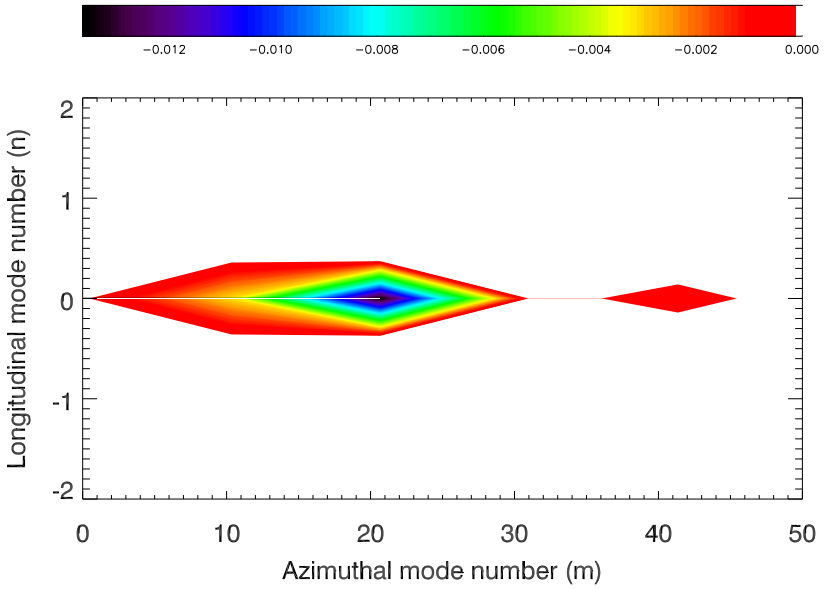

Figure 3.16: Total spectral nonconservative energy loss with an X-point

These results are similar to those found in [109] in that the energy dynamics

(in this case dissipation) is localized to small longitudinal mode numbers. Here, the longitudinal mode number n is normalized such that $n = 1 = 2 * \pi / L$ where L is the length of the device. Therefore, mode numbers smaller than unity are for modes which have a wavelength longer than the device. It should be noted that the nonconservative rate of change of our total energy is negative, as the only contribution is from the Ohmic dissipation, $D_{j_\parallel}$. Furthermore, and somewhat unexpectedly, an X-point reduces the dissipation in higher n-numbers, indicating that the azimuthally-applied X-point perturbs the strictly parallel mode number dissipation. This could perhaps be explained by considering the distortion of the profiles as shown in Figure 3.4, which might dissipate a structure which (without perturbation) would exist helically along the magnetic axis. The shift to higher azimuthal mode numbers is due to the externally applied X-point field inhibiting transport of azimuthally flowing perturbations, which dissolves coherent structures leading to higher mode number oscillations. This indicates that structures in a region of high cross field transport will be small relative to those in regions of free transport. While this is not directly applicable to tokamaks due to the flows of the scrape off layer, it still serves as an interesting result in this configuration.

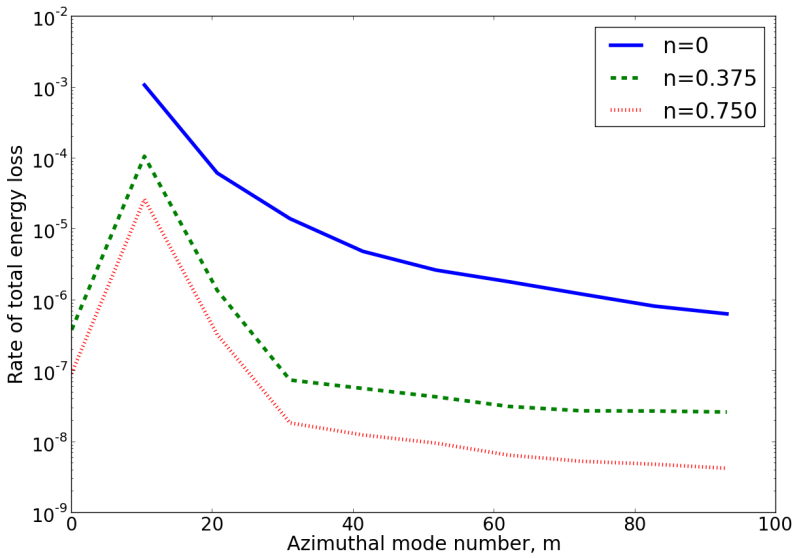

Figure 3.17: Specific longitudinal mode number traces of the total spectral nonconservative energy loss without an X-point

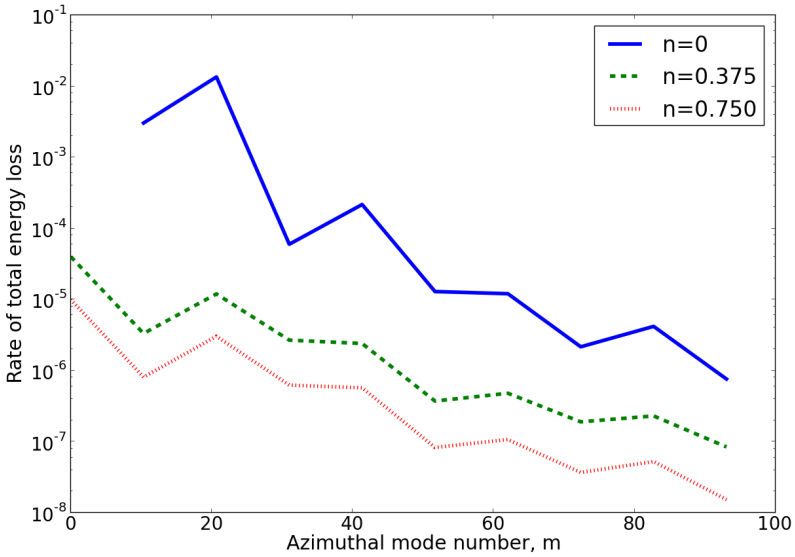

Figure 3.18: Specific longitudinal mode number traces of the total spectral nonconservative energy loss with an X-point

Figures 3.17 and 3.18 show the nonconservative rate of change of the total energy at selected longitudinal mode numbers as a function of azimuthal mode number. It is clear from these plots that the n=0 mode is dominant across the azimuthal mode number spectrum both with and without an X-point. While the introduction of an X-point induces a shift of dissipation to lower n-numbers, Figures 3.17 and 3.18 indicate that dissipation increases for each of those lower-n modes.

3.4 Conclusions and future work

A linear plasma device capable of simulating scenarios relevant to tokamak divertor regions would allow for direct comparison of plasma turbulence models and investigation of fundamental plasma physics. The results presented here indicate that a modest coil set on a university scale linear plasma device will produce measurable effects on the plasma profile, which would help elucidate the physics associated with tokamak divertor regions.

`BOUT++` can capably handle direct X-point simulations by imposing a simple

Cartesian coordinate system and altering parallel operators to include perturbed external fields. The introduction of a modest magnetic X-point perturbs the turbulence characteristics of the plasma column and alters the energy dynamics within the system. The simulations presented here propose future measurements to distinguish an altered driftwave phase shift, perturbed cross correlation in the turbulent spectrum, and measure a perturbed density profile exhibiting transport along the X-point field lines. These measurements could be reproduced experimentally in a similar device, as the variation in cases with and without an X-point is substantial. For instance, the energy dynamics shift to poloidal mode numbers which are twice as high in cases with an X-point. Furthermore, turbulent cross correlation profiles are about twice as wide as in cases without an X-point. It would therefore be interesting to build such a machine which would be able to attain results relevant to tokamak divertor and detachment scenarios.

Future work could look to implement a more complicated model which would remove the isothermal assumption allowing for studies of heat and energy convection. This would help elucidate physics relevant to novel divertor configurations such as the snowflake. Additionally, the results presented here could be compared with those obtained using the Flux Coordinate Independent (FCI) method for parallel derivatives, which will be explained and utilized in Chapter 5. This would help quantify the errors associated with each method, whether it be the assumption of straight field lines (used here) or the interpolation scheme used by the FCI method.

Chapter 4

TORPEX validation

4.1 Introduction

The natural progression after simulating linear geometries is to bend the linear device into a torus. This chapter details the research performed in simulating filament dynamics (Section 2.3.1) in toroidal geometries, specifically the poloidal magnetic null point scenarios in the TORPEX device [110]. Due to the flexibility of the method for creating magnetic geometries in Cartesian `BOUT++` scenarios (Section 2.5.2), we are able to fully reproduce the complex geometries of this experiment. This is the first time that this geometry has been simulated. Experimental measurements of filament propagation are reproduced, but an alternative mechanism for filament acceleration is proposed: it was recently suggested that the filament acceleration is caused by an increasing connection length in the poloidal magnetic null regions [111]. It is determined here, however, that the acceleration seen in experiment is likely dominated by the advection of a developing dipole, which is not unique to X-point scenarios.

Section 4.2 provides a brief introduction and motivation for the studies, as well as a description of the TORPEX poloidal magnetic null point geometry. Section 4.3 describes the modifications of the previously used isothermal model and the implementation of various numerical methods. Section 4.4 discusses filament characterization within this magnetic geometry, before comparing simulation to analytic calculations and experimental measurements in both a stationary and

moving plasma background. Section 4.5 describes the main conclusions of this work and potential areas for further investigation.

4.2 Background

Filaments, or blobs, are typically field aligned plasma structures which have been observed in the scrape of layer (SOL) of many magnetically confined plasmas [63]. These filaments carry particles into the SOL and therefore play a role in determining the profiles during L-mode and inter-ELM H-mode scenarios. While there have been many investigations into the dynamics of such filaments [63, 84, 112], few if any have studied their behavior near magnetic X-points. Simple magnetic tori such as the TORPEX device [113] replicate tokamak scrape off layer (SOL) scenarios while allowing straightforward diagnostic access. While filaments have been studied extensively within TORPEX [110, 114, 115], no theoretical studies have yet explored the dynamics in X-point configurations recently studied experimentally [116, 117, 111].

The fundamental physics of blob propagation is described in detail in Section 2.3.1 and in Reference [63] which is as follows. The divergence of the diamagnetic drift (physically, the curvature drift) causes a polarization of the blob, leading to an $\mathbf{E} \times \mathbf{B}$ velocity in the form of counter-rotating vortices and an outward advection of the blob. The dynamics of propagating filaments depends on the mechanism for charge dissipation within the blob in order to satisfy quasineutrality, $\nabla \cdot \mathbf{j} = 0$. If the charge separation is resolved primarily via the parallel current through the sheath, the filament is considered to be sheath-connected [63, 74]. If the connection length to the sheath is too large, or likewise the resistivity too high, charge is dissipated via cross-field currents such as the polarization current and the blob is said to be in the inertially limited regime [77].

In this work filaments are characterized in TORPEX magnetic null point scenarios using three dimensional simulations in `BOUT++` [101]. The research presented here focuses on the behavior of filaments as they encounter both open and closed field lines, and how that simulated behavior relates to experimentally ob-

served characteristics. Recent work [111] has sought to experimentally characterize filaments in TORPEX magnetic null configurations. A significant acceleration of filaments towards the X-point is observed in [111], and an analytical model is developed to explain this acceleration. In the region of poloidal magnetic nulls, the distance along the field lines between the two lobes of the potential dipole, called the connection length $L_{\parallel}$, is increased. This increased connection length is considered to reduce the effect of charge dissipation via parallel currents, and therefore an acceleration is manifested. Interestingly, a deceleration of the filaments is seen experimentally in the immediate vicinity of the X-point, but this is attributed to dissolution of the blob structure. Here we simulate filaments in these scenarios and compare simulations with this previously derived analytical model [111] in an attempt to further understand the nature of filament propagation in regions of poloidal magnetic nulls.

4.2.1 TORPEX null point scenarios

The aim of this work is to explore blob dynamics in the TORPEX simple magnetic torus in X-point geometries [111, 116, 117]. Many previous studies of filaments in the TORPEX device [73, 118, 119] utilized a case with a vertical field, which is the conventional TORPEX configuration. Figure 4.1 provide a picture of the TORPEX device, with a section of the device removed [113].

The TORPEX device has a major radius of 1m, a minor radius of 20cm, and creates a toroidal magnetic field via the brown coils pictured in Figure 4.1 [113]. The beige coils create a vertical magnetic field, providing open field line configurations similar to the scrape off layer of a tokamak.

Figure 4.2 indicates the trajectory of filaments in three different magnetic fields; a purely toroidal field (top), a TORPEX vertical field scenario (middle), and the recently studied poloidal magnetic null scenario (bottom). This figure helps to illustrate the effects of geometry on the evolution of filaments, as the trajectory of filaments in TORPEX X-point scenarios will later be compared to that in vertical field scenarios.

For the vertical and magnetic null scenarios, the magnetic field is calcu-

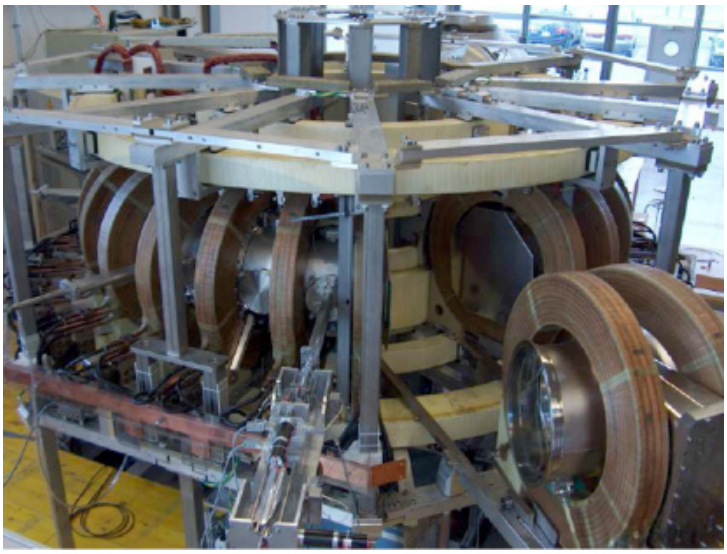

Figure 4.1: The TORPEX device, with a section removed. The brown coils create a toroidal field while the beige coils provide a vertical field in conventional operating scenarios [113].

lated based on the coil position and current, as described in Section 2.5.2 and will be discussed further in section 4.3.2. Filaments in this geometry have been observed experimentally to be toroidally symmetric, and therefore not aligned to the magnetic field [111]. The filaments are first considered coherent in experiment 4cm left of the center of the vacuum vessel (r,z) = (-4cm ,0cm) [117, 111], where (r,z) = (0,0) is considered the center of the vacuum vessel. Here we seed toroidally symmetric filaments with an initial peak density of $3 \times 10^{16}\mathrm{m}^{-3}$ at (r,z) = (-4cm,0cm) and an initial diameter of about 3cm.

4.3 Numerical methods and model

4.3.1 Isothermal Model

The model described previously in Section 2.5.1 is used here to simulate filaments in TORPEX magnetic null point scenarios. This model is again suitable as it was initially constructed for blob studies [84, 120] but has been extended for use in X-point scenarios [1]. Here, the model is extended to include a masking function χ which will be required for dealing with the in-vessel coil in TORPEX. For

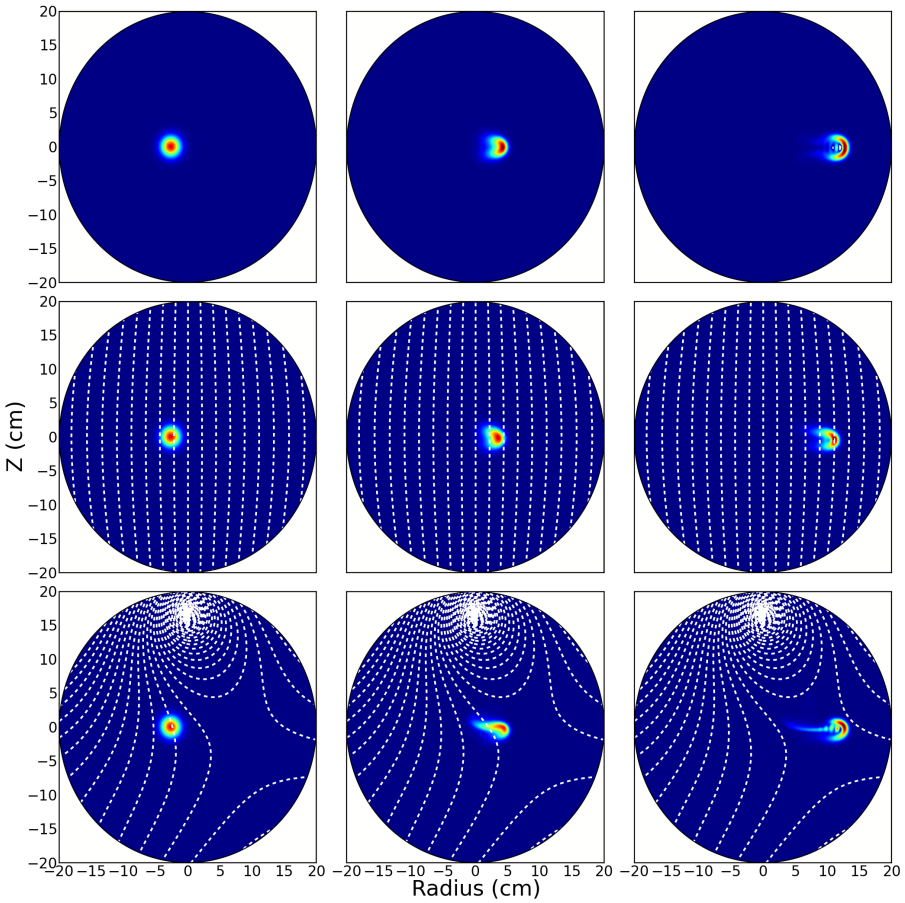

Figure 4.2: Filaments upon initialization (left), $21\mu s$ after seeding (middle), and $42\mu s$ after seeding (right) in three different TORPEX magnetic geometries; (top) purely toroidal magnetic fields, (middle) a vertical poloidal field, and (bottom) a poloidal magnetic null scenario [111]. Poloidal magnetic geometries are indicated by the white, dashed contours.

these simulations, the isothermal electron temperature T_{e0} is set to 2.5eV, as is measured in experiment [117]. The equations are given again as follows in SI units:

$$\frac{dn}{dt} = (1-\chi)\left[2c_s\rho_s\xi\cdot(\nabla n - n_0\nabla\phi) + \nabla_\parallel\frac{J_\parallel}{e} - n_0\nabla_\parallel u_\parallel\right] + \chi\nabla_\parallel^2 n \tag{4.1}$$

$$\rho_s^2 n_0\frac{d\omega}{dt} = 2c_s\rho_s\xi\cdot\nabla n + \nabla_\parallel\frac{J_\parallel}{e} \tag{4.2}$$

$$\frac{du_{\parallel}}{dt} = -\frac{c_s^2}{n_0}\nabla_{\parallel} n \tag{4.3}$$

$$J_{\parallel} = (1-\chi)\left[\frac{\sigma_{\parallel} T_e}{e n_0}(\nabla_{\parallel} n - n_0 \nabla_{\parallel}\phi)\right] \tag{4.4}$$

Where $\omega \equiv \nabla_{\perp}^2 \phi$ is the vorticity, total derivatives are split via $\frac{d}{dt} = \frac{\partial}{\partial t} + \mathbf{u_E}\cdot \nabla + \mathbf{u}_{\parallel}\cdot\nabla$, and parallel derivatives are evaluated using $\nabla_{\parallel} = \mathbf{b}\cdot\nabla$ where $\mathbf{b}$ is the unit vector along the total magnetic field, including the poloidal field. Curvature effects are included via the polarization vector $\xi \equiv \nabla \times \frac{\mathbf{b}}{B} \sim \frac{1}{BR_c}\hat{\mathbf{z}}$. In the above equations, $\rho_s = \frac{c_s}{\Omega_i}$ is the Bohm gyroradius, and $\sigma_{\parallel}$ is the parallel (Spitzer [121]) conductivity. These equations are normalized such that density (n) is normalized to typical TORPEX values, $n_0 = 8\times 10^{15} m^{-3}$, speeds are normalized to the sound speed, and $\phi = \frac{e\Phi}{T_{e0}}$ is the normalized electrostatic plasma potential.

The fundamental physics of blob propagation is reliant upon the currents within the system, as discussed in Section 2.3.1. This model effectively incorporates both the diamagnetic and polarization currents; the left hand side of the vorticity equation is the polarization current density, and the first term on the right hand side describes the diamagnetic current density.

Because TORPEX utilizes an in-vessel coil to create the X-point field, the singularity on the coil axis has been avoided by implementing a penalization scheme [104, 122], which utilizes a masking function at the location of the wire such that there are no gradients across the coil cross section. The masking function (χ) has the following form:

$$\chi = \begin{cases} 1 & 0 < r < r_c \\ \chi_0\ ln(r) & r_c \le r \le 1.1 r_c \\ 0 & r > 1.1 r_c \end{cases}$$

Where r_c is the coil radius, chosen here to be 1cm, and χ_0 is an arbitrary coefficient to determine the smoothness of the masking function. The final term of Equation 4.1 is a simple diffusion term to allow density to diffuse across the coil cross section.

4.3.2 Numerical Methods

The presence of poloidal magnetic field singularities in the form of O- and X-points in this magnetic topology requires the use of non-field-aligned coordinate systems. As such, a cylindrical coordinate system defined by the major radius ($\mathbf{x}$), vertical direction ($\mathbf{z}$), and toroidal direction ($\mathbf{y}$) was implemented , and the poloidal magnetic field was again implemented by prescribing an analytic form for the magnetic vector potential and modifying the parallel gradient operator.

The model described in Section 4.3.1 is solved in this geometry using a resolution of 1.5mm ($0.36\rho_s$) in the poloidal plane ($\mathbf{x}$, $\mathbf{z}$), and 15.7cm ($36.5\rho_s$) in the toroidal direction ($\mathbf{y}$). This resolution was chosen as modes are considered to be flute-like such that fluctuations are large scale in the toroidal direction and small in the poloidal direction. The perpendicular resolution is sufficient since it smaller than a gyroradius; fluid approximations assume that fluctuations vary slowly over a gyroradius. The remaining numerical schemes were used as in Chapter 3: time integration was implemented using the implicit time integration solver CVODE, within the SUite of Nonlinear and DIfferential/ALgebraic equation Solvers (SUNDIALS) [94]. The Laplacian solver, which calculates potential (ϕ) from vorticity (ω), in `BOUT++` was altered to invert using discrete sine transforms in the $\mathbf{z}$ (vertical) direction, which eliminates the periodicity used in typical Laplacian inversion utilizing Fourier transforms in `BOUT++` [101]. As the filaments in TORPEX are considered toroidally symmetric and therefore do not reach the sheath, simple Neumann (zero gradient) boundary conditions have been used in the poloidal plane, although presheath boundary conditions [106] have been implemented.

4.4 Filament Characterization and Experimental Comparison

As the model described in section 4.3.1 was previously tested in linear geometries [1], simulations were performed here to validate the extension of this model to toroidal geometries and to determine the characteristics of blob propagation within the TORPEX magnetic null point scenarios. Experimental comparison was conducted to investigate the filament acceleration mechanism seen in experiment. The simulations were initialized based on experimental observations [111, 123]; the initial filament diameter, measured as the full width at half maximum, was set to 3cm, and the filaments were seeded at (r,z) = (-4cm,0cm) as this is where filaments are first considered coherent in this TORPEX geometry. It has been proposed in [111] that the poloidal magnetic null region causes an acceleration by increasing the connection length associated with the dipole field. Here we test this assertion and compare simulations to the previously developed analytical model.

4.4.1 Current characterization

As described in Section 2.3.1, currents within filaments determine their propagation. Typically, filaments are field aligned and therefore can extend to the sheath, although recent work has found that currents can extend to the sheath even if the filament itself does not reach the target [118]. Filaments within this TORPEX configuration have been determined to be toroidally symmetric, however, and therefore the current is expected to be localized within the blob. As such, we have investigated the currents within the simulated filaments, as shown in Figure 4.3.

From Figure 4.3 it is apparent that the current is localized to the blob and does not extend to the plasma sheath at the edges of the computational domain. This localized current is essential to the development of the model in [111], as it is assumed that the charge is dissipated along the field line which connects the two lobes of the potential dipole. Furthermore, Figure 4.3 indicates our current

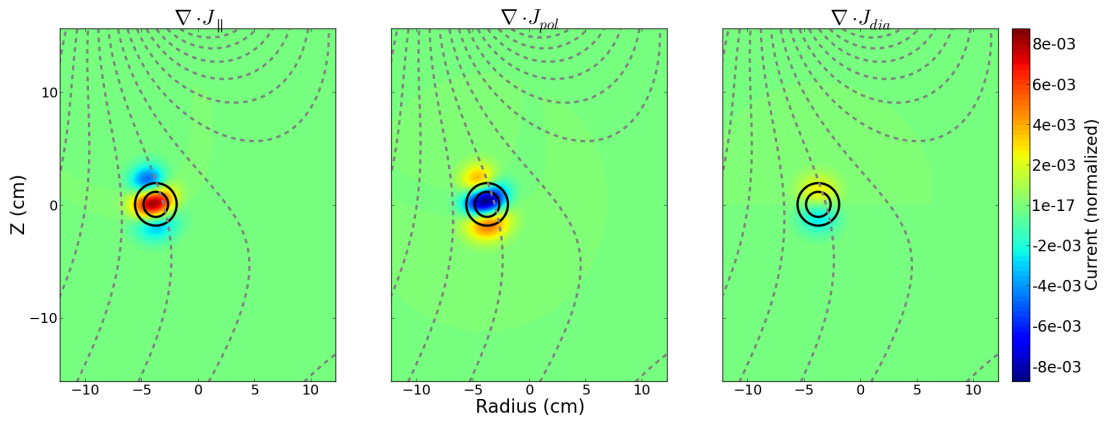

Figure 4.3: The divergence of the three currents within the system (color contour) immediately after initialization. The blob cross section is shown as the black solid contours, and the poloidal magnetic field is indicated by the grey dashed contours.

balance, since $\nabla \cdot J_{pol} \approx \nabla \cdot J_{dia} + \nabla \cdot J_{\parallel}$, and therefore the total current is divergence free.

4.4.2 Stationary Background

Having explored the currents which govern the filament propagation in this geometry, an attempt to validate simulation methods with experimental measurements of blob velocity was conducted. Initial simulations were performed with a stationary background plasma profile. To compare with experiment, the center of mass velocity was calculated and plotted for comparison with experimental data [111]. The results of this analysis are summarized in Figure 4.4, where the simulation in a stationary background is plotted as a solid green line.

From this data, it is clear that although the simulations exhibit a similar velocity to the blob propagation in experiment, they do not exhibit the same acceleration; the acceleration found in experiment is much higher than that of the simulations in the region of the X-point. However, it is still possible to determine the effect of the magnetic null region on filament propagation by seeding blobs at various distances from the magnetic null and measuring their velocities as they approach the X-point. The results of these simulations are shown in Figure 4.5.

Figure 4.5 indicates that the filaments undergo an acceleration as they ap-

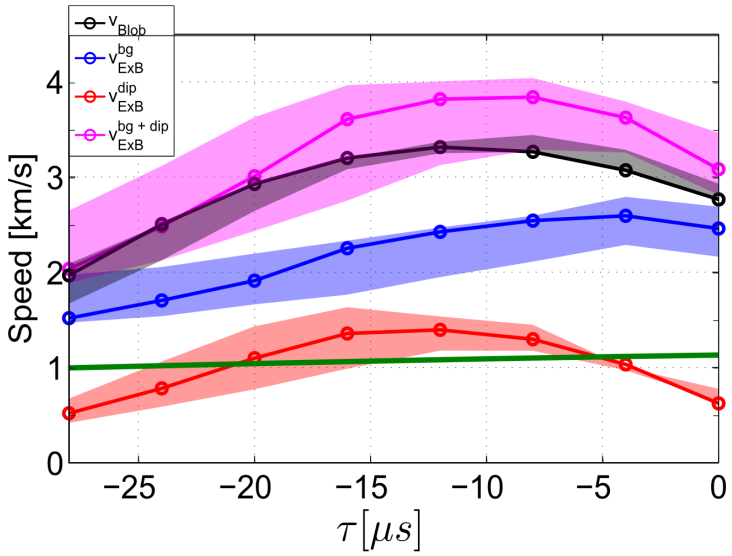

Figure 4.4: Center of mass velocity measurements from experiment (red, blue, black, magenta) and simulation (green). The black curve indicates the measured blob speed from experiment. The blue curve represents the calculated $\mathbf{E} \times \mathbf{B}$ background plasma velocity from measurements of the plasma potential. The red curve illustrates the calculated $\mathbf{E} \times \mathbf{B}$ from the blob potential dipole measurements, and the magenta curve is the calculated $\mathbf{E} \times \mathbf{B}$ velocity of the blob (red) plus the background velocity (blue). The simulation has a stationary background, and is comparable in magnitude to measurements which neglect the background, reproduced from Reference [111].

proach the X-point, but the highest acceleration occurs at the beginning of the evolution. To further analyze this, the acceleration of the various seeded blobs is illustrated in Figure 4.6.

Filaments have a higher acceleration at the beginning of their evolution due to the developing dipole, and continue to accelerate more slowly as they approach the X-point. This supports the assertion that the magnetic null point region causes an acceleration of filaments, most likely due to the increased connection length. However, as the strongest acceleration occurs during the formation of the dipole (e.g. $\sim 1 \times 10^8 \mathrm{ms}^{-2}$ for the case seeded at x_0 = -4cm), these results could indicate that the acceleration seen in experiment is due to the dipole forming on a moving background (which is itself approaching the null region). Furthermore, this initial acceleration is the same for each case, indicating that it is geometry independent. This is illustrated well in Figure 4.7, which plots the center of mass

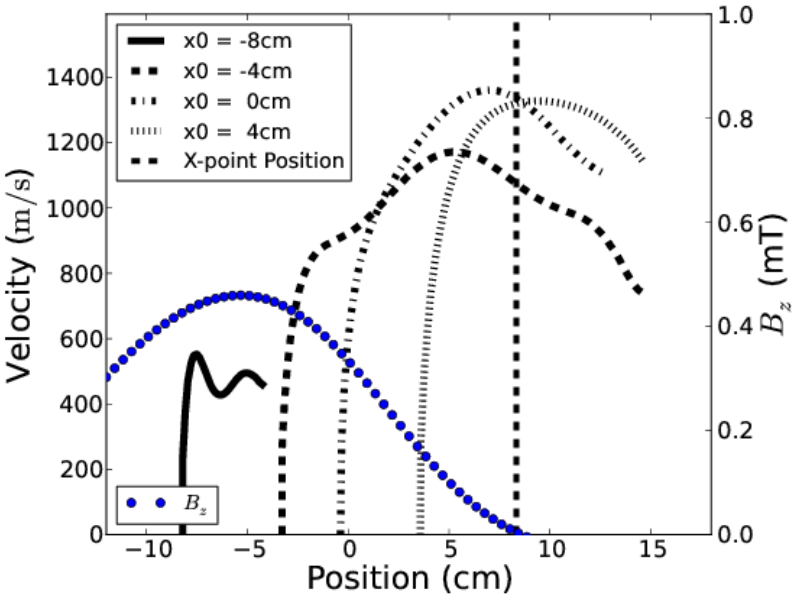

Figure 4.5: Velocity comparison of blobs seeded at various distances from the X-point. Faster blob propagation is seen near the null region, which is marked with a vertical line. The vertical field strength is plotted in blue dots as an indication of connection length, as $L_{\|} \sim B_z^{-1}$.

velocity for filaments seeded at different locations as a function of time.

Figures 4.7 and 4.6 indicate that the initial acceleration of the filaments, which is similar to that measured in experiment, is the same regardless of initial seeding position. This suggests that this acceleration is geometry independent, as it is only caused by the initial formation of a dipole. Therefore, the acceleration of an advected dipole could could mimic the acceleration caused by an X-point, and could explain the experimental observations. In these simulations, the dipole develops self-consistently, but there is no initial background potential profile. This could be different in experiment, where a dipole could already be present when a blob forms. The seeding of filaments farther from the X-point, however, would allow a dipole to fully develop before encountering the X-point region. In any case, the hypothesis of an advected developing dipole mimicking X-point acceleration due to increasing connection length will be further tested in Section 4.4.4.

To determine if the effects modelled here are consistent with previous analysis of TORPEX X-point scenarios [117, 111], a comparison with an analytic model [117, 111] of blob propagation in magnetic null regions was performed.

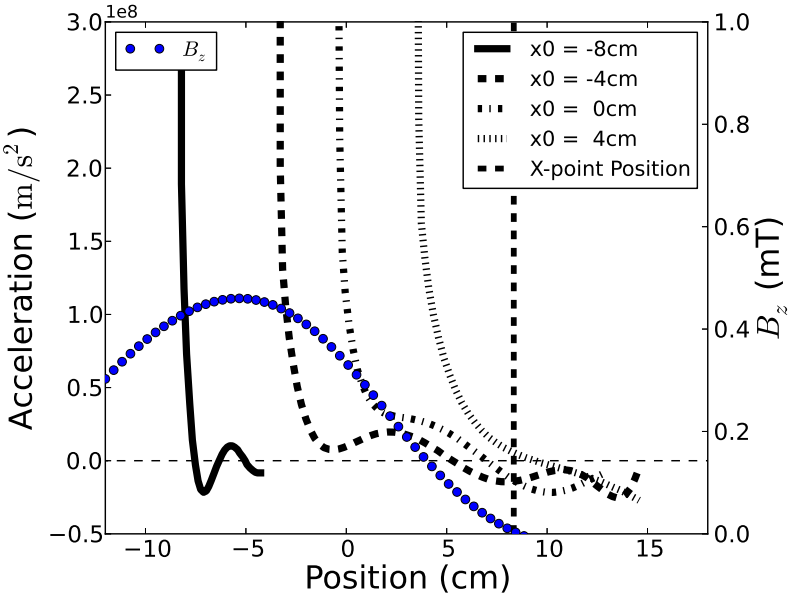

Figure 4.6: Comparison of acceleration of blobs seeded at various distances from the X-point. The highest acceleration occurs initially, as a dipole is developing. The vertical field strength is again shown in blue dots as an indication of connection length.

4.4.3 Analytical model comparison

An analytical model has been previously developed which relies on the assumption of increasing connection length in poloidal magnetic null regions as an acceleration mechanism [117, 111], and will be referred to here as the "Avino model". In this model, the blob velocity follows a function as shown in Equation 4.5:

$$v_b = \frac{\delta n}{n}\sqrt{\frac{2a}{R}}c_s\left(\frac{1}{1+A/L_\parallel^2}\right) \tag{4.5}$$

where:

$$A = \frac{CB^2a^{5/2}\sqrt{2R}}{m_i c_s} \tag{4.6}$$

Here, C is the proportionality coefficient between the plasma conductivity and the plasma density ($C = \sigma/n$), a is the radius of the blob, $L_\parallel$ is the parallel connection length, R is the major radius, and c_s is the sound speed. In the limit

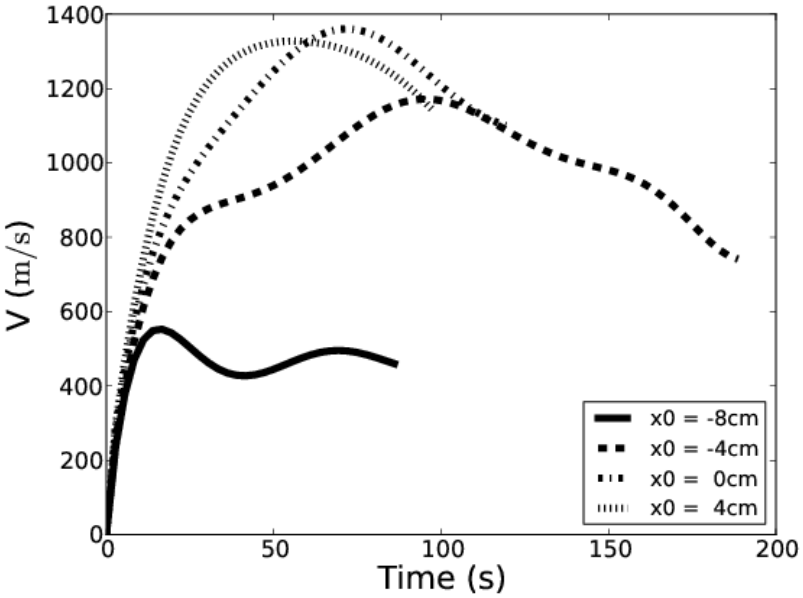

Figure 4.7: Velocity comparison of blobs seeded at various distances from the X-point as a function of time. The initial acceleration is the same in every case, which can be attributed to the developing potential dipole; as the dipole develops, the increasing electric field causes an acceleration.

$L_\parallel \to 0$, this relation reduces to the inertial scaling for blobs [63], and a $1/a^2$ scaling can be seen via the a dependence in the expression for A. In the original analysis by Avino et al., the relative perturbation of density, $\delta n/n$, was considered constant, and therefore the magnetic field (B), which also dictates the parallel connection length $L_\parallel$, is considered the only position-dependent variable. In the analysis presented here, however, we are able to directly calculate all quantities in Equation 4.5 from numerical simulations.

Although the plasma (Spitzer) conductivity [124] is an input to the simulation, it is calculated differently in [111], which defines it as:

$$\sigma = \frac{ne^2}{m_e \nu_{eH}} \tag{4.7}$$

where $\nu_{eH} = n_n \sigma_{eH} \sqrt{T_e/m_e}$ is the electron-neutral collision frequency. In these simulations, we have assumed the neutral density n_n is $2 \times 10^{18}\mathrm{m}^{-3}$ and a collisional cross section $\sigma_{eH} = 2 \times 10^{-19}\mathrm{m}^2$ following the analysis of [125]. It

should be noted, however, that this plasma conductivity only affects the value of C, which is used as a free parameter both here and in [111] to ensure that the model correctly corresponds with initial measured/simulated filament velocity. As stated previously, an isothermal temperature of 2.5eV was assumed.

The blob size a can be calculated as half the distance between the maximum and minimum of the potential dipole. Connection length is calculated by assuming that:

$$L_{\parallel} = \frac{2a}{tan\left(\frac{\delta B}{B}\right)} \tag{4.8}$$

where $\delta B/B$ is the poloidal magnetic field over the toroidal magnetic field. In completely vertical field cases, this reduces to B_z/B.

This model was then plotted against the same stationary background simulation which was shown in Figure 4.4 along with the calculations from Reference [111]. The proportionality coefficient C is adjusted such that the calculated blob velocity coincides with our simulation 28μs prior to the filament arriving at the X-point. This is also done in Reference [111], where the proportionality constant is three times that calculated analytically. Here, the proportionality constant is multiplied by a factor of 0.63 ($C = 0.63C_{analytic}$) relative to the analytic solution, whereas C was increased by a factor of 3 in [111]. Figure 4.8 illustrates the simulation, the calculations based on the simulation presented here with an adjustment to the proportionality constant, and the connection length $L_{\parallel}$ which was previously asserted to be the main contribution to filament acceleration.

From Figure 4.8 it is not clear how well the analytical model expressed in Equation 4.5 reproduces the data. While the increasing connection length corresponds to an increased analytical blob velocity, the simulated filament velocity is not fully recovered, even when other factors such as $\delta n/n$ in Equation 4.5 are evolved. As $\delta n/n$ is considered constant in [111], a higher acceleration is seen. Since $\delta n/n$ will only decrease (no sources), when allowed to vary as shown here, the analytic calculation produces a smaller acceleration. While other factor are varying (b, R), they vary by less than $10^{-}3$, and therefore are not as significant as

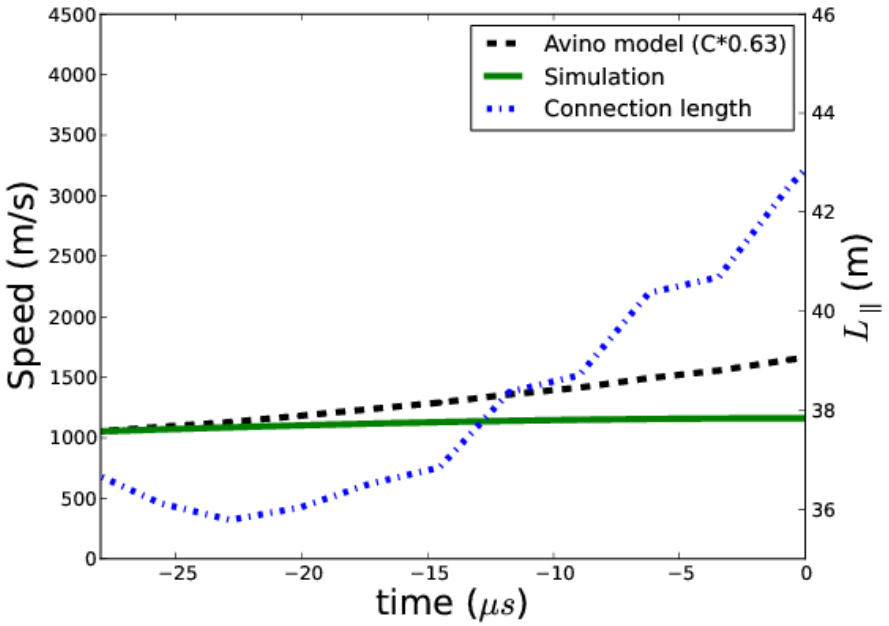

Figure 4.8: Comparison of simulated blob velocities (on a stationary background) with an analytical model [111]. Simulated results are shown in green, the model explicitly calculated herein is shown in black, dashed, with an adjustment to the proportionality coefficient. Here, as with [111], t=0 is when the blob is at the null point. The connection length is shown in blue, dot-dashed.

the density perturbation, which varies by as much as 30%. Furthermore, the parallel connection length is not infinite, as the filament experiences a slight vertical displacement, and misses the exact X-point.

The same analysis was conducted on a filament seeded farther from the magnetic null region. This allows the filament dipole to fully develop before encountering any effects of the X-point. The results are shown in Figure 4.9.

This supports the hypothesis that the increasing connection length $L_\parallel$ in the region of the X-point causes an acceleration, as the model described in Reference [111] reproduces results seen in the simulation. Here, the proportionality coefficient C was decreased by a factor of 3.3 relative to the analytic solution($C = 0.3C_{analytic}$). As the analytical model exhibits the same acceleration profile as shown in simulation, it is plausible to conclude that the acceleration seen in the simulation is due to the introduction of the X-point. This acceleration, however, is smaller than that seen in experiment. The acceleration seen

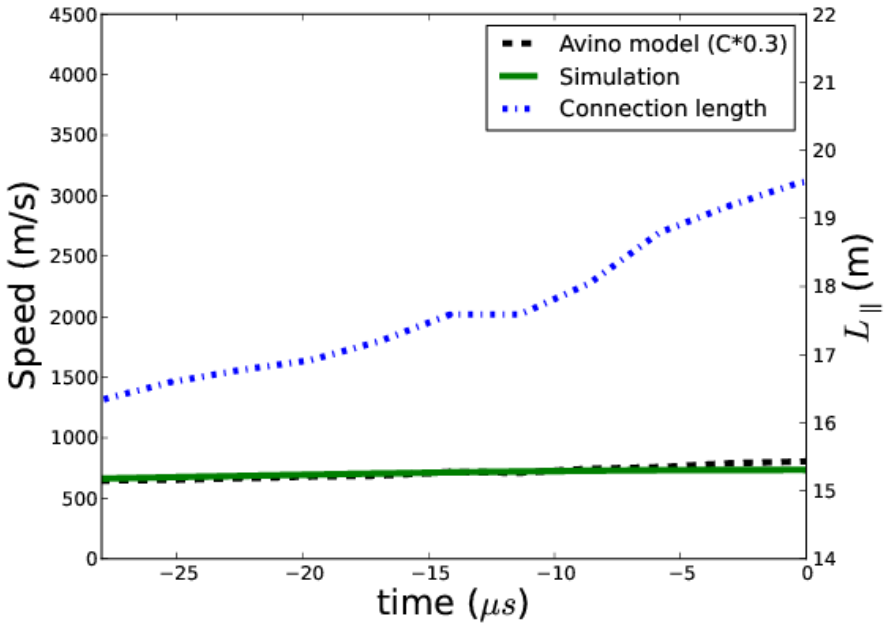

Figure 4.9: Comparison of simulated blob velocities (on a stationary background) with an analytical model [111]. Here, the filaments are seeded farther from the X-point, at r_0 = -8cm to allow the dipole to fully develop. Simulated results are shown in green and the model explicitly calculated herein is shown in black, dashed. The connection length is shown in blue, dot-dashed.

in experiment is characteristic of the initial dipole formation. If the developing dipole were advected toward the X-point, it could appear that the magnetic null region is causing the acceleration, when in actuality the effect of the null region on the acceleration is minimal (as shown here). To test the assertion of an advected dipole creating the acceleration profile seen in experiment, a moving background was added to the simulation, corresponding to a vertical electric field observed in experiments.

4.4.4 Constant translational background

To investigate if the initial dipole development causes the acceleration seen in experiment, a constant background radial plasma velocity of 2km/s was implemented in accordance with experimental measurements [111]. This was incorporated by implementing a background plasma potential profile with a constant gradient in **z**, thereby creating a constant radial $E \times B$ motion of the plasma.

Figure 4.10 shows the results of three simulations. A simulation of blobs on a stationary background plasma profile, as discussed previously, is shown as the solid line. The dashed line indicates the velocity of a blob in a TORPEX X-point geometry with a moving background. When this is compared with the experimental measurements in Reference [111], it is clear that the simulation has more closely reproduced the experimentally observed acceleration and deceleration.

Not only does this case match the velocity seen in experiment, but both the average acceleration and deceleration are reproduced. There is a slight difference in the maximum velocity which could potentially be attributed to the isothermal and inviscid approximations, or the effect of neutral damping.

Figure 4.10 also illustrates the calculated blob velocity using Equation 4.5 and the parameters from the simulation. It is clear that the acceleration profile is not matched by the analytical model when the parameters in Equation 4.5 are explicitly calculated, and the initial acceleration is underestimated, indicating an additional acceleration mechanism to the increasing connection length $L_{\parallel}$.

To verify that this effect is an effect of dipole formation and not the null region increasing connection length, we can overplot the velocity in a vertical magnetic field case, where no magnetic X-point is present. The vertical field case is the typical TORPEX scenario, and has been implemented via Equation 2.67 knowing the vertical coil current and locations [123]. The vertical field is relatively constant and the same strength as the X-point field at the blob seeding/birth location, (r,z)=(-4cm,0cm). The results of this test case are also shown in Figure 4.10, where the dotted line indicates the blob propagation in a vertical field case with a moving background.

Figure 4.10 indicates that filaments in a vertical field have similar acceleration and velocity characteristics to those in magnetic X-point scenarios. To analyze this assertion more completely, the $E \times B$ component of the blob propagation has been calculated from simulation in both X-point and vertical field scenarios. The comparison of these contributions is shown in Figure 4.11.

From Figure 4.11 it is clear that the $E \times B$ motion is the dominant effect in blob velocity. Additionally, Figure 4.11 allows for direct comparison with

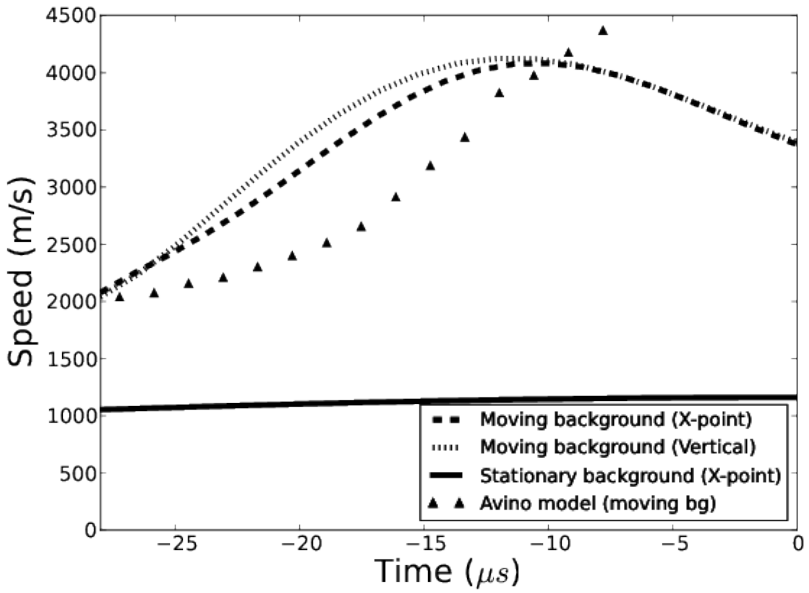

Figure 4.10: Center of mass velocity measurements from simulations of three different scenarios; stationary background X-point case (solid), moving background X-point (dashed) and vertical (dotted) fields. The vertical field case in a moving background recovers the same characteristics as the X-point simulation and experimental measurements, indicating that the null region has little measurable effect on filament acceleration. This assertion is also supported by the small acceleration seen in the stationary background case (solid). The Avino model fails to recover the simulated acceleration, indicating and additional acceleration mechanism.

Figure 4.4. By plotting the $E \times B$ contribution for both cases, it can be illustrated that the X-point has little measurable effect on the filament acceleration via $E \times B$ convection. Additionally, the differences in velocity profiles between vertical and X-point scenarios as seen in simulation lie within the experimental uncertainty [111].

From these results it is possible to conclude that the acceleration mechanism seen in experiment is not primarily due to the increased connection length in the region of the X-point. Instead, the moving background causes the developing dipole to propagate towards the null region as it begins to accelerate the filament relative to the background. It should be noted that the recent experiments in magnetic null point geometries are not the first to exhibit the shown acceleration and deceleration profile. This characteristic has been seen previously in TORPEX

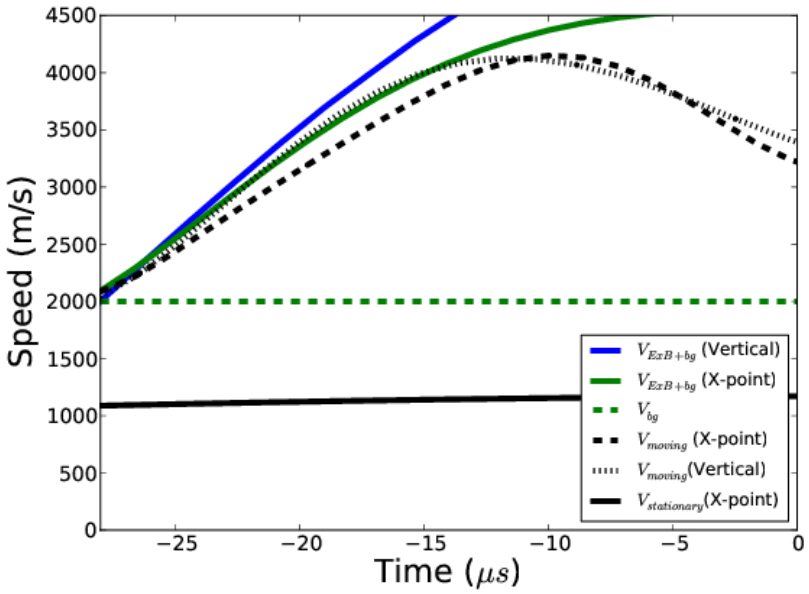

Figure 4.11: Center of mass velocity measurements from simulations including the $E \times B$ contributions for vertical (blue) and X-point (green) scenarios.

without poloidal magnetic nulls both with simulation [119] and experiment [73], both of which exhibit an initial acceleration and deceleration in the first tens of microseconds. Additionally, the analytical model derived in [111] was also unable to explain the deceleration after $t \sim -10\mu s$ in the immediate vicinity of the X-point, which was attributed to the dissolution of the blob (despite $\delta n/n$ being considered almost constant immediately prior). The advection of a developing dipole exhibits both an acceleration and a deceleration of the filaments on a correct timescale. As the analytical model in Figure 4.10 underestimates the acceleration, the increasing connection length can be considered a minor factor in the filament acceleration.

4.5 Conclusions and future work

We have successfully been able to model blob propagation in the X-point scenarios within the TORPEX device using a method of perturbed magnetic vector potentials. By prescribing a Cartesian coordinate system, numerical instabilities have been avoided, allowing for straightforward simulation. Experimental

measurements could be reproduced, however simulation results indicate that the filament acceleration seen in experiment is due to dipole formation, and not the increased connection length caused by to the introduction of an X-point. It has also been shown that the magnetic null region does indeed cause an acceleration of filaments in the vicinity of the X-point. This acceleration, however, is much smaller than that of the initial dipole formation, and therefore is difficult to measure experimentally. However, if the magnetic null were created farther from the region where the filaments are formed, it would in principle be possible to measure the acceleration due to the increased connection length in the X-point region, provided the blob dipoles were given sufficient time to form. Future computational analysis of TORPEX configurations should look to implement a more complicated model which does not make an isothermal approximation and accurately incorporates neutrals.

Chapter 5

Towards nonaxisymmetry

Having modelled complex magnetic geometries in both linear and toroidal configurations, we provide here the basis of ongoing work towards nonaxisymmetric modelling in BOUT++. The ultimate goal of this research is to be able to simulate plasma fluid turbulence simulations in realistic stellarator geometries in BOUT++. This would allow for comparison with experiment as well as divertor interaction studies, which are currently limited computationally to (non-turbulent) transport simulations.

Section 5.1 provides a brief discussion of the current status of stellarator transport modelling, and the associated challenges. Section 5.2 introduces the Flux Coordinate Independent (FCI) method for calculating parallel derivatives, which allows the simulation complex geometries including stellarators. Sections 5.3 and 5.4 describe the testing of the FCI method and describe the foundations for stellarator modelling in BOUT++, including transport modelling using the FCI method. Finally, Section 5.6 provides a summary and description of proposed future work toward global stellarator edge fluid turbulence modelling in BOUT++.

5.1 Stellarator and Nonaxisymmetric Modelling

Historically, neoclassical transport has been the dominant loss mechanism in stellarators [126]. Recent optimizations have allowed for the minimization of neoclas-

sical losses, which has culminated in the design of the Wendelstein 7-X stellarator [39, 127]. As Wendelstein 7-X has been optimized for neoclassical transport, turbulent transport could potentially become comparable to neoclassical losses. As such, it is becoming increasingly important to simulate turbulence in nonaxisymmetric configurations to determine its role in comparison to neoclassical transport in order to optimize performance.

Edge fluid turbulence modelling of tokamak plasmas often exploits the axisymmetry of tokamak configurations to reduce the computational expense. The nonaxisymmetric nature of stellarators, however, requires that simulations are fully three dimensional. For three dimensional tokamak modelling, it is often advantageous to align the computational grid to the magnetic field as discussed in Section 2.4, which helps improve numerical efficiency. Typically, parallel dynamics exhibit a high wavelength, which allows for lower resolution in the parallel direction, and therefore faster computation. In stellarators, however, the complex magnetic geometry requires either a clever field aligned system [128], or a nonaligned system since parallel structures are introduced along the magnetic field.

Figure 5.1 [129] presents a Poincaré plot of the Wendelstein 7-X stellarator, which illustrates the differences between the edge and core of a stellarator which determine the difficulty in simulating edge and core turbulence.

In the core of stellarators, the closed flux surfaces and low collisionality facilitate the use of gyrokinetic codes such as GENE [130], which is currently the only technique for simulating stellarator turbulence. However, due to the small scales simulated in gyrokinetics, the computation is quite expensive for experimentally relevant temporal and spatial scales. Additionally, GENE simulations are currently localized to single flux surfaces or flux-tube geometries.

The edge of stellarators, however, includes stochastic regions and magnetic islands, and edge modelling in stellarators is currently limited to magnetohydrodynamic transport modelling to determine the steady state profiles. This is done primarily using a code called EMC3 [131], which employs a Monte-Carlo solver to simulate three dimensional transport (non-turbulent) equations in or-

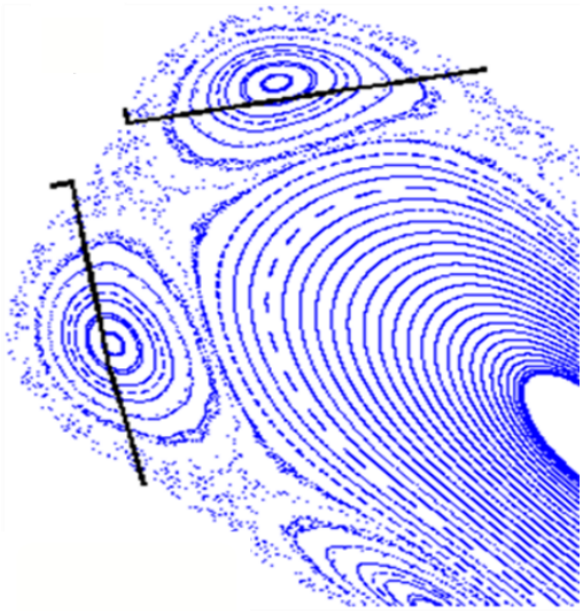

Figure 5.1: Poincaré plot of the Wendelstein 7-X magnetic field lines, indicating closed flux surfaces in the core and a stochastic edge region [129]

der to determine steady state quantities for divertor profiles. The relatively high collisionality of edge plasmas both in stellarators and tokamaks justifies a fluid approach to turbulence simulations, however the current nature of plasma fluid turbulence simulations renders it difficult to simulate nonaxisymmetric magnetic geometries; stochastic regions are impossible in field-aligned coordinate systems.

The simulation of nonaxisymmetric configurations in `BOUT++` is possible, although difficult. `BOUT++` was originally developed for flute reduced plasma models in field aligned geometries. Specifically, the three dimensions used were radial, toroidal, and parallel to the magnetic field. As stated previously, this is inaccurate in the presence of magnetic X- and O-points, which still exist in stellarator geometries. Additionally, the metric tensor within `BOUT++` is two dimensional, as it assumes the third dimension is periodic (toroidal angle) and can be spectrally decomposed. Although a three dimensional metric tensor would be advantageous, we will show here that it is possible to simulate stellarator geometries in `BOUT++` using a non-field-aligned grid through the implementation of the Flux Coordinate Independent (FCI) method for parallel derivatives.

5.2 The Flux Coordinate Independent Method

The advantage of field aligned coordinate systems is that parallel derivatives are simplified to be taken along one dimension of the coordinate system, which is computationally efficient since the majority of turbulence models are described by separating perpendicular and parallel derivatives. One disadvantage of this method is that complex geometries such as magnetic nulls are poorly described and susceptible to numerical instabilities. A second disadvantage of field-aligned coordinate systems is the difficulty associated with generating the mesh for non-axisymmetric fields. In most turbulence codes, field aligned grids are generated using a two dimensional poloidal cross section, and an assumption of axisymmetry which leads to a two dimensional equilibrium. Additionally, the presence of magnetic islands and stochastic magnetic field regions in stellarators render this method impractical. The previous two chapters have utilized a modified parallel derivative scheme in a Cartesian coordinate system (discussed in Section 2.5.2). This method, however, is unsuitable for nonaxisymmetric cases due to the perpendicular displacement of field lines as a function of toroidal angle. That is, as the field line moves toroidally, it also moves significantly in the poloidal plane. The previous method for parallel derivatives relies on the assumption that perpendicular perturbations in the field and stochastic regions are small. Therefore, for cases such as stellarators, another method must be used to calculate parallel derivatives.

Recently Dr Peter Hill has led the implementation of the Flux Coordinate Independent method for calculating parallel derivatives [5, 83] in `BOUT++`. This method for calculating parallel derivatives has been implemented in other codes [132], and is intuitively straightforward, as described in Figure 5.2 [5].

Based on the form of the magnetic field at a given point, the field line is followed to the next poloidal (or azimuthal) plane. The position at which the field line hits the next plane is interpolated to the nearest grid points, and a value for a given quantity is assigned based on that interpolation. This process is repeated on the previous plane, and a differential is calculated based on these interpolated values via central differencing. As the FCI method is used solely for

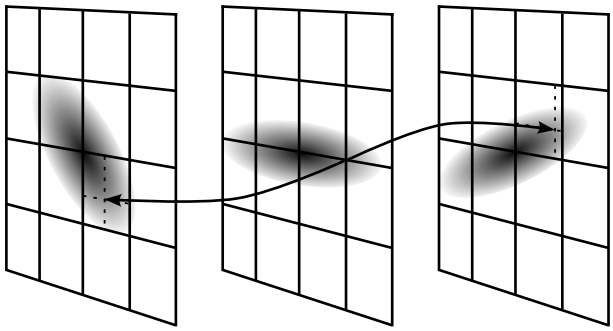

Figure 5.2: Illustration of Flux Coordinate Independent method for calculating parallel derivatives.

calculation of parallel derivatives, the process is independent of the poloidal grid configuration. In the work presented here, the poloidal grids are chosen to be Cartesian. For the FCI method used in `BOUT++`, the interpolation scheme is cubic Hermite spline, but other schemes can be implemented.

While this process is intuitively straightforward, it allows for more complex magnetic field configurations in comparison to structured grids. Previous work has used this model to simulate turbulence in the region of magnetic islands [133], verifying its suitability for magnetic X- and O-points. In the following section, the recent implementation of the FCI method is tested to determine if nonaxisymmetric modelling is possible within `BOUT++`.

5.3 Foundations for stellarator modelling in `BOUT++`

The FCI method has been implemented into `BOUT++` and tested via the method of manufactured solutions [5], which determined that the operators converge to second order, as is expected for the central difference schemes in use. One of the aims of the research presented here is to provide the components necessary to simulate stellarator turbulence cases and evaluate the computational and developmental work required. The following subsection details the progress towards stellarator turbulence using the FCI method by describing the recent nonaxisymmetric test scenarios which have been implemented.

5.3.1 Diffusion test cases

To determine the efficacy of the FCI method as a tool for stellarator turbulence modelling, a test case of an infinite aspect ratio classical stellarator was constructed. A theoretical linear device with 4 helical coils was considered, as shown in Figure 5.3. A Poincaré plot of this configuration was created to ensure the existence of closed flux surfaces, as shown in Figure 5.4.

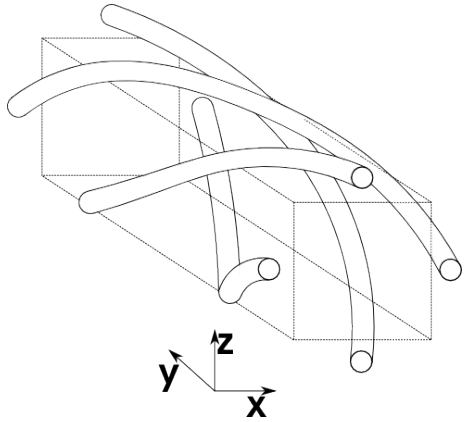

Figure 5.3: The straight stellarator test case; a very large aspect ratio classical stellarator showing helical coils and the inlaid Cartesian coordinate system (dashed).

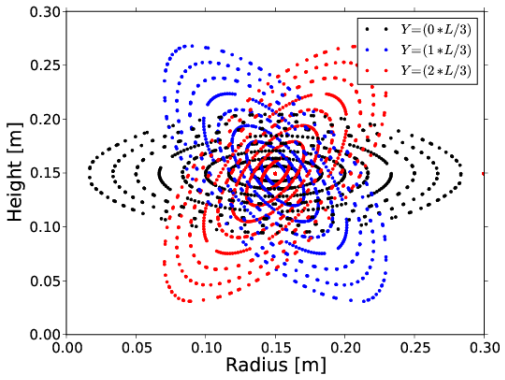

Figure 5.4: Poincaré plot of the straight stellarator indicating closed flux surfaces

This configuration has been implemented into the FCI grid generator [5], which has recently been written in collaboration with Dr. Peter Hill and Dr. Ben Dudson. It is possible to change several parameters in this grid generator including rotational transform, toroidal field and helical coil current/position. A typical grid with 16 Cartesian poloidal planes at 256 x 256 resolution can be generated in approximately 45 seconds.

As the FCI method is purely a tool for calculating parallel dynamics, a simple heat advection equation was modelled:

$$\frac{\partial f}{\partial t} = \nabla \cdot (\mathbf{bb} \cdot \nabla f) \equiv \nabla_{\parallel}^2 f \tag{5.1}$$

By solving Equation 5.1 for an initial three dimensional (non-field-aligned)

Gaussian distribution of our test function f, and allowing the simulated to reach a saturated steady state, it is possible to trace out the flux surfaces (shown in Figure 5.4). The results of the diffusion simulation are shown in Figure 5.5.

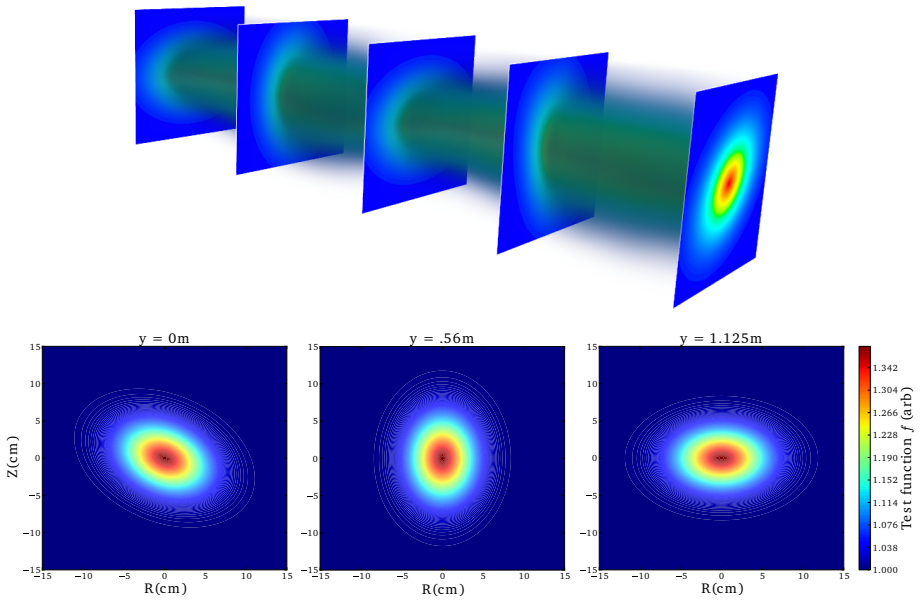

Figure 5.5: Heat diffusion in the straight stellarator test case; flux surfaces are correctly mapped out, qualitatively indicating proper calculation of parallel derivatives.

Figure 5.5 indicates that the FCI method for calculating parallel derivatives is correctly evaluating parallel dynamics; as an initial distribution is left to propagate along the field lines, the flux surfaces are traced out. The extent to which the interpolation of field lines in the perpendicular planes modifies the calculated quantities is tested in the following section.

5.3.2 Inherent Numerical Diffusion

There exists a strong anisotropy of heat conductivity in magnetized fusion plasmas. Parallel conductivity can be as much as a factor of 10^{10} higher than perpendicular conductivity. It is therefore important to reduce errors in parallel operators, as even a small perpendicular pollution of parallel dynamics can lead to substantial errors [134]. One of the main sources of error for the FCI method is the interpolation, as every quantity is interpolated based on where the field lines intersect the next and previous perpendicular planes. The issue can be illustrated

by considering a field aligned structure which is very small in the poloidal plane at a given grid point. Assuming the field line does not intersect a grid point in the next (or previous) perpendicular plane, the structure will be distributed between the four nearest grid points. This will then dissipate the function, causing a loss of accuracy and introducing an error. Currently, the FCI method in `BOUT++` utilizes cubic Hermite spline interpolation, but other methods are possible and can be used [132]. As a test of the interpolation, the previous diffusion case of a straight classical stellarator was implemented for 4 different grid resolutions. It is possible to determine the inherent numerical diffusion from interpolation by assuming that the diffusion follows the relation:

$$\frac{\partial f}{\partial t} = D\nabla_{\perp}^{2} f = D\nabla \cdot (\nabla f - \mathbf{bb} \cdot \nabla f) \tag{5.2}$$

where D is the diffusion coefficient for the numerical diffusion of our test function. The inherent numerical diffusion from the interpolation scheme puts a limit on the minimum resolution which can be used, as low resolution grids will introduce a higher perpendicular numerical diffusion. Ideally, numerical perpendicular diffusion should be at least a factor of 10^{-8} smaller than the parallel dynamics [134]. The scaling of inherent perpendicular numerical diffusion coefficients with perpendicular mesh spacing in the straight stellarator geometry is shown in Figure 5.6, where the diffusion coefficients at a grid point just off-axis (r,z = 16,15cm) are normalized to the parallel diffusion. For this analysis, the number of parallel grid points was fixed at 16, and the number of perpendicular grid points varied; 64x64 resolution gives a mesh spacing of 4.76mm, 128x128 resolution gives a perpendicular mesh spacing of 2.38mm, 256x256 resolution indicates a mesh spacing of 1.19mm, and 512x512 resolution has a mesh spacing of 0.59mm. For reference, the domain size is always set to 30cm x 3m x 30cm, and the parallel resolution is chosen to be a constant 19.6cm. Figure 5.7 indicates the loss of our test function f due to numerical diffusion as a function of time for these various resolutions. The initial transient region in Figure 5.7 is due to the parallel transport along field lines. As the test function fills in the flux surfaces,

the test function f increases in regions which were not initially highly populated. The following decrease is then due to inherent diffusion, as there are no sinks in the system.

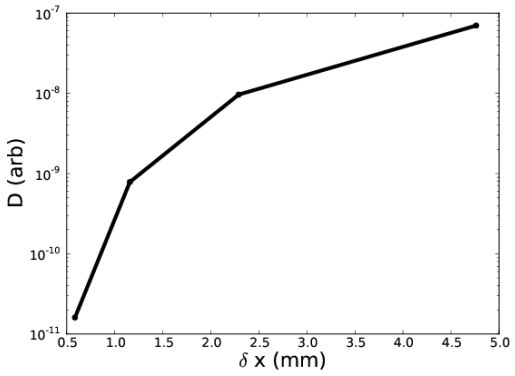

Figure 5.6: Inherent numerical perpendicular diffusion as a function of poloidal mesh spacing in the straight stellarator test case. The fit shows third order convergence, which is broadly in line with previous work [5].

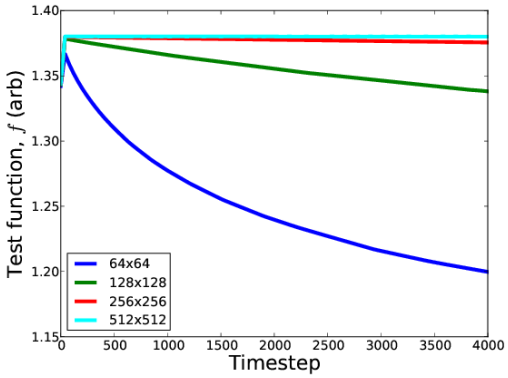

Figure 5.7: The test function f at the center of the domain as a function of time for various resolutions; inherent numerical diffusion serves as an artificial sink at lower resolutions.

From Figures 5.6 and 5.7 it appears that the optimal resolution for an FCI mesh is 256 by 256, as the perpendicular diffusion is at least 10^{-8} smaller than the parallel diffusion. This ensures that the pollution of parallel dynamics in the perpendicular planes is acceptable, following the analysis of [134]. Of course, higher resolution cases are more precise but are also more computationally expensive.

Having quantified the diffusion inherent in the FCI method for parallel derivatives within `BOUT++`, we arrive at a minimum resolution required for this nonaxisymmetric configuration, which is comparable to the resolution one would choose for a given turbulence case for a system of this size, as $\rho_s \approx 1$mm. We have therefore provided evidence that nonaxisymmetric modelling is possible in `BOUT++`, as the most difficult barrier to stellarator modelling is the ability to correctly capture parallel dynamics. The next section describes recent work in implementing a transport model which is a subset of the EMC3 model, which intends to test the efficacy of `BOUT++` as an alternative to common methods used in stellarator modelling.

5.4 Transport modelling

EMC3 [131] is a commonly used tool to simulate the steady state profiles of stellarator edge plasmas, which allows for the reconstruction of heat flux profiles for divertor optimization. Recent work [135] has looked to test the EMC3 model against analytic solutions of the one dimensional transport model. Here, we present the first results following this work in `BOUT++` to determine if `BOUT++` can effectively and efficiently solve a simplified form of the EMC3 equations. The EMC3 equations can be reduced to a one dimensional model which captures isothermal parallel dynamics, which are shown in [135] to be:

$$\frac{\partial n}{\partial t} = -\nabla \cdot \left(n v_\parallel\right) + S_i \tag{5.3}$$

$$\frac{\partial n v_\parallel}{\partial t} = -v_\parallel \nabla_\parallel n v_\parallel - 2T_{e0} \nabla_\parallel n \tag{5.4}$$

where T_{e0} is the isothermal electron temperature, assumed here to be 5eV, n is the density, S_i is the constant source function, and $v_\parallel$ is the parallel velocity. It is possible to solve these expressions to obtain an analytical solution, assuming that the velocity is $\pm c_s$ at the edges of the domain, which are considered to be at $x = \pm L/2$. Using this information, the differential equation can be solved to obtain the analytical solutions which have been previously found to be [135, 136]:

$$n_i(x) = \frac{S_i x}{v_\parallel(x) c_s} \tag{5.5}$$

$$v_\parallel(x) = \frac{L}{2x} - \sqrt{\frac{L^2}{4x^2} - 1} \tag{5.6}$$

where S_i is again the ion source which is independent of position, x is the

distance along the field line, c_s is the sound speed and L is the length of the domain, which spans from $-L/2$ to $L/2$. For all of the following simulations, the boundary conditions were implemented in accordance with [135]. Specifically, velocities were set to $\pm c_s$ (which is normalized to 1) at the upper and lower boundary, respectively. Densities were set to $\frac{S_i L}{2c_s}$.

The first implementation of this model into BOUT++ was done without the use of the FCI method, allowing for testing using conventional operators. Figures 5.8 and 5.9 illustrate a comparison of the analytical model and a simulation using finite volume (flux conserving) operators.

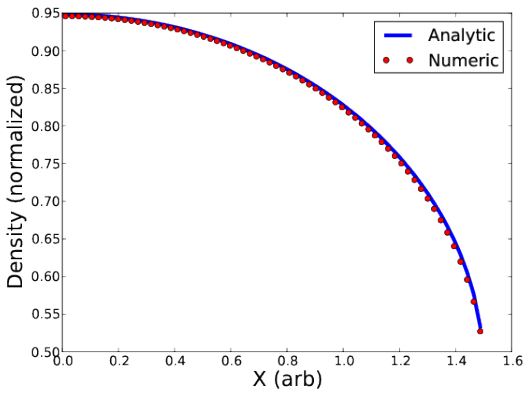

Figure 5.8: Steady state density in a 1D transport model and the analytical solution using conventional finite volume operators in BOUT++.

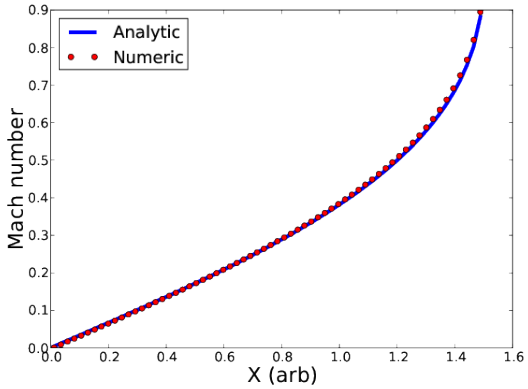

Figure 5.9: Comparison of the steady state velocity in a 1D transport model and an analytical solution using conventional finite volume operators in BOUT++.

It is clear from Figures 5.8 and 5.9 that BOUT++ is capable of simulating the correct profiles in these one dimensional transport equations. However, the FCI method utilizes a finite difference scheme, which is not conservative and therefore could introduce losses. As a test, the conventional (non-FCI) central differencing schemes were implemented and again compared to analytical solution, Figures 5.10 and 5.11

Figures 5.10 and 5.11 indicate that the more simple central differencing scheme fails to reproduce the analytical solution, as the numerical steady state converges to incorrect profiles. Using this method, it is possible that quantities can be lost from the simulation, as these operators are non-conservative; flux

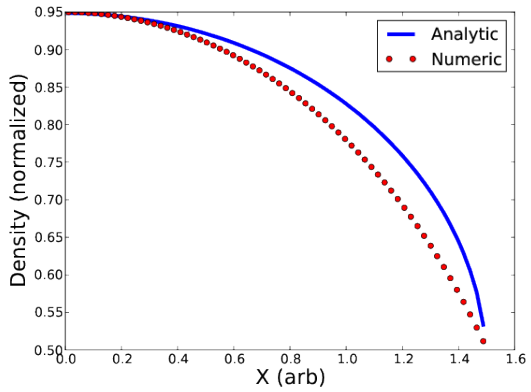

Figure 5.10: Steady state density in a 1D transport model and the analytical solution, having utilized a finite difference scheme within `BOUT++`.

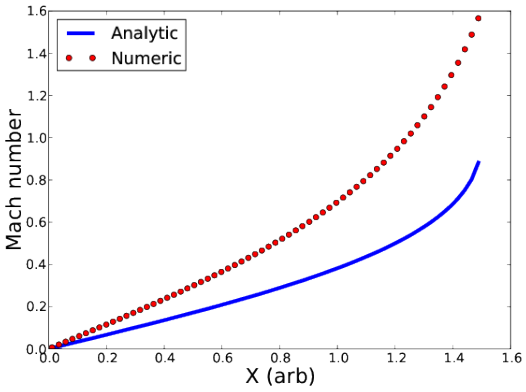

Figure 5.11: Comparison of the steady state velocity using conventional finite difference schemes in a transport model and an analytical solution.

exiting one computational cell is not necessarily entering the next. As such, it is important to reduce these losses when using a finite difference scheme, such as the FCI method. A method for improving these finite difference schemes will be discussed shortly.

To further test the Flux Coordinate Independent method for parallel derivatives, this one dimensional transport model was implemented in the geometry shown in Figure 5.12. This geometry has a completely straight field at the center of the domain, where the FCI method must not interpolate, and an increasingly strong helical field at larger minor radii where interpolation is essential. Furthermore, the magnetic field line length is nonuniform which (referring to Equation 5.5) creates a radially varying profile for density.

The one dimensional transport model was implemented into the geometry shown in Figure 5.12 at various resolutions. Similar to the straight stellarator test case, the parallel resolution ($\mathbf{y}$) was held constant while the resolution of Cartesian poloidal planes was varied. To reduce losses, the FCI operators were modified to calculate derivatives based on the flux at the at the grid cell faces; the flux at the edges of each computational cell was averaged with the flux at the edge of its neighboring cells. While this still does not guarantee the conservation properties of finite volume methods, the quantities are more closely conserved

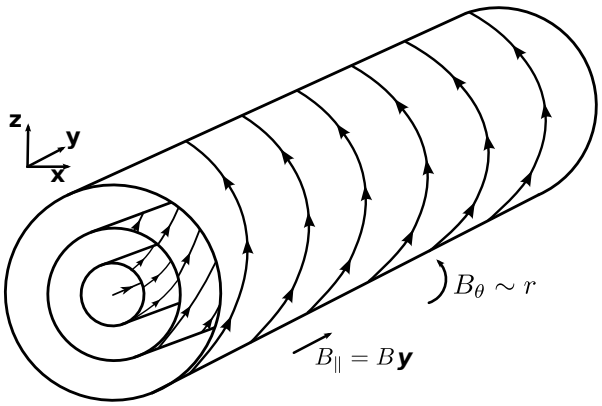

Figure 5.12: The geometry used to test the FCI method when solving the one dimensional transport model. The azimuthal magnetic field is proportional to the minor radius r, allowing a test of straight field lines on axis, and a test of interpolation away from the center.

than in simple finite difference schemes. Figures 5.13 and 5.14 illustrate the results of the transport simulation at the center of the domain shown in Figure 5.12 for three different poloidal resolutions. As these plots are taken at the center of the domain where the field line is straight, they can be compared to the previous finite difference results, Figures 5.10 and 5.11, and a clear improvement is seen.

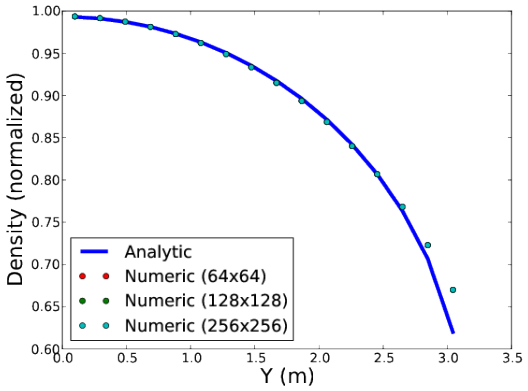

Figure 5.13: Steady state solution for density in the one dimensional transport model and the analytical solution using the FCI method on straight field lines

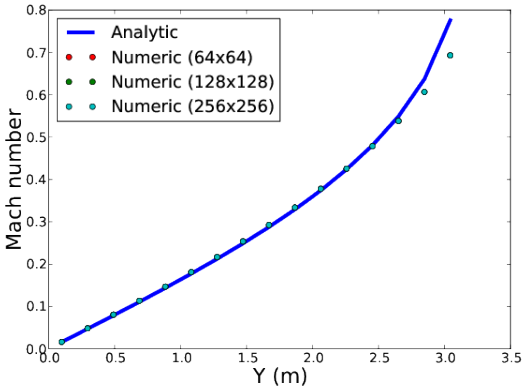

Figure 5.14: Comparison of the steady state velocity and an analytical solution using the FCI method in a region of straight field lines.

As the simulations correctly reproduces the behavior of the analytic model at the center of the domain, it can be concluded that the losses due to the central

differencing scheme used by FCI have been reduced. Furthermore, there is no dependence on poloidal resolution as the interpolation scheme is not used on straight field lines. To test the interpolation of the FCI method, it is useful to examine the results away from the center where the field lines are helical, as shown in Figures 5.15 and 5.16. Specifically, these results were taken at about two-thirds of the distance to the edge of the computational domain, where the shear causes a shift of 2.35cm in the azimuthal direction between each perpendicular plane (separated by 19.6cm).

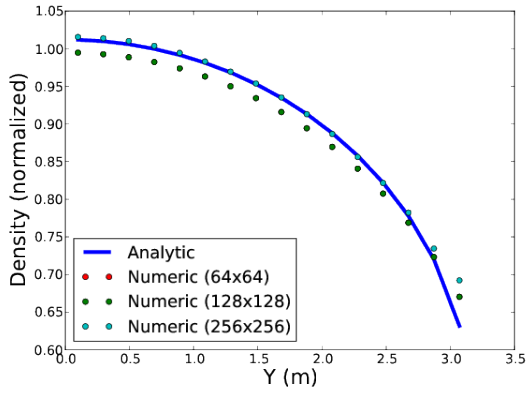

Figure 5.15: Steady state density and the analytical solution of a one dimensional transport model in a region of helical field lines for three different resolutions. Accuracy is increased with resolution.

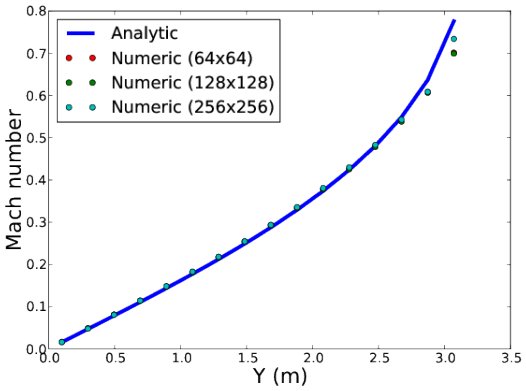

Figure 5.16: Comparison of the steady state velocity and an analytical solution in a region of helical field lines. Again, the higher resolution cases provide more accurate results.

Again, the simulations of the one dimensional transport model have reproduced the analytical solution along helical field lines, when considering a sufficiently high resolution (recalling Section 5.3.2). As these helical field lines require the use of interpolation in the FCI operators, these results indicate that errors due to interpolation are reduced to tolerable levels at sufficient resolution and the FCI method is capable of simulating transport models.

5.5 Recent additions to BOUT++ of interest

Due to the nature of BOUT++ as an open source framework, there are often new methods introduced which can benefit others. There have been several recent implementations in BOUT++ by other developers which are relevant to this research. Firstly, the FCI grid generator has been extended to accept input from files output from VMEC [137], an equilibrium solver commonly used in stellarator physics. This allows for experimental profiles to be implemented, and the intention is to provide future comparison with other codes. Poloidal limiters and parallel boundary conditions for the FCI operators have also been implemented, allowing for more stable and realistic simulations. Numerically, the recent implementation of OpenMP [138] in BOUT++ will allow for better parallelization which should drastically improve performance. Together, the implementations of these methods provide a strong foundation upon which future stellarator modelling in BOUT++ can be performed, as they address the main challenges to nonaxisymmetric modelling.

5.6 Conclusions and Future Work

Here we have discussed the recent progress in modelling nonaxisymmetric geometries within BOUT++. The Flux Coordinate Independent approach to parallel derivatives has been implemented into BOUT++ and allows for complex geometries to be modelled. A very large aspect ratio classical stellarator test case was implemented and it was determined that the FCI approach is correctly evaluating parallel dynamics, which was the most difficult challenge in modelling nonaxisymmetric configurations. A one dimensional transport model was implemented and tested against an analytic solution, where it was determined that BOUT++ can effectively converge to the analytical solution using FCI operators. These results indicate that BOUT++ has the components necessary to model nonaxisymmetric cases.

Future work should look to first model transport in nonaxisymmetric devices, as this is an important step in determining the efficacy of numerical meth-

ods. Furthermore, this would provide a result which can be compared to EMC3, a code which currently has no equivalent for stellarator scenarios. Once this is completed, a full turbulence model should be implemented in an attempt to model global edge fluid turbulence in nonaxisymmetric configurations.

Numerically, `BOUT++` should be modified to have a three dimensional metric tensor. This would allow for more complicated computational meshes and more complete numerical methods. Currently, the implementation of some operators (such as curvature) for stellarator geometries must be implemented by prescribing a three dimensional polarization vector ($\mathbf{b} \times \kappa$) which then modifies the respective terms. This method is exactly what was used in the previous two chapters for curvature, and is often used in tokamak turbulence modelling. The implementation of a three dimensional mesh would allow for three dimensional metric tensors to more accurately capture the effects of local curvature.

The efficiency of the FCI method could potentially be improved by performing the interpolation on a graphical processing unit (GPU), as the repetitive two dimensional operation lends itself well to GPU architecture. While there are several remaining challenges, this work has shown promising progress towards the first global stellarator edge fluid turbulence simulations.

Chapter 6

Conclusions and Future Work

6.1 Conclusions

Turbulent transport in magnetically confined fusion plasmas is the predominant limitation to viable fusion energy. By building larger fusion devices, it is possible to attain fusion-relevant parameters despite the transport due to turbulence. However, the recent increased performance of tokamaks causes an increase of heat and particle flux onto plasma facing components. Understanding the nature of turbulence in regions of plasma exhaust is necessary in the development of efficient, compact fusion reactors. By simulating turbulence in realistic geometries, it is possible to ascertain the performance and limitations of various scenarios. Unfortunately, the efficient simulation of turbulence in realistic magnetic geometries including magnetic X- and O-points presents further challenges. Field-aligned coordinate systems, which are most often employed in tokamak X-point turbulence simulations, have a singularity in the magnetic null region, prohibiting explicit computation. In this thesis, we have presented the results of turbulence simulations using non-field-aligned grids in three different geometries relevant to magnetically confined fusion research.

Chapter 3 details the results of simulations performed as part of a feasibility study for a university-scale linear plasma device capable of producing azimuthal X-points in tokamak divertor-relevant scenarios [1]. This device would allow for direct comparison of plasma turbulence models and accessible experimental investigation of fundamental plasma physics relevant to tokamak divertor

and detachment scenarios. The linear geometry also provides a simple test for the implementation of complex magnetic geometries using a Cartesian grid and a modified parallel gradient operator in `BOUT++` while still providing novel and relevant results. The results presented herein indicate that a modest azimuthal magnetic coil set would produce measurable changes in the plasma profile of a linear device. A characterization of the turbulence within the device has been provided, including a measurements from synthetic diagnostics which could be reproduced experimentally. Among other results, it was shown that the energy dynamics [109] within the system are altered by the introduction of an azimuthal magnetic null point, which causes the energy within the system to be dissipated at higher azimuthal mode numbers. This effect is likely due to the inhibited transport of azimuthally flowing perturbations, which dissolves coherent structures.

Having effectively implemented a Cartesian coordinate system and a modified parallel gradient operator in linear geometries, the method was extended to characterize turbulence in toroidal configurations by considering filament propagation within TORPEX poloidal magnetic null point scenarios [111, 2]. Recent work [111] measured the propagation of blobs in the region of a poloidal magnetic null point. A measured acceleration was attributed to the increasing connection length in the vicinity of the X-point, and a model was previously developed for the observed acceleration [111]. Here, we have further investigated filament propagation in scenarios with both a moving and stationary background. When simulations are performed with a stationary background plasma, the experimental acceleration is not recovered. The analytical model, however, supports the velocity profile of the simulated filaments. This provides first indication that the acceleration seen in experiment might not be entirely dominated by the increasing connection length, as the analytical model is derived in support of this assertion. We are able to recover experimental velocity profiles by introducing a moving background plasma profile as is seen in experiment. This acceleration profile, however, is seen in scenarios both with and without an X-point, indicating that the experimentally measured acceleration is not primarily caused by an

increasing connection length. It is suggested here that the acceleration seen in experiment is caused by an advection of a developing dipole by the background plasma. This advection of the dipole mimics acceleration caused by increasing connection length near an X-point as the filament is accelerated in the direction of the magnetic null.

Finally, the prospects of BOUT++ as a stellarator simulation code were discussed in Chapter 5. The implementation of the Flux Coordinate Independent (FCI) method for parallel derivatives [133] into BOUT++ has allowed for the simulation of complex geometries. Here we have explored two test cases to determine the efficacy of future stellarator transport and turbulence modelling. Firstly, a diffusion equation was modelled in a straight stellarator geometry to verify the implementation of the FCI method. It was shown that the flux surfaces of the straight stellarator were correctly recovered, indicating that the FCI operators had been correctly implemented. In addition, a one dimensional transport model was also implemented into a geometry resembling a circular cross section, infinite aspect ratio tokamak which allows for testing of the central differencing scheme, the implementation of boundary conditions, and the interpolation inherent in the FCI method. We have shown that the transport model within BOUT++ reproduces the analytic solution in regions both with and without interpolation. Together with the previous test case of diffusion in a straight stellarator, this result indicates that the implementation of the FCI method for parallel derivatives into BOUT++ provides the basis for future stellarator turbulence modelling.

6.2 Future Work

The strength of BOUT++ lies in its flexibility. As such, the research presented herein could be repeated with more complex models. For both the linear and toroidal cases presented in Chapters 3 and 4 respectively, a nonisothermal model would elucidate interesting physics. This would especially be useful as the motivation for this work is its relevance to tokamak divertor scenarios where the goal is to minimize heat and particle flux onto plasma facing components. Furthermore, the

simulations in linear geometry could implement a more realistic source and exploit more synthetic diagnostics. Experimentally, the construction of such a device would allow for direct measurements of turbulence in divertor and detachment relevant scenarios.

Simulations in TORPEX poloidal magnetic null point geometries should look to implement a more realistic source region. The filaments presented here were seeded poloidal Gaussians, and the generation of filaments is still a subject for further study. We have presented here an alternative mechanism for filament acceleration in TORPEX X-point scenarios. As such, future experimental campaigns should explore this possibility. Primarily, a test case in vertical field (no X-point) scenarios should be performed. This assertion could also be tested by generating the filaments in a region farther from the X-point, or minimizing the background plasma flow, allowing the dipole to fully develop.

It is important to note that the simulations presented in Chapters 3 and 4 utilize the electrostatic approximation. That is, magnetic fluctuations due to the induced currents within the plasma are neglected. However, in the area of a magnetic null such as an X-point, small magnetic fluctuations can become significant relative to the total strength of the magnetic field. It would be a useful exercise to perform these simulations without making an electrostatic approximation.

Finally, Chapter 5 has discussed the potential for `BOUT++` to simulate non-axisymmetric geometries with a view of stellarator turbulence modelling. The first studies should look to implement a more complex transport model in a geometry which can be compared to EMC3. This would allow for verification of EMC3 while still providing novel physics. Upon successful implementation of a transport model, a full turbulence model should be implemented. This would be the first global edge fluid turbulence code for stellarators, and therefore provide novel results relevant to modern experiments, such as heat flux profiles on the island divertor in Wendelstein 7-X.

Computationally, the ability for `BOUT++` to model stellarator physics could be improved with several advancements. Firstly, the metric tensor should be extended to three dimensions to properly incorporate stellarator physics. Fur-

thermore, the implementation of OpenMP and interfacing with GPU processing would greatly increase efficiency, which is a strong advantage for fluid turbulence modelling. Finally, a more flexible, nonorthogonal computational mesh would allow for more realistic strikepoint coverage and increase efficiency, as the current method grids an entire plasma cross section including the core. Ideally, the mesh would be generated for only the plasma edge and scrape off layer.

The results presented in this thesis provide a basis for plasma turbulence simulation in complex magnetic geometries using `BOUT++`. Additionally, we have provided evidence that `BOUT++` could effectively be used as a stellarator transport and turbulence code.

Bibliography

[1] B W Shanahan and B D Dudson. X-point modelling in linear configurations using bout++. *Journal of Physics: Conference Series*, 561(1):012015, 2014.

[2] B W Shanahan and B D Dudson. Blob dynamics in torpex poloidal null configurations. *Plasma Physics and Controlled Fusion*, 58(12):125003, 2016.

[3] Brendan Shanahan, Peter Hill, and Ben Dudson. Towards nonaxisymmetry; initial results using the flux coordinate independent method in bout++. *arXiv preprint arXiv:1609.06603*, 2016.

[4] Jarrod Leddy, Ben Dudson, Michele Romanelli, Brendan Shanahan, and Nick Walkden. A novel flexible field-aligned coordinate system for tokamak edge plasma simulation. *arXiv preprint arXiv:1604.05876*, 2016.

[5] P Hill, B W Shanahan, and B D Dudson. The fci method in bout++. *In Preparation*, 2016.

[6] I Dincer. Renewable energy and sustainable development: a crucial review. *Renewable and Sustainable Energy Reviews*, 4(2):157–175, 2000.

[7] K Caldeira, A K Jain, and Martin I Hoffert. Climate sensitivity uncertainty and the need for energy without co2 emission. *Science*, 299(5615):2052–2054, 2003.

[8] T B Johansson and L Burnham. *Renewable energy: sources for fuels and electricity*. Island press, 1993.

[9] Naomi Oreskes. The scientific consensus on climate change. *Science*, 306(5702):1686–1686, 2004.

[10] John Cook, Dana Nuccitelli, Sarah A Green, Mark Richardson, Bärbel Winkler, Rob Painting, Robert Way, Peter Jacobs, and Andrew Skuce. Quantifying the consensus on anthropogenic global warming in the scientific literature. *Environmental research letters*, 8(2):024024, 2013.

[11] Camille Parmesan and Gary Yohe. A globally coherent fingerprint of climate change impacts across natural systems. *Nature*, 421(6918):37–42, 2003.

[12] Susan Solomon. *Climate change 2007-the physical science basis: Working group I contribution to the fourth assessment report of the IPCC*, volume 4. Cambridge University Press, 2007.

[13] John A Church and Neil J White. A 20th century acceleration in global sea-level rise. *Geophysical research letters*, 33(1), 2006.

[14] International Energy Agency. Key world energy statistics, 2013.

[15] M King Hubbert et al. Nuclear energy and the fossil fuel. In *Drilling and production practice*. American Petroleum Institute, 1956.

[16] Wikimedia Commons; Plazak. Hubbert upper-bound peak 1956.

[17] and others. Recovery of shale oil, February 8 1966. US Patent 3,233,668.

[18] Kelvin B Gregory, Radisav D Vidic, and David A Dzombak. Water management challenges associated with the production of shale gas by hydraulic fracturing. *Elements*, 7(3):181–186, 2011.

[19] J Ongena and G Van Oost. Energy for future centuries - prospects for fusion power as a future energy source. *FUSION SCIENCE AND TECHNOLOGY*, 53(2T):3–15, 2008.

[20] J H Nuckolls and L Wood. Future of inertial fusion energy. *LLNL Preprint UCRL-JC-149860, Sept*, 33, 2002.

[21] A. Einstein. Ist die trägheit eines körpers von seinem energieinhalt abhängig? *Annalen der Physik*, 323(13):639–641, 1905.

[22] J Wesson. *Tokamaks*. Oxford University Press, Oxford, fourth edition, 2011.

[23] John D Lawson. Some criteria for a power producing thermonuclear reactor. *Proceedings of the Physical Society. Section B*, 70(1):6, 1957.

[24] John D Lindl. *Inertial confinement fusion: the quest for ignition and energy gain using indirect drive*. American Institute Of Physics, 1998.

[25] S Nakai and H Takabe. Principles of inertial confinement fusion-physics of implosion and the concept of inertial fusion energy. *Reports on progress in physics*, 59(9):1071, 1996.

[26] H-S Park, OA Hurricane, DA Callahan, DT Casey, EL Dewald, TR Dittrich, T Döppner, DE Hinkel, LF Berzak Hopkins, S Le Pape, et al. High-adiabat high-foot inertial confinement fusion implosion experiments on the national ignition facility. *Physical review letters*, 112(5):055001, 2014.

[27] John D Lindl, Peter Amendt, Richard L Berger, S Gail Glendinning, Siegfried H Glenzer, Steven W Haan, Robert L Kauffman, Otto L Landen, and Laurence J Suter. The physics basis for ignition using indirect-drive targets on the national ignition facility. *Physics of Plasmas (1994-present)*, 11(2):339–491, 2004.

[28] John Lindl, Otto Landen, John Edwards, Ed Moses, and NIC Team. Review of the national ignition campaign 2009-2012. *Physics of Plasmas*, 21(2), 2014.

[29] TK Fowler and BG Logan. The tandem mirror reactor. 1977.

[30] J Freidberg. *Plasma Physics and Fusion Energy*. Cambridge University Press, 2007.

[31] BB Kadomtsev and MA Leontovich. Fizika plazmy i problema upravlyaemykh termoyadernykh reaktsij. *Plasma physics and the problem of controlled thermonuclear reactions*, 3, 1958.

[32] EuroFusion. Diagram illustrating the tokamak principle: arrangement of magnetic field coils and the resulting magnetic field that confines the plasma, 2011.

[33] M Keilhacker, A Gibson, C Gormezano, PJ Lomas, PR Thomas, ML Watkins, P Andrew, B Balet, D Borba, CD Challis, et al. High fusion performance from deuterium-tritium plasmas in jet. *Nuclear Fusion*, 39(2):209, 1999.

[34] JET Team. Fusion energy production from a deuterium-tritium plasma in the jet tokamak. *Nuclear Fusion*, 32(2):187, 1992.

[35] R Aymar, P Barabaschi, and Y Shimomura. The iter design. *Plasma physics and controlled fusion*, 44(5):519, 2002.

[36] Lyman Spitzer Jr. The stellarator concept. *Physics of Fluids (1958-1988)*, 1(4):253–264, 1958.

[37] M Hirsch, J Baldzuhn, C Beidler, R Brakel, R Burhenn, A Dinklage, H Ehmler, M Endler, V Erckmann, Y Feng, et al. Major results from the stellarator wendelstein 7-as. *Plasma Physics and Controlled Fusion*, 50(5):053001, 2008.

[38] DT Anderson, JA Derr, and JL Shohet. The interchangeable module stellarator. *Plasma Science, IEEE Transactions on*, 9(4):212–220, 1981.

[39] G Grieger, W Lotz, P Merkel, J Nührenberg, J Sapper, E Strumberger, H Wobig, R Burhenn, V Erckmann, U Gasparino, et al. Physics optimization of stellarators. *Physics of Fluids B: Plasma Physics (1989-1993)*, 4(7):2081–2091, 1992.

[40] Allen H Boozer. What is a stellarator? *Physics of Plasmas (1994-present)*, 5(5):1647–1655, 1998.

[41] Guenter Grieger and I Milch. Das fusionsexperiment wendelstein 7-x. *Physikalische Blätter*, 49(11):1001–1005, 1993.

[42] MG Haines. Fifty years of controlled fusion research. 1996.

[43] S P Hirshman and D J Sigmar. Neoclassical transport of impurities in tokamak plasmas. *Nuclear Fusion*, 21(9):1079, 1981.

[44] C S Pitcher and PC Stangeby. Experimental divertor physics. *Plasma physics and controlled fusion*, 39(6):779, 1997.

[45] EuroFusion, 2011.

[46] F Wagner, G Becker, K Behringer, D Campbell, A Eberhagen, W Engelhardt, G Fussmann, O Gehre, J Gernhardt, G v Gierke, et al. Regime of improved confinement and high beta in neutral-beam-heated divertor discharges of the asdex tokamak. *Physical Review Letters*, 49(19):1408, 1982.

[47] Ker-Chung Shaing and EC Crume Jr. Bifurcation theory of poloidal rotation in tokamaks: A model for l-h transition. *Physical Review Letters*, 63(21):2369, 1989.

[48] PW Terry. Suppression of turbulence and transport by sheared flow. *Reviews of Modern Physics*, 72(1):109, 2000.

[49] G Federici, A Loarte, and G Strohmayer. Assessment of erosion of the iter divertor targets during type i elms. *Plasma physics and controlled fusion*, 45(9):1523, 2003.

[50] A Zhitlukhin, N Klimov, I Landman, J Linke, A Loarte, M Merola, V Podkovyrov, G Federici, B Bazylev, S Pestchanyi, et al. Effects of elms on iter divertor armour materials. *Journal of nuclear materials*, 363:301–307, 2007.

[51] S I Krasheninnikov, A Y Pigarov, and D J Sigmar. Plasma recombination and divertor detachment. *Physics Letters A*, 214(5):285–291, 1996.

[52] P M Valanju, M Kotschenreuther, S M Mahajan, and J Canik. Super-x divertors and high power density fusion devices. *Physics of Plasmas*, 16(5):056110–056110, 2009.

[53] GF Matthews. Plasma detachment from divertor targets and limiters. *Journal of nuclear materials*, 220:104–116, 1995.

[54] H Zohm, C Angioni, E Fable, G Federici, G Gantenbein, T Hartmann, K Lackner, E Poli, L Porte, O Sauter, et al. On the physics guidelines for a tokamak demo. *Nuclear Fusion*, 53(7):073019, 2013.

[55] M Kotschenreuther, P Valanju, B Covele, and S Mahajan. Magnetic geometry and physics of advanced divertors: The x-divertor and the snowflake. *arXiv:1309.5289*, 2013.

[56] D D Ryutov. Geometrical properties of a "snowflake.

[57] VD Shafranov. Plasma equilibrium in a magnetic field. *Reviews of Plasma Physics*, 2:103, 1966.

[58] Jean Paul Richter. The notebooks of leonardo da vinci: Compiled and edited from the original manuscripts, in two vols.; reprinted new york, 1970.

[59] Vadim Nikolaevich TSytovich. Theory of turbulent plasma. 1977.

[60] B D Dudson. *Edge Turbulence in the Mega-Amp Spherical Tokamak*. PhD thesis, University of Oxford, Trinity College, 2007.

[61] P B Snyder. *Gyrofluid Theory and Simulation of Electromagnetic Turbulence and Transport in Tokamak Plasmas*. PhD thesis, Princeton University, Department of Astrophysical Sciences, 1999.

[62] S J Zweben, J A Boedo, O Grulke, C Hidalgo, B LaBombard, R J Maqueda, P Scarin, and J L Terry. Edge turbulence measurements in toroidal fusion devices. *Plasma Phys. Control. Fusion*, 49(7):S1–S23, Jul 2007.

[63] D A D´ Ippolito, J R Myra, and S J Zweben. Convective transport by intermittent blob-filaments: Comparison of theory and experiment. *Physics of Plasmas*, 18:060501, 2011.

[64] N R Walkden. *Properties of Intermittent Transport in the Mega Ampere Spherical Tokamak*. PhD thesis, University of York, 2015.

[65] DA D'Ippolito, JR Myra, SI Krasheninnikov, GQ Yu, and A Yu Pigarov. Blob transport in the tokamak scrape-off-layer. *Contributions to Plasma Physics*, 44(1-3):205–216, 2004.

[66] A Kirk, N Ben Ayed, G Counsell, B Dudson, T Eich, A Herrmann, B Koch, R Martin, A Meakins, S Saarelma, R Scannell, S Tallents, M Walsh, H R Wilson, and the MAST team. Filament structures at the plasma edge on mast. *Plasma Physics and Controlled Fusion*, 48(12B):B433, 2006.

[67] RJ Maqueda, GA Wurden, S Zweben, L Roquemore, H Kugel, D Johnson, S Kaye, S Sabbagh, and R Maingi. Edge turbulence measurements in nstx by gas puff imaging. *Review of Scientific Instruments*, 72(1):931–934, 2001.

[68] JP Graves, J Horacek, RA Pitts, and KI Hopcraft. Self-similar density turbulence in the tcv tokamak scrape-off layer. *Plasma physics and controlled fusion*, 47(3):L1, 2005.

[69] BA Carreras, VE Lynch, and B LaBombard. Structure and properties of the electrostatic fluctuations in the far scrape-off layer region of alcator c-mod. *Physics of Plasmas (1994-present)*, 8(8):3702–3707, 2001.

[70] T Happel, F Greiner, N Mahdizadeh, B Nold, M Ramisch, and U Stroth. Generation of intermittent turbulent events at the transition from closed to open field lines in a toroidal plasma. *Physical review letters*, 102(25):255001, 2009.

[71] GY Antar, SI Krasheninnikov, P Devynck, RP Doerner, EM Hollmann, JA Boedo, SC Luckhardt, and RW Conn. Experimental evidence of intermittent convection in the edge of magnetic confinement devices. *Physical review letters*, 87(6):065001, 2001.

[72] SH Müller, Ahmed Diallo, Ambrogio Fasoli, Ivo Furno, Benoît Labit, and Mario Podestà. Plasma blobs in a basic toroidal experiment: Origin, dynamics, and induced transport. *Physics of Plasmas (1994-present)*, 14(11):110704, 2007.

[73] F Riva and et al. Blob dynamics in the torpex experiment: a multi-code validation. *Plasma Physics and Controlled Fusion*, 58(4):044005, 2016.

[74] Sergei I Krasheninnikov. On scrape off layer plasma transport. *Physics Letters A*, 283(5):368–370, 2001.

[75] AV Nedospasov, VG Petrov, and GN Fidel'man. Plasma convection in the poloidal limiter shadow of a tokamak. *Nuclear fusion*, 25(1):21, 1985.

[76] S. I. Krasheninnikov, D. A. D'Ippolito, and J. R. Myra. Recent theoretical progress in understanding coherent structures in edge and sol turbulence. *Journal of Plasma Physics*, 74:679–717, 10 2008.

[77] OE Garcia, V Naulin, AH Nielsen, and J Juul Rasmussen. Turbulence and intermittent transport at the boundary of magnetized plasmas. *Physics of Plasmas (1994-present)*, 12(6):062309, 2005.

[78] P Ricci, F D Halpern, S Jolliet, J Loizu, A Mosetto, A Fasoli, I Furno, and C Theiler. Simulation of plasma turbulence in scrape-off layer conditions: the gbs code, simulation results and code validation. *Plasma Physics and Controlled Fusion*, 54(12):124047, 2012.

[79] Patrick Tamain, H Bufferand, Guido Ciraolo, Clothilde Colin, Ph Ghendrih, Frédéric Schwander, and Eric Serre. 3d properties of edge turbulent transport in full-torus simulations and their impact on poloidal asymmetries. *Contributions to Plasma Physics*, 54(4-6):555–559, 2014.

[80] R. Courant, K. Friedrichs, and H. Lewy. Über die partiellen differenzengleichungen der mathematischen physik. *Mathematische Annalen*, 100(1):32–74.

[81] DD Ryutov, RH Cohen, WA Farmer, TD Rognlien, and MV Umansky. The churning mode of plasma convection in the tokamak divertor region. *Physica Scripta*, 89(8):088002, 2014.

[82] D D Ryutov, R H Cohen, T D Rognlien, and M V Umansky. A snowflake divertor: a possible solution to the power exhaust problem for tokamaks. *Plasma Physics and Controlled Fusion*, 54(12):124050, 2012.

[83] F Hariri and M Ottaviani. A flux-coordinate independent field-aligned approach to plasma turbulence simulations. *Computer Physics Communications*, 184(11):2419 – 2429, 2013.

[84] N R Walkden, B D Dudson, and G Fishpool. Characterization of 3d filament dynamics in a mast sol flux tube geometry. *Plasma Physics and Controlled Fusion*, 55(10):105005, 2013.

[85] A N Simakov and P J Catto. Drift-ordered fluid equations for field-aligned modes in low-β collisional plasma with equilibrium pressure pedestals. *Physics of Plasmas*, 10(12):pp. 4744–4757, December 2003.

[86] Andrei N. Simakov and Peter J. Catto. Erratum: âdrift-ordered fluid equations for field-aligned modes in low-Î²*collisionalplasmawithequilibriumpressurepedestals*â[*phys.plasmas*10, 4744(2003)].

[87] SI Braginskii. Transport processes in a plasma. *Reviews of plasma physics*, 1:205, 1965.

[88] J. J. Ramos. General expression of the gyroviscous force. *Physics of Plasmas*, 12(11), 2005.

[89] Zuoyang Chang and J. D. Callen. Generalized gyroviscous force and its effect on the momentum balance equation. *Physics of Fluids B*, 4(7), 1992.

[90] Donald D Gray and Aldo Giorgini. The validity of the boussinesq approximation for liquids and gases. *International Journal of Heat and Mass Transfer*, 19(5):545–551, 1976.

[91] K Bodi, G Ciraolo, Ph Ghendrih, F Schwander, E Serre, and P Tamain. Impact of the boussinesq approximation in tokamak scrape-off layer turbulence. 2011.

[92] J D Jackson. *Classical Electrodynamics, Third edition*. John Wiley and Sons, 1999.

[93] A Arakawa and V R Lamb. Computational design of the basic dynamical processes of the {UCLA} general circulation model. In J Chang, editor, *General Circulation Models of the Atmosphere*, volume 17 of *Methods in Computational Physics: Advances in Research and Applications*, pages 173 – 265. Elsevier, 1977.

[94] A C Hindmarsh et al. SUNDIALS: Suite of nonlinear and differential/algebraic equation solvers. *ACM Transactions on Mathematical Software*, 31(3):363–396, 2005.

[95] B LaBombard, E Marmar, J Irby, R Vieria, S Wolfe, P Bonoli, C Fiore, R Granetz, M Greenwald, I Hutchinson, et al. X-point target divertor concept and the alcator dx high power divertor test facility. In *APS Meeting Abstracts*, volume 1, page 4002, 2013.

[96] YK M Peng, PJ Fogarty, Thomas W Burgess, Dennis J Strickler, Brad E Nelson, J Tsai, CA Neumeyer, R Bell, C Kessel, J Menard, et al. A component test facility based on the spherical tokamak. *Plasma physics and controlled fusion*, 47(12B):B263, 2005.

[97] EB Hooper, MD Brown, JA Byers, TA Casper, BI Cohen, RH Cohen, MC Jackson, TB Kaiser, AW Molvik, WM Nevins, et al. Modeling results for a linear simulator of a divertor. Technical report, Lawrence Livermore National Lab., CA (United States), 1993.

[98] B MihaljÄiÄ, P K Browning, and K J Gibson. Spatially resolved spectroscopy of detached recombining plasmas in the university of manchester linear system divertor simulator. *Physics of Plasmas (1994-present)*, 14(1):– , 2007.

[99] J C Sandeman, P Uddholm, J A Elliott, and M G Rusbridge. Experiments on drift wave launching: I. dispersion curves and damping rates. *Plasma Physics and Controlled Fusion*, 39(1):159, 1997.

[100] W Gekelman, H Pfister, Z Lucky, D Bamber, Jand Leneman, and J Maggs. Design, construction, and properties of the large plasma research deviceâthe lapd at ucla. *Review of Scientific Instruments*, 62(12):2875–2883, 1991.

[101] B D Dudson, M V Umansky, X Q Xu, P B Snyder, and H R Wilson. BOUT++: A framework for parallel plasma fluid simulations. *Computer Physics Communications*, 180:1467–1480, 2009.

[102] B D Scott. The nonlinear drift wave instability and its role in tokamak edge turbulence. *New Journal of Physics*, 4(1):52, 2002.

[103] M. V. Umansky, P. Popovich, T. A. Carter, B. Friedman, and W. M. Nevins. Numerical simulation and analysis of plasma turbulence the large plasma devicea). *Physics of Plasmas (1994-present)*, 18(5):–, 2011.

[104] L Isoardi, G Chiavassa, G Ciraolo, P Haldenwang, E Serre, Ph Ghendrih, Y Sarazin, F Schwander, and P Tamain. Penalization modeling of a limiter in the tokamak edge plasma. *Journal of Computational Physics*, 229(6):2220 – 2235, 2010.

[105] M G Rusbridge, G Sewell, H Qaosim, D A Forder, M Kay, A Randewich, A Mirarefin, P K Browning, K J Gibson, and J Hugill. Observations of the interaction of a plasma stream with neutral gas: evidence of plasma loss through molecular-activated recombination. *Plasma Physics and Controlled Fusion*, 42(5):579, 2000.

[106] J Loizu, P Ricci, F D Halpern, and S Jolliet. Boundary conditions for plasma fluid models at the magnetic presheath entrance. *Physics of Plasmas (1994-present)*, 19(12):–, 2012.

[107] B Scott. *Plasma Physics and Controlled Fusion*, 45:A385–398, 2003.

[108] Bruce D Scott and Sadruddin Benkadda. Introduction to turbulence in magnetised plasmas. In *Aip Conference Proceedings*, volume 1013, page 20, 2008.

[109] B Friedman, T A Carter, M V Umansky, D Schaffner, and B Dudson. Energy dynamics in a simulation of lapd turbulence. *Physics of Plasmas (1994-present)*, 19(10):–, 2012.

[110] I. Furno, B. Labit, M. Podestà, A. Fasoli, S. H. Müller, F. M. Poli, P. Ricci, C. Theiler, S. Brunner, A. Diallo, and J. Graves. Experimental observation of the blob-generation mechanism from interchange waves in a plasma. *Phys. Rev. Lett.*, 100:055004, Feb 2008.

[111] F. Avino, A. Fasoli, I. Furno, P. Ricci, and C. Theiler. x-point effect on plasma blob dynamics. *Phys. Rev. Lett.*, 116:105001, Mar 2016.

[112] J. R. Myra, D. A. Russell, and D. A. DâIppolito. Collisionality and magnetic geometry effects on tokamak edge turbulent transport. i. a two-region model with application to blobs. *Physics of Plasmas*, 13(11), 2006.

[113] A Fasoli et al. Electrostatic instabilities, turbulence and fast ion interactions in the torpex device. *Plasma Physics and Controlled Fusion*, 52(12):124020, 2010.

[114] M. Podestà, A. Fasoli, B. Labit, I. Furno, P. Ricci, F. M. Poli, A. Diallo, S. H. Müller, and C. Theiler. Cross-field transport by instabilities and blobs in a magnetized toroidal plasma. *Phys. Rev. Lett.*, 101:045001, Jul 2008.

[115] C. Theiler, I. Furno, P. Ricci, A. Fasoli, B. Labit, S. H. Müller, and G. Plyushchev. Cross-field motion of plasma blobs in an open magnetic field line configuration. *Phys. Rev. Lett.*, 103:065001, Aug 2009.

[116] F Avino, A Fasoli, and I Furno. The new torpex in-vessel toroidal conductor for the generation of a poloidal magnetic field. *Review of Scientific Instruments*, 85(3):–, 2014.

[117] F Avino. *Turbulence at the boundary of toroidal plasmas with open and closed magnetic flux surfaces*. PhD thesis, CRPP, EPFL, 2015.

[118] L. Easy, F. Militello, J. Omotani, B. Dudson, E. HavlÃÄkovÃ¡, P. Tamain, V. Naulin, and A. H. Nielsen. Three dimensional simulations of plasma

filaments in the scrape off layer: A comparison with models of reduced dimensionality. *Physics of Plasmas*, 21(12), 2014.

[119] Federico D. Halpern, Annalisa Cardellini, Paolo Ricci, SÃ©bastien Jolliet, Joaquim Loizu, and Annamaria Mosetto. Three-dimensional simulations of blob dynamics in a simple magnetized torus. *Physics of Plasmas*, 21(2), 2014.

[120] J R Angus, M V Umansky, and S I Krasheninnikov. Effect of drift waves on plasma blob dynamics. *Physical Review Letters*, 108(21):215002, 2012.

[121] Robert S Cohen, Lyman Spitzer Jr, and Paul McR Routly. The electrical conductivity of an ionized gas. *Physical Review*, 80(2):230, 1950.

[122] Alejandro Paredes, Hugo Bufferand, Guido Ciraolo, Frédéric Schwander, Eric Serre, Philippe Ghendrih, and Patrick Tamain. A penalization technique to model plasma facing components in a tokamak with temperature variations. *Journal of Computational Physics*, 274:283–298, 2014.

[123] I Furno and F Avino. Private Communication, 2015.

[124] Lyman Spitzer Jr and Richard Härm. Transport phenomena in a completely ionized gas. *Physical Review*, 89(5):977, 1953.

[125] H. Tawara, Y. Itikawa, H. Nishimura, and M. Yoshino. Cross sections and related data for electron collisions with hydrogen molecules and molecular ions. *Journal of Physical and Chemical Reference Data*, 19(3), 1990.

[126] Darwin D-M Ho and Russell M Kulsrud. Neoclassical transport in stellarators. *Physics of Fluids (1958-1988)*, 30(2):442–461, 1987.

[127] J Nührenberg, W Lotz, P Merkel, C Nührenberg, U Schwenn, E Strumberger, and T Hayashi. Overview on wendelstein 7-x theory. *Fusion Technology*, 27(CONF-941182–), 1995.

[128] Neil McTaggart, Roman Zagórski, Xavier Bonnin, A Runov, Ralf Schneider, T Kaiser, T Rognlien, and M Umansky. 3d edge energy transport in stellarator configurations. *Journal of nuclear materials*, 337:221–226, 2005.

[129] Jeremy D Lore, Tamara Andreeva, Jean Boscary, Sergey Bozhenkov, Joachim Geiger, Jeffrey H Harris, Hauke Hoelbe, Arnold Lumsdaine, Dean McGinnis, Alan Peacock, et al. Design and analysis of divertor scraper elements for the w7-x stellarator. *IEEE Transactions on Plasma Science*, 42(3):539–544, 2014.

[130] T Görler, X Lapillonne, S Brunner, Tilman Dannert, Frank Jenko, Florian Merz, and D Told. The global version of the gyrokinetic turbulence code gene. *Journal of Computational Physics*, 230(18):7053–7071, 2011.

[131] Y Feng, F Sardei, and J Kisslinger. 3d fluid modelling of the edge plasma by means of a monte carlo technique. *Journal of nuclear materials*, 266:812–818, 1999.

[132] Andreas Stegmeir, David Coster, Omar Maj, Klaus Hallatschek, and Karl Lackner. The field line map approach for simulations of magnetically confined plasmas. *Computer Physics Communications*, 198:139–153, 2016.

[133] P Hill, F Hariri, and M Ottaviani. The effect of magnetic islands on ion temperature gradient turbulence driven transport. *Physics of Plasmas (1994-present)*, 22(4):042308, 2015.

[134] S Günter, Q Yu, J Krüger, and K Lackner. Modelling of heat transport in magnetised plasmas using non-aligned coordinates. *Journal of Computational Physics*, 209(1):354–370, 2005.

[135] J Cosfeld, F Hasenbeck, M Rack, and Y Feng. Analytische lösungen des vereinfachten emc3 models. In *DPG-Frühjahrstagung der Sektion Atome, Moleküle, Quantenoptik und Plasmen (SAMOP)*. DPG, 2016.

[136] Oleksandr Kalentev. *A Finite Difference Code for 3D Plasma Edge Modelling*. PhD thesis, Universität Greifswald, 2008.

[137] SP Hirshman and O Betancourt. Preconditioned descent algorithm for rapid calculations of magnetohydrodynamic equilibria. *Journal of Computational Physics*, 96(1):99–109, 1991.

[138] Leonardo Dagum and Rameshm Enon. Openmp: an industry standard api for shared-memory programming. *Computational Science & Engineering, IEEE*, 5(1):46–55, 1998.